NANYANG TECHNOLOGICAL UNIVERSITY
SINGAPORE

# ELUCIDATING THE EFFECTS OF RADIANT AND SUB-RADIANT INTERACTIONS IN TERAHERTZ METAMATERIALS

**MANUKUMARA MANJAPPA**

**SCHOOL OF PHYSICAL AND MATHEMATICAL SCIENCES**

**2018**

# ELUCIDATING THE EFFECTS OF RADIANT AND SUB-RADIANT INTERACTIONS IN TERAHERTZ METAMATERIALS

**MANUKUMARA MANJAPPA**

School of Physical and Mathematical Sciences

A thesis submitted to the Nanyang Technological University
in partial fulfillment of the requirement for the degree of
Doctor of Philosophy

**2018**

*For my beloved parents*

# Acknowledgements

First of all, I would like to express my heartfelt gratitude and my sincere thanks to my research supervisor Prof. Ranjan Singh, for his continuous support and immense motivation throughout my PhD. I wholeheartedly acknowledge his positive influence, precise direction and his strong encouragement towards research that always motivated me to work with a positive intent and energy. I feel privileged to have carried out my PhD thesis under his invaluable guidance and supervision.

I would like to express my sincere thanks to Prof. David Wilkowski for co-supervising my thesis and for his valuable inputs and guidance during my PhD. I also would like to extend my thanks to Prof. Sum Tze Chien and Prof. Arokiaswami Alphones for their constant inputs as thesis advisory committee (TAC) members.

I express my grateful thanks to Prof. Nikolay I Zheludev, Prof. Chengkuo Lee, Prof. Andrew A Bettiol and Prof. Sum Tze Chien for their fruitful collaborations and for their timely and valuable inputs on my works. I also express my heartfelt thanks to my master thesis supervisor Prof. Andal Narayanan from RRI, Bangalore, for her constant support and motivation for my research. I express my sincere thanks to all the professors of my Master degree from the Physics department, University of Mysore for their thoughtful guidance.

I thank all my colleagues including Prakash Pitchappa, Yogesh Kumar Srivatava, Longqing Cong, Abhishek Kumar, Govind Dayal, Manoj Gupta, Wen Xiang Lim, Thomas CaiWei Tan, Song Han and Sreekanth for their grateful help and delightful discussions during my PhD work. I express my heartfelt thanks to Shuvan Prashant Turaga, Ankur Solanki and Harish N S Krishnamoorthy for their immense contribution in the collaborative works and for fruitful interactions.

I greatly acknowledge the selfless help from all the research staff and students from CDPT for lending the lab equipment when needed and for useful discussions. I thank all the office staffs of CDPT and PAP for their kind assistance during my PhD term. I thank all the people who constantly lent their support and help during my PhD research.

I wholeheartedly thank all my friends and my classmates for making this journey a easy and a memorable one. Specially, I express a very special thanks and my heartfelt love to Padmashree, Neelima, Radhakrishna and their family, for their warmhearted love, selfless care and for making me a part of their own family. I cherish their love, smiles, presence and constant support during the ups-downs throughout this journey.

Finally, I feel this section will carry no meaning without expressing my very special

gratitude and my hearty love to my beloved parents, who has been my greatest inspiration throughout my life. My heartfelt love to my uncle, my aunt, my brother Dr. Umesh and my sister-in-law Dr. Rachana. Their constant care, happiness, love and invaluable support make this journey the most cherished and treasured part of my life. Their trust and belief in my decisions and my abilities, has greatly inspired me to move forward in the difficult situations with more enthusiasm. I would like to end this section by dedicating this thesis and the incredible journey of my PhD to my beloved parents who have made many sacrifices for my progress and they have been the most influential part in the successful completion of this PhD thesis.

# Contents

# List of Figures

# List of Tables

# Abstract

This thesis discusses the study and implications of near-field interactions mediated by radiant and sub-radiant resonant modes in passive metamaterials (MMs), MEMS actuated active MMs and semiconductor-metamaterial heterostructures at terahertz frequencies.

The thesis is divided into two parts, where the first part of the thesis includes first three chapters (Chaps. 2, 3 and 4) that discusses on the phenomena of metamaterial induced transparency and lattice induced transparency in the metamaterial structures at terahertz frequencies. Theoretical analysis using classical coupled oscillators model is proposed to unravel the interaction mechanisms that reveals the radiant and sub-radiant type of Fano interference effects in the system. These systems show strong slow light effects with large enhancement in the group delay of the pulse through the medium. Further, the implications of the competing electric and magnetic near-field interactions on the transmission characteristics of the medium have shown to exhibit resonant invisibility effects showing an active control of effective permittivity and permeability of the medium.

Second part of the thesis (Chap. 5 and Chap. 6) focuses on the demonstration of excitation and active modulation of sharp Fano resonances in a MEMS metamaterial and semiconductor-metamaterial hybrid heterostructure systems. Excitation of Fano resonance in MEMS metamaterial by introducing out-of plane structural asymmetry exhibits anisotropic coupling that results in the multiple-input-output (meta-hysteresis) characteristics in its near- and far-field optical properties. This exhibits exciting features such as NAND and XOR logical operations, where XOR function can show direct implications in the one-time pad (OTP) secured cryptographic channel for sub-terahertz wireless communications. Further, an active control of Fano resonance in a heterostructure consisting of solution processed $CH_3NH_3PbI_3/PbI_2$ semiconductors spin coated on a metamaterial structure is discussed that exhibits ultrasensitive and ultrafast modulation of Fano resonance in the metamaterial structure, respectively (Chap. 6). Additionally, a new signature of localized plasmon-phonon quasiparticles sensing and interference effects are observed and elucidated using the coupled oscillator model. This phenomenon reveals a strong resonant interactions between the elementary excitations that can be actively controlled by optically pumping the sample using a femtosecond pulse. The thesis concludes by discussing the importance and the future prospectives of the conducted studies.

# Chapter 1

# Introduction: Theory and Overview

Light-matter interaction has been a focus of study over the centuries. It helps to explore the resonant and the off-resonant properties of the materials over entire part of the electromagnetic (EM) spectrum. Until late twentieth century, light-matter interaction in terahertz part of the EM spectrum was the least explored and was termed as the 'THz gap'. With the advent of metamaterials (MMs), which exhibit structure dependent resonance properties, have become excellent candidates for probing light-matter interactions at terahertz frequencies. Metamaterials are composed of periodic array of sub wavelength sized meta-atoms, which exhibit strong near-field coupling that can carry the interaction energy over to far-field regimes. This chapter gives an overview and the theoretical foundations for the works carried out the thesis that mainly focuses on the characterization of near- and far-field optical properties of MMs in terms of their radiant-subradiant interactions in realizing new and versatile MM based optical devices at terahertz frequencies.

This chapter introduces the basic concepts and technical details of the terahertz spectroscopy and metamaterial research. The necessary tools in understanding and

elucidating the terahertz manipulation using MMs that includes the numerical simulators, fabrication processes and the terahertz characterization are being discussed. Last part of this chapter focuses on providing and discussing the scope and outline of the present thesis.

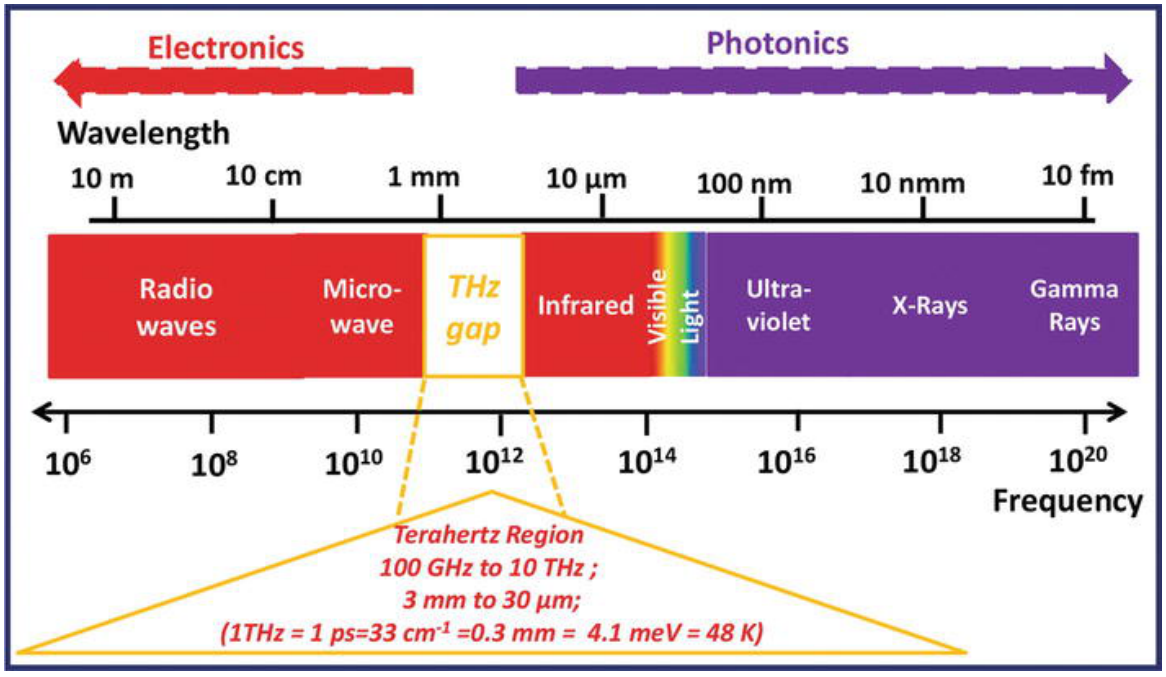


Figure 1.1: Electromagnetic (EM) spectral band highlighting the THz spectral region of interest. (*Source: Internet*)

## 1.1 Terahertz (THz) Spectroscopy

Terahertz (THz) waves (T-waves) [1] are characterized as non-ionizing radiation possessing sub-millimeter photons of wavelengths ranging from 30 $\mu$m to 3 mm (0.1 - 10 THz). These waves are bounded between the microwaves and the infrared frequencies in the electromagnetic (EM) spectrum, thereby bridging the gap between the high-speed electronics and the photonics (see, Fig.1.1). THz waves show numerous applications[2, 3] in our day to day life that include security screening [4], wireless high bandwidth communications[5, 6], THz imaging of tissues in medical sectors,

quality control processes and in scientific sectors. THz waves show great prospects in the field of optics, condensed matter physics and wireless communications. However, they have been underutilized due to the existence of what is known as 'THz gap'. The THz-gap was majorly existed until the end of 20th century that saw the least amount of progress in THz technologies in comparison to other part of the electromagnetic spectrum due to the lack of natural material sources, detectors and the optical components that respond to THz region of EM spectrum. The progress in the THz spectroscopy was stimulated by the pioneering works on photoconductive switch [7–10] and nonlinear frequency mixing [11–14] based generation of THz radiation using the radiation damaged epitaxial silicon on sapphire (SoS) substrate and the lithium tantalate ($LiTaO_3$) crystal, respectively. These works set the tone for the development of the terahertz time domain (THz-TDS) spectroscopy, which till today serves as the first choice spectroscopic tool broadband THz characterization of the material samples.

THz-TDS is a coherent detection of the terahertz pulses in the time domain, where the electric field of the THz pulses is measured with respect to time. Unlike other optical detection, THz-TDS technique has a greatest advantage of measuring both amplitude as well as phase of the THz pulses. Thus, it helps to retrieve the complex nature of the dielectric properties like complex permittivity and complex conductivity of the sample material. THz-TDS technique is a non-ionizing and non-destructive measurement technique, because of their low energies and relatively slow oscillation speeds. Now there are several approaches in generating and detecting the THz radiation using the photoconductive antennas, nonlinear crystals and quantum cascade systems[15, 16]. Here, we focus on the THz-TDS system involving the GaAs based photoconductive antenna and nonlinear crystals (mainly ZnTe) for generating and detecting the THz pulses, which will be employed in the THz characterization of the MM samples throughout the thesis.

### 1.1.1 Photoconductive Antenna based THz-TDS system

The photoconductive switch (also termed as Auston switch)[7] based THz generation and detection is one of the widely used THz-TDS system that exhibits remarkable signal to noise ratio (10000:1). Figure 1.2 illustrates the pulsed THz generation and detection processes by optically pumping the voltage biased photoconductive antenna using 800 nm ultrafast optical pulses possessing high repetition rate. At the emitter side, a pair of 10 $\mu$m width metal electrodes separated by $L = 80$ $\mu$m are placed on the photoconductive substrate (low temperature-GaAs) and biased with a $DC$ voltage of 70 $V$. As the ultrafast laser pulse with photon energy greater than the energy band gap of the semiconductor is illuminated at the gap of the semiconductor, the photo-induced free carriers are generated in the substrate. These photo-carriers generated in the gap area are accelerated by the biased DC voltage ($\mathbf{V}$) that generates the photocurrent across the two electrodes, thereby creating a time varying current density $\mathbf{J}$(t) given by,

$$\mathbf{J}(t) = \mathbf{N}(t) e \mu \mathbf{V} \tag{1.1}$$

where, $e$ and $\mu$, respectively are the charge and mobility of photo-excited electrons, $\mathbf{V}$ is the bias voltage and $\mathbf{N}$(t) is the time varying photo-carrier density. The time varying current density $\mathbf{J}$(t) generates the terahertz pulse in the far-field, whose electric field amplitude is given by,

$$\mathbf{E}_{THz} = \frac{Ae}{4\pi\epsilon_0 c^2 z} \frac{\delta \mathbf{N}(t)}{\delta t} \mu \mathbf{V} \tag{1.2}$$

where, $A$ is the area of the photo-illuminated gap, $z$ is the far-field probe's position from the THz source. From the expression, it is clear that the strength of the THz radiation proportional to the area ($A$) of illumination and the electric field bias ($\mathbf{V}$), thereby electric energy stored in the gap area ($A$) rather than the energy of the optical

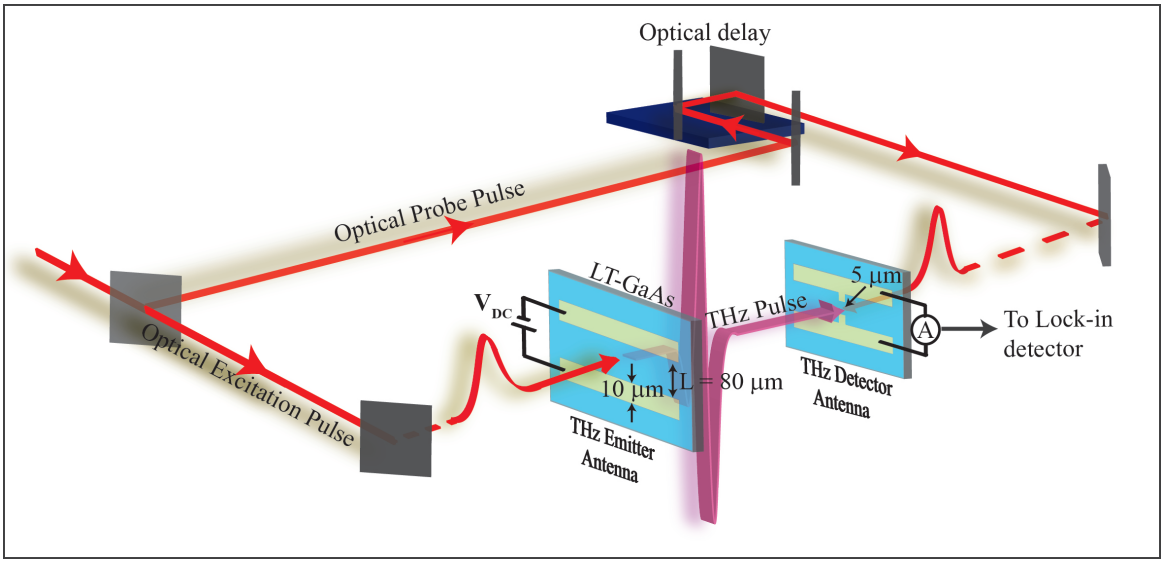


Figure 1.2: Schematic of Photoconductive antenna based THz-TDS system.

pulse is strongly accountable for the energy of the THz radiation. Linear dependence on the time varying charge carrier generation requires more photo-carrier generation is required for the strong generation of the THz waves. The equation [1.2] is only valid in the weak excitation regime, where the optical pulse excitation just acts as the trigger to the release of the electric energy stored in the gap of the antenna in the form of THz radiation.

At the detector side, mechanisms involved in detecting the THz pulse are almost similar to the processes observed at the emitter side. However, instead of using the external voltage bias, the incident THz field acts as the bias field in generating the current density in the semiconductor, which is collected by a current sensor connected across the electrodes. An optical probe pulse is used to map the THz pulse by controlling optical time delay ($\tau$) between the optical probe pulse and the THz pulse using a delay stage. The photo-excited carriers are driven across the electrodes using the THz field that generates the photocurrent ($\mathbf{J}_d$), which is proportional to the electric field of the THz wave.

$$\mathbf{J}_d = \mathbf{N}_d e \mu \mathbf{E}(\tau) \tag{1.3}$$

$\mathbf{E}(\tau)$ represents the temporally mapped electric field of the THz waveform as a function of time delay $\tau$. Since the THz-TDS allows measuring the electric field of the THz wave rather than its intensity, the measurement retrieves both the amplitude and phase of the THz pulse, thereby allowing the direct measurement of complex optical constants of the material that are not possible to retrieve using the other optical techniques. The performance of photoconductive based THz-TDS system is majorly dictated by the short carrier lifetimes of the substrate, geometry of the antenna, intensity of the excitation pulse and the bias voltage. The semiconducting materials such as low temperature gallium arsenide (LT-GaAs) and ion implanted silicon on sapphire (SoS) with high quantum efficiency and ultrafast carrier lifetimes ($<$ 1 ps) are mainly used as the emitter and the detector substrates. The separation ($L$ = 80 $\mu$m) between the electrodes along with the refractive index of the emitter substrate determines the central frequency of the THz wave, determined by the formula,$f_0 = \frac{c}{2Ln}$. Active area of antenna gap between the electrodes will play a crucial role in deciding on the values of bias voltage and the intensity of the excitation pulses. Large area of the gap results in higher power of THz pulses and also increases the breakdown threshold for the dielectric properties of the semiconducting substrate. The bias voltage and the intensity of the excitation laser pulse dictate the strength of the THz signal that are limited by the damage threshold for dielectric properties of the semiconductor. Higher laser intensity causes in the thermal breakdown of the antenna that causes the heating of the substrate through laser power, which results in its low resistance and higher photocurrent though the antenna. Whereas, if the voltage bias (V) is greater than the breakdown field of the semiconductors ($4 \times 10^5$ V cm$^{-1}$ for GaAs), it results in the dielectric breakdown of the semiconductor thereby affecting the performance and lifetime of the photoconductive antenna.

The time domain waveform and the corresponding Fourier transformed frequency spectrum of the terahertz pulse generated and detected using the PC antenna are

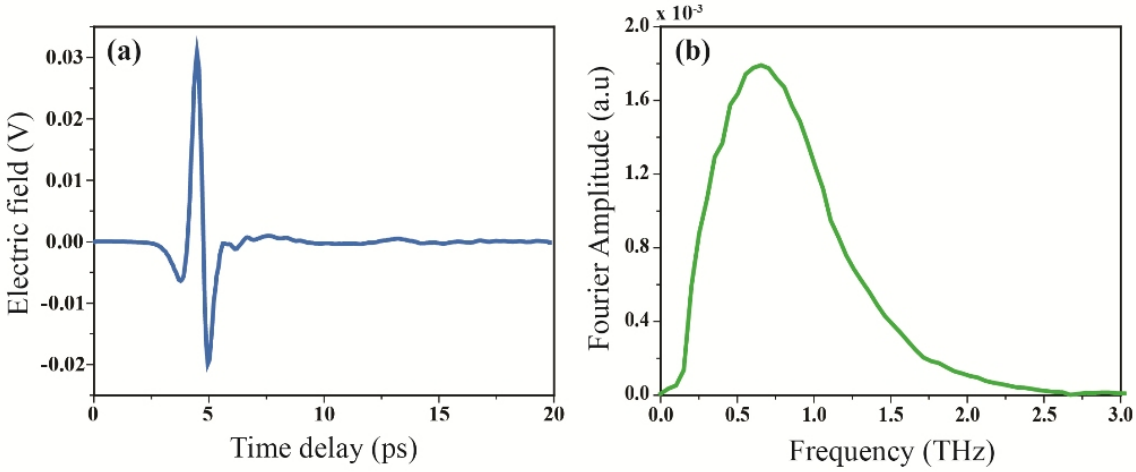


Figure 1.3: (a) Measured transmission time domain signal obtained in $N_2$ environment using PC antenna based THz-TDS system. (b) Corresponding fast Fourier transformed (FFT) THz spectra showing nearly 2 THz bandwidth of the setup.

shown in Fig 1.3 (a) and (b), respectively. For the sample, THz-TDS measurements are done in two steps. First, the THz scan is performed on the sample (metal structures on the dielectric substrate), which is referred to as 'sample signal'. Then subsequently, a separate THz-TDS scan is carried out for the plane dielectric substrate that is referred to as 'reference signal'. Later, the transmission spectrum of the sample is obtained by normalizing the Fourier transformed signals of the sample ($\mathbf{E}_S(\omega)$) and the substrate ($\mathbf{E}_R(\omega)$) and is expressed as,

$$|T(\omega)| = |\frac{E_S(\omega)}{E_R(\omega)}| \tag{1.4}$$

All our THz-TDS measurements are performed in dry nitrogen ($N_2$) environment to avoid the possible vibrational resonances and strong THz absorption of the water vapors that may greatly affect the results.

### 1.1.2 Optical pump-Terahertz Probe (OPTP) spectroscopy using ZnTe based THz-TDS system

Although the photoconductive antenna based THz system provides very low noise signals with better stability and considerable bandwidths, but have lower peak powers. The nonlinear crystal systems can generate THz pulses with high peak powers and longer bandwidths. Since generation and detection of the THz waves using the nonlinear crystals involve amplified laser systems of high pulse energy of low repetition rates (1 kHz), it facilitates to realize more robust optical-pump terahertz-probe (OPTP) spectroscopic system. OPTP spectroscopy is also termed as transient THz spectroscopy or time resolved terahertz spectroscopy (TRTS). It offers an exciting tool to measure the transient non-equilibrium dynamics in the materials under the influence of a pump beam. The optical pump beam with higher photon energy and higher intensities is typically used as the pump beam, whereas the THz beam with low energies and powers is used to probe the dynamics in the material system. In our studies, we employ the OPTP system to probe the dynamic tuning of MM resonances in a hybrid semiconductor-metamaterial system along with unveiling the ultrafast relaxation dynamics of prominent semiconducting materials. The OPTP spectroscopic system used in our measurement is based on the THz generation using zinc telluride (ZnTe) nonlinear crystal, which is integrated with the high intense optical pump pulse. In this section, we go through the basics on the generation and detection of the THz waves using the ZnTe crystal and its integration with the optical pump beam that facilitates the OPTP measurements of the semiconductor-metamaterial hybrid sample.

Generation of THz pulses in the ZnTe nonlinear crystals is based on the optical rectification method, where the $< 110 >$ axis cut ZnTe crystal is pumped by a 120 fs laser pulse of wavelength 800 nm under favorable phase matching conditions. ZnTe

crystal is nearly transparent to optical wavelengths around 800 nm and higher THz wavelengths ($> 50$ $\mu$m), and shows good nonlinear properties at 800 nm. It is a noncentrosymmetric crystal with large 2nd order nonlinear susceptibility ($\chi^{(2)} = 1.6 \times 10^{-7} m/V$) and high electro-optic coefficient $r_{41} = 4.04$ pm/V. The efficiency of THz generation through ZnTe strongly depends on the thickness and orientation of the crystal, wavelength and the intensity of the incoming optical pump beam. Optical rectification is a non resonant nonlinear process and since the crystal must have higher $\chi^{(2)}$, only non-centrosymmetric nonlinear systems can be used to generate THz emission. When the ultra short pulses with electric field $E(t) = \sqrt{I(t)}e^{-i\omega t}$ (where, $\sqrt{(I(t)} = E_0 e^{-at^2}$) propagates through the nonlinear crystal, it creates a time varying second order nonlinear polarization within the crystal ($\mathbf{P}^{(2)}(t) = \mathbf{P}_0 e^{-2at^2}$). This, time varying polarization produces the THz radiation, whose electric field is given by,

$$\mathbf{E}_{THz} \propto \frac{\delta^2 \mathbf{P}^{(2)}}{\delta t^2} \tag{1.5}$$

Other nonlinear processes such as SHG can compete with the optical rectification process to decrease the efficiency of the THz emission. But these effects will only dominate at higher intensities of the excitation pulses and reduce the efficiency of the THz generation.

The THz detection is performed using the free space electro-optic sampling (FSEOS) technique, where the polarization change in the low intense optical beam due to the influence of THz electric field is used to map the waveform of the THz pulse using the balanced photo-detector. This technique exploits the Pockel's effect of the birefringent nonlinear crystal (ZnTe), where the strong electric field can induce anisotropy in the crystal to change the polarization of the optical beam passing through the crystal. FSEOS process is summarized in the figure 1.4. Upon time matching the group

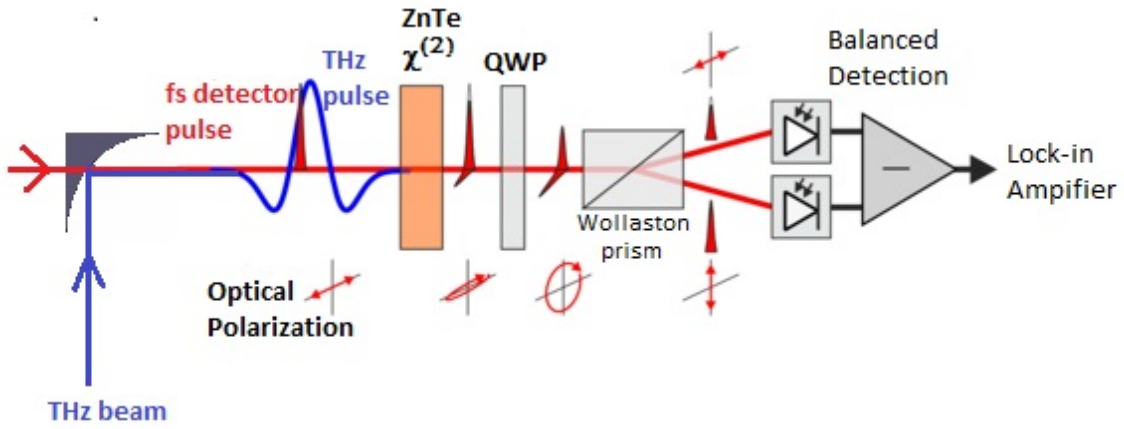


Figure 1.4: Schematic showing Free space electro-optic sampling (FSEOS) using a ZnTe crystal[17].

velocity of the optical pulse with the phase velocity of the THz pulse inside the ZnTe crystal, the THz pulse acts as a constant DC electric field on the optical probe pulse. This induces a small birefringence in the system that happens near 800 nm for the ZnTe crystal. Thus, in the presence of the THz electric field, the linearly polarized optical pulse experiences rotation in its polarization after passing through the crystal. This change in the polarization of the optical pulse is recorded via performing polarization sensitive balanced detection. Before THz pulse arrives on the ZnTe crystal, the polarization of the optical pulse is linear and by using the combination of QWP and Wollaston prism that splits the circularly polarized light into orthogonally polarized lights with equal intensity, the output signal from the balance detector is made zero. Output signal from the balance detector is measured as the difference between the intensities of two orthogonally polarized beams. As THz pulse ($E_{THz}$) strikes the crystal, it rotates the polarization of the optical pulse that in turn changes the signal on the balance detector. This change in the signal strength is proportional to the amplitude of THz pulse $E_{THz}$ falling on the ZnTe crystal. Since the wavelength of THz pulse is much longer than the optical pulse, only small part of the THz pulse is measured at one time. So by varying the relative time delay between

the optical pulse and the THz pulse using a variable delay stage, the entire THz pulse profile can be traced.

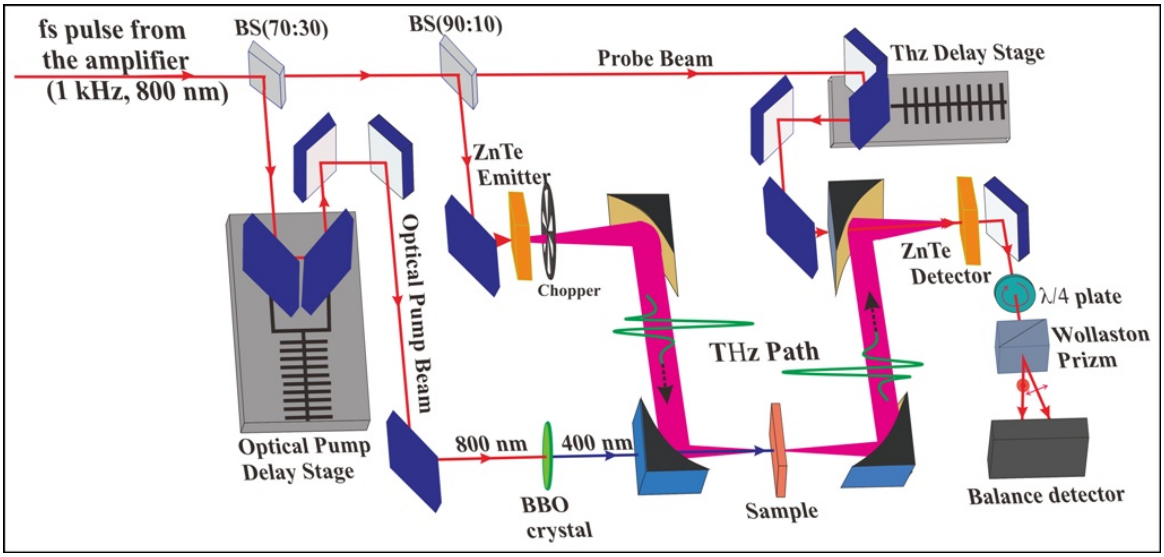


Figure 1.5: Schematic of ZnTe nonlinear crystal based OPTP THz-TDS system.

Figure 1.5 depicts the experimental scheme of ZnTe based THz-TDS spectroscopy integrated with the optical pump beam. Ultra short laser pulse of pulse-width 120 fs from an amplified ultrafast laser is split into two using the beam splitter (BS, 70:30), where one part (transmitted) is derived for the generating and detecting the THz waves using the ZnTe crystal, while the other part of the beam (reflected) is taken for pumping the sample during the pump-probe measurements. The transmitted beam is further split into two using a beam splitter (BS, 90:10), where the reflected beam hits the ZnTe (emitter) crystal to generate the THz pulses via the above discussed optical rectification process, whereas the transmitted beam is used to map the THz pulse via FSEOS process at the detector end. THz emitter crystal generates diverging THz beam that is collimated using a parabolic mirror just after the emitter crystal, which is collimated using an off axis parabolic mirror. Collimated THz pulse is focused on the 'sample' using another parabolic mirror. Thus, by using two pairs of parabolic mirrors, THz beam is guided to the detector via the sample. At the detector end,

a low power femtosecond optical beam that is time matched with the THz pulse is sent through the ZnTe (detector) crystal. Change in the polarization of the optical beam is recorded via electro-optic sampling (FSEOS) method and the time domain voltage signals are recorded using lock-in detection technique, which is synced to a LabView program. In the post processing step the recorded time domain signals are Fourier transformed to extract the amplitude spectrum of the signal. During the OPTP measurements, the optical pump is time matched with the THz probe pulse at the sample position using a variable delay stage that helps in scanning the relaxation life time of the photo-excited electrons in the sample.

## 1.2 Metamaterials

The response of the electromagnetic wave with the medium is governed by the Maxwell's equations,

$$\begin{aligned} \vec{\nabla} \cdot \vec{\mathbf{E}} &= \frac{\rho}{\epsilon}, & \vec{\nabla} \cdot \vec{\mathbf{B}} &= 0 \\ \vec{\nabla} \times \vec{\mathbf{E}} &= \frac{-\partial \vec{\mathbf{B}}}{\partial t}, & \vec{\nabla} \times \vec{\mathbf{B}} &= \mu \vec{J} + \epsilon\mu \frac{\partial \vec{\mathbf{E}}}{\partial t} \end{aligned} \tag{1.6}$$

Where, $\epsilon$ and $\mu$ are respectively, the relative permittivity and permeability that characterize the optical response within the medium. Based on the effective permittivity and effective permeability of the medium, materials can be classified in to four different classes as described by the $\epsilon - \mu$ diagram given by the figure 1.6. Metamaterials (MMs) being artificially engineered materials, they can be designed to show the properties of purely electric (cut wires, Region II), purely magnetic (split rings, Region IV) and simultaneous electric and magnetic properties (cut wires + split rings, Region III). A specific class of MM called left-handed materials possessing negative effective parameters (falls in Region III of $\epsilon - \mu$ diagram) have shown to

exhibit unusual properties[18] that are not found in nature, such as negative refraction, reversal Snell's law, negative group velocities in the resonant MM media.

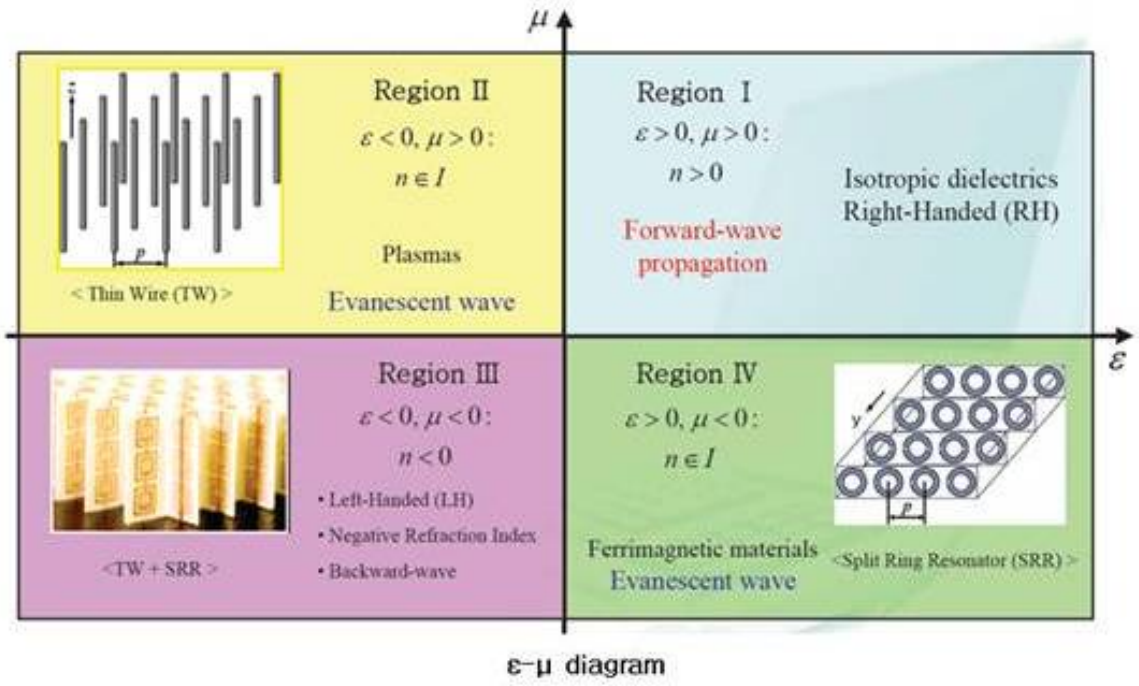


Figure 1.6: Characterization of material properties using $\epsilon - \mu$ diagram. MMs fall in the 3rd quadrant (Region III) of the $\epsilon - \mu$ diagram, where both $\epsilon$ and $\mu$ are negative. *(Source: Internet)*

Although the field of MM research has shown huge growth over the years, there is no unique definition termed to define the word metamateral. The current MM study falls in the definition given in the W. Cai and V. Shalaev book on Optical Metamaterials[19], "A metamaterial is an artificially structured material which attains its properties from its sub-wavelength unit structure rather than its constituent materials". Metamaterial constitutes sub-wavelength sized metal resonators (called meta-atoms) which are periodically arranged on a dielectric substrate. As depicted in figure 1.7, periodicity of the unit cell in MM structure is smaller than the wavelength of the incoming light ($\frac{\lambda}{p} > 1$) that separates the MM from other artificial periodic structures like photonic crystals. Since the size of the meta-atoms are smaller than the wavelength, the incoming light sees the MM system as an effective homogeneous

medium and the total electromagnetic response from the MM is considered as an average response of the collection of constituent unit cells.

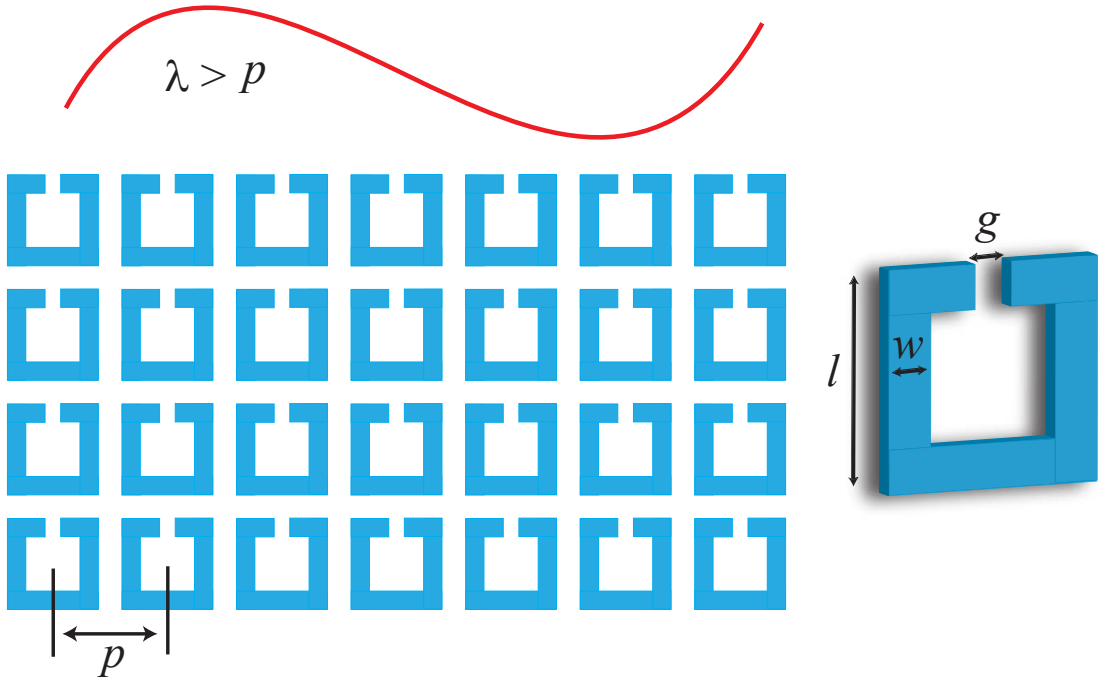


Figure 1.7: Periodic arrangement of MM unit cells (SRRs) showing the sub wavelength behavior of MM ($p < \lambda$). Geometry of split ring resonator (SRR) unit cell, where $g$ is the capacitor gap, $w$ and $l$ are the width and length of the metal arms.

Electromagnetic MMs[20, 21] exhibit extraordinary properties over a large portion of electromagnetic spectrum, whose resonance features are strongly dictated by their geometry and size rather than the composition of constituent materials. The unprecedented advantage of these structures comes from their subwavelength size, their scalability and ability to capture and manipulate the finest near field information present in the system. Near field is the most dominant component of the scattered fields closer to the object surface that fails to radiate freely to the far field. Due to its omnipresent nature and the finest information it entraps, near field has proved to be a vital component in the light-matter interactions. Manipulating the near field in MMs[22] has yielded opulence of remarkable phenomena including the perfect lens[23, 24], negative index[25], artificial magnetism at terahertz frequencies[26], plas-

monic mode hybridization[27, 28] and many more. The near field coupling and their precise manipulation has resulted in sharp resonance features such as Fano resonance feature[29–32] and classical electromagnetically induced transparency resonances[33–36], which are very well exploited in the applications such as sensors[37–39], lasing spasers[40, 41], slowlight[42–45] and in enhancing the nonlinearity[46, 47] in the MM medium. These sharp resonances in MMs result from the Fano type of destructive interference mechanisms between the bright (radiant) and the dark (sub-radiant) modes of the MM structures. The focus of the thesis is in probing and manipulating the radiant and sub-radiant near field interactions in a MM, microelectromechanical systems (MEMS) MM and semiconductor-metamaterial hybrid systems that promises interesting phenomena and applications in the terahertz part of the electromagnetic spectrum.

As given by the definition, MM response is determined by the geometry and periodic arrangement of the unit cells that determines the effective $\epsilon$ and $\mu$ of the MM system. Thus, the shape and size of the MM unit cells (referred to as meta-atoms) define the resonant properties of the entire structure. A meta-atom resonating at the frequency ($f$) can be a designed by using the expression,

$$f_m = m\frac{c}{2ln} \tag{1.7}$$

Where $m$ = 1,2,...,$m$ is the $m$th mode of the resonator and c is the speed of light in vacuum. The resonant frequency of the MM is dictated by the product of two times length ($l$) of the resonator and the refractive index ($n$) of the dielectric substrate. The lowest order mode ($m = 1$) of the MM resonance is called the 'LC resonance' and the lowest even order resonance mode ($m = 2$) is termed as the 'dipole resonance' mode. LC mode can be excited in split ring resonator (SRR) structures, where the incident electric field component is parallel to the gap ($g$) of the split ring resonator whereas, for

the other orientation of the electric field component the dipole nature of the resonance is seen at the higher frequency. SRR is the most fundamental and commonly used MM structure that consists of a conducting metallic loop with a small gap ($g$) at one side of the ring (figure 1.7). The resonant properties of the SRR are determined by its size and the orientation of the gap with respect to the incident electric field. The physics of the resonance properties can be optically analogued to a simple LC-oscillator circuit, where the loop of the SRR provides a self inductance (effective $\mu$) and the SRR gap gives the effective capacitance (effective $\epsilon$) in the system. Hence, the resonance frequency of the lowest order mode of the SRR is given according to the basic LC resonant electronic circuits, $f_0 = \frac{1}{2\pi\sqrt{LC}}$ . Therefore, the fundamental mode of the SRR is termed as the 'LC mode' or the 'SRR mode'.

Since the resonance of the MM depends on the size ($l$) and shape of the meta-atom, it helps us to design these sub-wavelength structures at any desired frequencies we want. Our interest lies in the resonance properties of these MMs at terahertz frequencies ($f$ = 0.3 - 3 THz/ $\lambda$ = 100 - 1000 $\mu$m) of the electromagnetic spectrum, thus the resonators of length $l$ = 10 - 100 $\mu$m are designed to study the resonant and non-resonant interaction of MMs at the terahertz frequencies. The recent innovations in THz MMs have played an important role in eliminating the existed THz gap by providing MM based emitters[48, 49], detectors[50, 51] and many optical components such as MM based waveplates[52, 53], modulators[54–56] and lenses[57] in the terahertz frequencies that have enhanced the interactions and manipulation of THz waves. We use the commercially available numerical solver called Computer Simulation Technology (CST) microwave studio to design and numerically model the MM structures at terahertz frequencies. Metamaterials fabrication at THz frequencies involves the photolithography techniques to assemble metallic wires of sub-wavelength structures on a dielectric surface, which will be discussed in later part of the chapter. The optical characterization of these structures at terahertz frequencies is carried out

using the photoconductive switch based THz-TDS system.

### 1.2.1 Microelectromechanical system (MEMS) based reconfigurable metamaterials

The ability of MMs to tune the optical and the near field characteristics by changing the shape and size of the MM gives an unprecedented advantage to manipulate the light matter interactions across wide range of electromagnetic spectrum. In conventional MMs, to alter their structural or optical properties, it requires to fabricate a new set of devices with slightly different structural configuration that allows the tunability of the optical response in the device. This limitation of not able to control the optical characteristics in the device in real time would potentially hinder the role and reliability of MM devices in the practical applications. Hence, it is important to establish real time active and dynamic control over the structural reconfiguration of the MM resonators in order to enhance their technological and real world applications.

In the recent years, there are numerous works establishing the dynamical reconfiguration of the MM devices using external stimuli such as thermal[58], magnetic[59], electric[60, 61] and optical pulses[62] across microwaves to optical frequencies. These reconfigurable metadevices possess a unique advantage of real time control in manipulating the near fields by exploiting the sensitive changes in the optical properties of the MMs to their micro/nano scale movements, which makes them more resilient and merits their applications as future generation state-of-the-art metadevices. Depending on the design, fabrication constraints and size of the resonators, different reconfiguration techniques are being used across the spectrum. Here, in the scope of the thesis, we study the voltage actuated micro-electro-mechanical systems (MEMS) based MM devices and optically reconfigurable semiconductor-metamaterial hybrid systems.

These devices possess favorable dimensions of the resonators that can be realized using well known fabrication techniques that include the conventional photolithography process at terahertz wavelengths. Micro-electro-mechanical systems (MEMS) are recently the trending research area in the field of material fabrication and the opto-electro mechanical devices. MEMS are a class of micro-actuators, whose mechanical/electrical properties can be controlled by an external stimulus such as temperature, electrostatic or the optical stimulus. They can be fabricated in nano/micro scales enabling them to be perfect candidates for realizing active and tunable metamaterials possessing real time control over the near- and far-field optical properties in MM. They possess unique advantage in active manipulation of the near fields in all the three spatial directions by exploiting sensitive changes to their micro/nano scale movements, which makes them more resilient and merits their applications as future generation state-of-the-art active photonic devices. They mainly operating in the terahertz (THz) to near-infrared frequencies and have enabled dynamic manipulation of range of THz properties such as magnetic response, transparency, near-perfect absorption and THz anisotropy.

The process of the MEMS operation(actuation)[63] is summarized in the figure 1.8. To electrically actuate the metallic cantilevers, a DC biased voltage is applied between the silicon substrates and the metallic structures (Fig. 1.8(a)). When voltage is applied across the released cantilevers and Si substrate, the attractive electrostatic force ($F_E$) deforms the suspended cantilevers towards the fixed Si substrate. This mechanical deformation of cantilevers induces a restoring force ($F_R$) in the deformed cantilever that opposes the electrostatic force ($F_E$), which caused the deflection in the first place. Thus, the balance between the electrostatic force and restoring force decides the final position of the cantilever for a given voltage. As $V_{DC}$ increases further, the electrostatic force ($F_E$) increases much faster than the restoring force ($F_R$), and at a critical value known as the“pull-in voltage ($V_{PI}$), the magnitude of

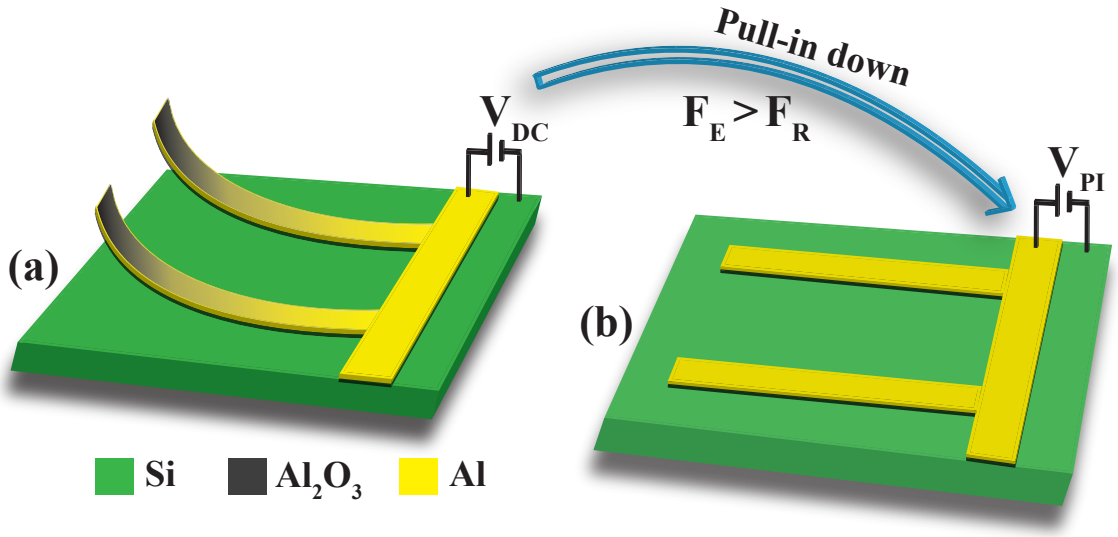


Figure 1.8: Shows the MEMS based MM unit cell structure. (a) OFF-state (released-state) of the cantilever, where the $V_{DC} < V_{pi}$ . (b) Is the ON-state for cantilever, when the DC applied voltage $V_{DC} < V_{pi}$ .

electrostatic force will exceed the restoring force (i.e. $F_E > F_R$), thereby bringing the microcantilevers in physical contact with the Si substrate (Fig. 1.8(b)).

## 1.3 Numerical Simulation Solver: CST-Microwave studio

This section describes the principles and techniques behind the numerical simulations that are commonly used to design and model the MM resonators at THz frequencies. We use commercially available software called Computer Simulation Technology Microwave Studio (CST-MWS) to design and simulate the electromagnetic responses in the resonant MM sample. This is in general a Maxwell equation solver that uses the Finite Integral Techniques (FIT) or the Finite Difference Time Domain (FDTD) techniques to solve the integral form of Maxwell's equation with appropriate boundary conditions. Maxwell's equations in the integral form are given by [64],

$$\begin{aligned} \oint_{\delta V} \overrightarrow{\mathbf{D}} \cdot d\overrightarrow{s} &= \int_V \rho \cdot d\mathbf{V}, & \oint_{\delta V} \overrightarrow{\mathbf{B}} \cdot d\overrightarrow{A} &= 0 \\ \oint_{\delta A} \overrightarrow{\mathbf{E}} \cdot d\overrightarrow{s} &= -\int_A \frac{\partial B}{\partial t} \cdot d\mathbf{A}, & \oint_{\delta A} \overrightarrow{\mathbf{H}} \cdot d\overrightarrow{s} &= \int_A (\frac{\partial D}{\partial t} + J) \cdot d\mathbf{A} \end{aligned} \tag{1.8}$$

On the other hand, CST-MWS offers the CAD design environment to draw the desired structures those needed to be simulated. Most commonly used materials such as metals (aluminium, gold, etc) and dielectrics (silicon, quartz, etc) can be found in the material library of the CST software. Even though the materials show frequency dependent conductivity properties, the materials in CST library are characterized by their dc conductivity values that hold a good approximation at Terahertz frequencies for the thin metal films. CST environment provides two types of solvers to model the resonant MM structures; one being the Frequency domain solver that and the other being the Transient solver. Although both gives the similar output parameters, the basic difference lies in their process of solving the Maxwell's equations (Eqn. 1.8). Basically, they use different type of boundary conditions and approximations to solve the Maxwell's grid equations which will be discussed in detail in the following paragraphs.

### 1.3.1 Frequency Domain Solver

Below is the work flow for the Frequency Domain Solver and we will go through them in detail one by one.

1. Set the desired frequency and length units for the solver and set the background environment to normal ($\epsilon = 1$).

2. Set the frequency range of interest for the simulation.

3. Design the MM unit cell structure using the available CAD environment.

4. Set the appropriate boundary conditions.

5. Define the input and output waveguide ports.

6. Generate/construct mesh: Meshing.

7. Run the Frequency domain solver.

After designing the MM unit cell of desired dimensions and defining the frequency range for the simulation, the next step is to apply the proper boundary conditions to the structure to exactly model the periodicity of MM. Frequency domain solver uses 'Unit Cell' boundary conditions in the X-Y plain to efficiently model a MM unit cell as an infinite array of antennas by considering all the possible edge effects. In the Z direction the boundary condition is 'open' as it represents propagation axis of the light. In the $Z_{max}$ (+Z) direction it is important to use 'open (add space)' boundary condition to prevent the simulator in considering the fringing fields effects generated near the metallic surface when the resonance is excited. The necessary gap to avoid these fringing field effects that not to be considered during the simulation, is of the order of $\lambda/8$, which is set as default in the CST-MWS.

To solve the Maxwell's equations (Eqn. 1.8) numerically, the simulation domain must be divided into small grids called 'mesh'. To achieve the accurate simulation results with better resolution, the mesh size should be smaller than the smallest of the structure of interest and the mesh size should be considered smaller than (quarter the wave length) the characteristic wavelength of the structure. There is a trade-off between the simulation time and the resolution. More number of meshes (smaller mesh size) increases the accuracy of the results and on the other hand it increases the solver time as well. It is up to the user to define the number of mesh depending on the requirements on the simulation resolution and accuracy.

By applying the mesh, the integral form of the Maxwell's equations given in Eqn. 1.8 are converted into discrete matrix representations,

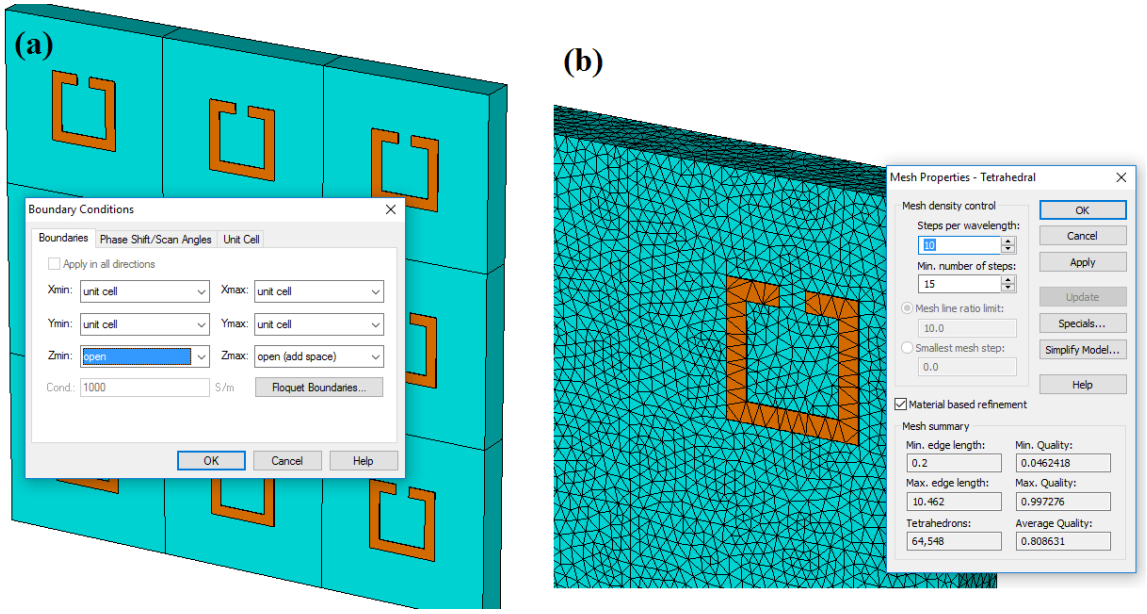


Figure 1.9: Parameter windows for setting the (a) boundary conditions and for performing (b) mesh adaptation process in CST-MWS Frequency solver simulator.

$$\begin{aligned} \widehat{S}\ d &= q, & \widehat{S}\ b &= 0 \\ \widehat{C}\ e &= -\frac{\partial b}{\partial t}, & \widehat{C}\ h &= \frac{\partial d}{\partial t} + j \end{aligned} \tag{1.9}$$

These equations are called the Maxwell's grid equations (MGEs), where $\widehat{S}$ and $\widehat{C}$ are the discrete sign matrices. Once the mesh is defined, the frequency domain solver converts the MGEs into their Fourier equivalent i.e. $\partial/\partial t \longrightarrow i\omega$. Later on the Fourier transformed MGEs are solved point by point (mesh by mesh) in frequency domain. The output results are displayed in the S-Matrix or S-parameters that comprise of complex transmission and reflection coefficients for all the calculated modes. Frequency domain solver that uses finite difference time domain (FDTD) methods to solve the Maxwell's grid equations (Eqn. 1.9) is highly efficient for simulating the narrow bandwidth structures or the highly resonant structures with localized frequency response. On the other hand, the time domain or transient solver uses 'periodic' boundary conditions and 'hexahedral mesh' type to solve the MGEs

(Eqn. 1.9) in time domain using the Finite Integration Technique (FIT). In this method the time derivatives are approximated by finite time differences $\Delta$t and solved temporally using the leapfrog scheme. The size of $\Delta$t greatly affects the stability and accuracy of the simulation and its value is related to the spatial dimensions of the mesh grid. This variable is set default by the CST solver and rarely needs to be changed by the end user. The transient solver environment is similar to the experimental situation, where in both the cases the electric field response is calculated/measured in time domain. Later, the obtained time signal is frequency converted using FFT in the post processing steps. Transient solver is ideal to model the higher bandwidth/higher frequency structures and also better simulator to consider if the accuracy is not a concern, as it takes less time for the solver to complete the simulations compare to Frequency solver.

### 1.3.2 Interpretation of the simulated data

The simulated results are characterized by s-parameters, which relate the outgoing waves to the incoming waves through a scattering matrix (S-Matrix) given by,

$$\begin{bmatrix} O_1 \\ O_2 \end{bmatrix} = \begin{bmatrix} S_{11} & S_{12} \\ S_{21} & S_{22} \end{bmatrix} \begin{bmatrix} I_1 \\ I_2 \end{bmatrix}$$

$S_{11}$ is the reflection coefficient and $S_{12}$ is the transmission coefficient at Port 1 of the waveguide, whereas $S_{21}$ and $S_{22}$ are respectively the transmission and reflection coefficients at the Port 2 of the waveguide (figure 1.10). The obtained s-parameters in CST are complex that contain both amplitude as well as phase information of the signals. By default the calculated s-parametars are normalized to the port impedence. The expression given by above matrix equation, is for two ports, in case if the user requires full S-matrix one may choose 'All Ports' option while performing the simulation. The solver will excite the material with the Gaussian pulse in the time

domain and the out put power will be normalized to a frequency independent power of 1 W.

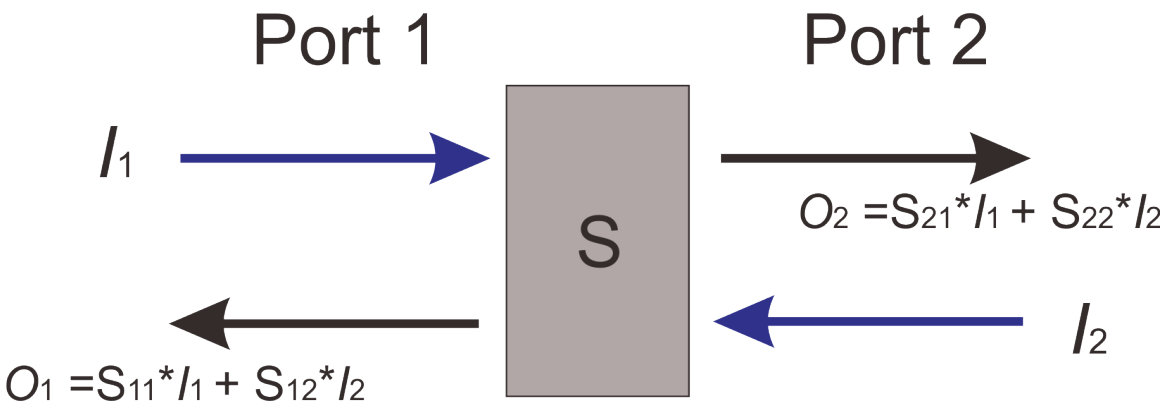


Figure 1.10: Represents a two port network showing two dimensional scattering parameters.

### 1.3.3 Simulating the Electromagnetic fields

Apart from providing the S-parameters, CST-MWS offers a direct visualization of the 2D and 3D electromagnetic field distribution in the region of interest. The simulation parameters help us to extract the entire range of electric and magnetic properties of the system. Local charge distributions and the surface current densities can be obtained at any desired frequencies by running the simulations for previously described boundary conditions. For the MM structures, where both the electric and magnetic responses can be seen, these field distributions serve the most in analyzing and interpreting the observed resonant and non resonant phenomenon. The simulated field distributions help us in explaining the nature of near field coupling in the system. Strength and phase of the trapped electric and magnetic fields on the metallic structures of meta-atoms dictates the nature of coupling in the near field regime and thus the transmission characteristics. The detail work flow for simulating the electromagnetic fields can be found in CST-MWS tutorial.

### 1.3.4 Sources for discrepancies between the numerical simulations (CST-MWS) and the experimental results

Despite the fact that numerical simulations model the experimental results with great accuracy, there will be some discrepancies in the observed and the simulated results due to following likely errors.

1. Defined material parameters on CST will be slightly different from the materials used in reality.

2. The background of the simulation can be different from the real experimental situations.

3. Material dimensions may vary during the fabrication process that may show slight offset resonant behaviors from the simulated one.

4. There could be geometrical errors arising in the simulations due to the inaccuracy in defining the number of mesh.

Considering all these possible errors into account the CST-MWS numerical solver give the most accurate results and has become an exceptional tool in modeling the MM resonators and has contributed immensely in the growth of MM research especially in the terahertz regime. In the following studies, we use frequency domain solver to numerically simulate the MM structures, as it provides much accurate resolution considering the smaller mesh size and unit cell boundary environments.

## 1.4 Metamaterial Fabrication Process

At terahertz part of the electromagnetic spectrum, the MM structures possess microscale dimensions that can be easily fabricated using the conventional lithography techniques that include electron beam lithography and UV photolithography techniques.

In our study, we employ UV light illumination based photolithography technique followed by thermal metallization, which is the most commonly used fabrication technique in realizing the terahertz MM structures. In the course of the thesis, three types of MM designs are being probed that includes conventional MM structures, MM structures on silicon on sapphire (SoS) substrates and MEMS based MM structures. All these structures are fabricated using the conventional photolithography process in addition to reactive ion itching techniques for the samples on SoS and the MEMS MMs.

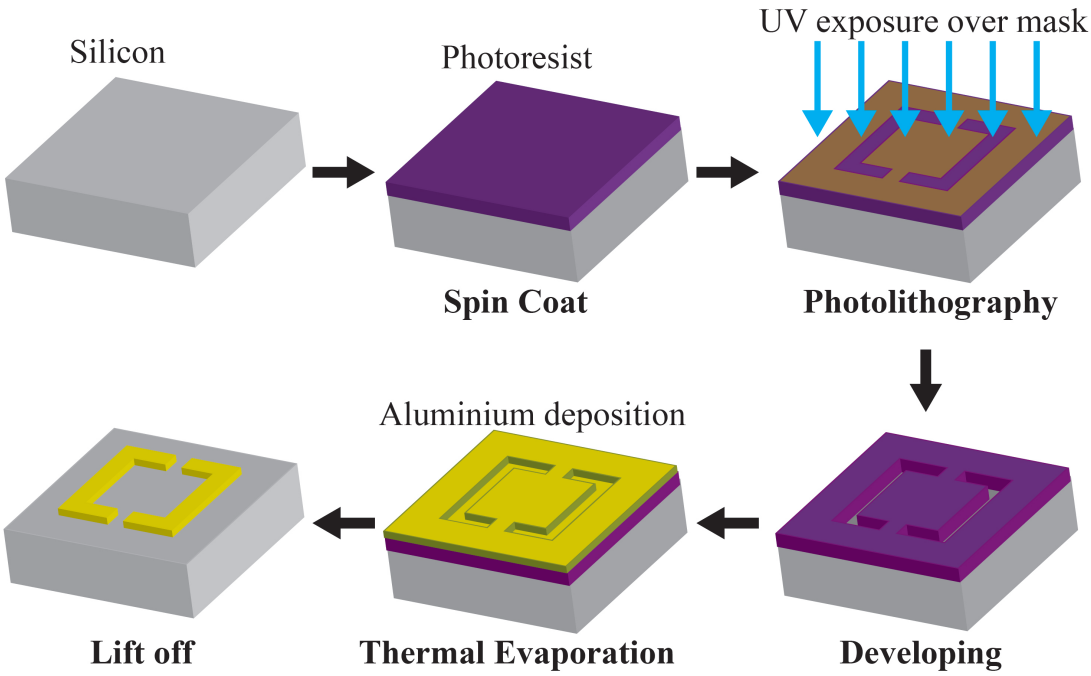


Figure 1.11: Conventional photolithography fabrication process using thermal evaporation technique for metal deposition and liftoff method to dissolve the photoresist.

The planar MM structures are fabricated using the conventional photolithography process followed by the thin metal layer deposition using the thermal evaporation technique and finally the MM pattern is obtained after the lift-off process in acetone. Firstly, a photoresist of thickness 1.5 $\mu$m is spun coated at 3000 rpm for 30 s on the clean substrate and later baked in an oven for 15 mins at 115° C in order to evaporate

the solvent. The spun coated photoresist is covered with the mask and illuminated by the UV light. The mask basically contains the MM structures that allow the area of the MM structures on the photoresist is exposed to the UV light, thereby can be removed by the developer solution (AZ solvent). After the developing process, the aluminium (Al) metal of 200 nm thickness is deposited on the sample using thermal evaporation technique. As the last step, the Al deposited sample is dipped into acetone solution and the undesired aluminium metal deposited on the photoresist is removed through the lift-off process by dissolving the photoresist in acetone. In the case of active SoS samples, a second step photolithography was performed using a positive photo-resist to cover the split gap, followed by reactive ion etching (RIE) process to etch off undesired silicon from the sapphire surface. Finally wafers were soaked in acetone to remove photo-resist and to get desired MM structure. The resolution of photolithography technique is in few microns (2-3 microns), which is quite ideal for the MM fabrication at THz frequencies, whose dimensions are in few micrometers. The following figure 1.11 illustrates the fabrication steps of the MM structures using the conventional photolithography technique.

The MEMS MM samples are fabricated using the CMOS compatible techniques and materials that employs the conventional photolithography techniques to pattern the MM structures. Firstly, a 100 nm thick $SiO_2$ sacrificial layer is deposited on a cleaned and lightly doped silicon substrate suing low pressure chemical vapor deposition process. A first step of photolithography process is carried to etch off a part of the $SiO_2$ layer for the metal lines. Then a 50 nm of thick $Al_2O_3$ layer is deposited on the pattered $SiO_2$ sample using the atomic layer deposition process. As a next step, Al layer of required thickness is deposited using the sputtering technique. This subsequent deposition of Al metal and $Al_2O_3$ confirms that the bimorph Al/$Al_2O_3$ are in physical contact with each other and in contact with silicon at the metal line (anchor) region and in all the other regions, it is in contact with $SiO_2$ layer. Later,

a second step of photolithography is performed forming the desired pattern of MM structure followed by the dry etching of $Al/Al_2O_3$ bimorph layers. In the final step, vapor hydrofluoric acid (VHF) is used to isotropically etch-off the $SiO_2$ sacrificial layer, thereby leaving the suspended $Al/Al_2O_3$ bimorph cantilevers on the Si substrate. Since the bimorph layers possess residual stress, it causes the released resonators arms (cantilevers) to bend-up leaving a air gap between the $Al/Al_2O_3$ bimorph and the silicon substrate.

## 1.5 Scope of the thesis

Metamaterial research is a recent advance in the area of optics and photonics. THz MMs in particular are of greatest interest due to low material losses and ease of fabrication and strong display of magnetic interactions at THz frequencies. In THz MMs, near field effects arising due to their sub wavelength nature are dominated by both electric as well as magnetic nature of interactions. Controlling and manipulating the near field interactions in these MMs is a great deal of interest for the basic science as well as technological aspect of the structures. This thesis aims to unravel new physical phenomena in the THz MMs by tailoring the radiant and sub-radiant near field interactions in a passive and a dynamic way. Numerous interesting phenomena such as high Q-factor resonances, slow-light effects, resonant invisibility, logical operations, ultrafast THz modulators and formation of new type of quasi-particles interactions are efficiently probed and discussed in the scope of this thesis. These results offer useful applications to the real world technologies as sensors, optical routers in communication channels, modulators and various nonlinear and multifunctional electro-optical devices in the terahertz part of the electromagnetic spectrum. The focus of the thesis is on the various aspects of radiant (bright) and subradiant (dark) interactions in THz MMs, where the following chapters will show the various approaches on bright-dark

interactions and their influence on their near/far field optical characteristics under different structural configurations.

So far in this chapter, the overview and the technical concepts of the MMs, spectroscopic and the numerical tools and the fabrication methods for the MMs were discussed.

Chapter 2 discusses the classical interference mechanisms between the near fields in a concentrically structured split ring (SRR) and closed ring resonators (CRR). The strong near coupling between SRR and CRR results in a classical analogue of electromagnetically induced transparency effects such as MM induced transparency (MIT) showing a sharp transparency peak at the resonance. A theoretical framework based on the two-coupled oscillators (T-O model) is proposed to unveil the Fano-type destructive interference mechanisms that lead to the sharp transparency effect. Further, the consequences of the MIT, such as slow-light effect and delay bandwidth products are discussed in the chapter.

In chapter 3, the effects of competing magnetic and electric near field interactions on the sub-radiant (dark) mode are discussed. In the strong inductive coupling regime, the influence of the dark mode is completely annihilated thereby, rendering the split ring resonator (SRR) invisible to the incident THz field. In the process, the passive tuning of MIT is discussed and demonstrated experimentally, where the amplitude of the transparency peak gradually diminishes as the magnetic interactions starts to grow in the system. Some of the consequences of the annihilation of SRR effect such as invisibility of SRR structure and active control of resonant invisibility in the system are demonstrated. The active tuning of the permittivity and permeability of the metamaterial medium is shown using the MEMS MM design.

In Chapter 4, a new technique termed lattice induced transparency (LIT) in inducing the sharp transparency resonances in MM structures is discussed and demonstrated. The concepts on the lattice modes and the physical mechanisms of coupling

the MM resonances with the resonant lattice mode are highlighted in this chapter. A new theoretical framework based on the three-coupled oscillators model is proposed and discussed that elucidates the coupling mechanisms responsible for the observed LIT effects. Further, a strong resonance dispersion and strong enhancement in the group delay of the medium are demonstrated. In the second part of the chapter, active control of the LIT phenomenon is demonstrated, where the coupling between the lattice mode and the MM resonance is dynamically controlled using the ultrafast optical pulse of wavelength 800 nm.

Chapter 5 focuses on the excitation of sharp Fano-type resonances at terahertz frequencies using an out-of-plane reconfigurable MEMS MM possessing two independent voltage controls. First part of the chapter covers the introduction to Fano-type resonances in MMs followed by the motivation and the design of the MEMS based Fano resonance experiment. The active and persistent tuning of sharp Fano resonances are shown that exhibits a hysteretic type of closed loop behavior in its far- and near-field optical characteristics with respect the asymmetry in the structure. We elaborate the discussion focusing on the consequence of the hysteretic type (meta-hysteresis) of behavior that leads to multiple-input-output (MIO) states in the system. Further the implications of MIO states in demonstrating the MM enacted NAND and 'exclusive OR' (XOR) logical operations and its relevance to the secure cryptographic communication are being discussed.

Chapter 6 illustrates the active and ultrafast phototuning of the Fano resonances in metamaterials using various dynamic materials, such as silicon and solution processed semiconducting materials. A simple and economical techniques for realizing active metamaterial are demonstrated by interfacing the metamaterial structures with the dynamic materials such as solution processed perovskites ($CH_3NH_3PbI_3$) and lead iodide ($PbI_2$) thin semiconducting films. This study reveals the low-cost, ultrasensitive and ultrafast modulation of Fano resonances in THz MMs that also possess strong

phonon-metamaterial resonance coupling leading to the hybrid localized plasmon-phonon quasi-particles formations. A two-oscillator (T-O) model is employed to understand the coupling mechanism that reveals the Fano type of interference coupling between the localized plasmon-phonon quasi-particles. These results provide the future prospects on investigating strong resonant plasmon mediated light-matter interactions signifying the the formation of strong and ultrastrong polaritonic formations in semiconductor-metamaterial hybrid systems.

# Chapter 2

# Metamaterial induced transparency in a concentrically arranged unit cell metamolecule

## 2.1 Introduction

### 2.1.1 Classical analogue of electromagnetically induced transparency and slow-light phenomenon

It is a well established fact that the speed of light slows down when the light travels through a medium, and the amount of slowing down is governed by the refractive index ($n$) of the medium. In such processes the information/energy carried by the light will be lost due to the resonant scattering within the medium. Recently discovered new techniques based on the quantum interference phenomenon have given new perspective in slowing down and storing the light pulses inside a strongly dispersive medium with a minimal scattering of the photons at the resonance. These systems enable to store or retrieve the energy/information and also aids in enhancing the light-

matter interactions by orders of magnitude, thereby increasing the nonlinearity of the medium. Such strong dispersive effects can be realized by electromagnetically induced transparency[65] (EIT) technique, where in the influence of the strong pump beam, a thick opaque/resonant medium is rendered transparent to the incoming beam of resonant electromagnetic radiation. This effect was first observed in atomic system[66], where two possible excitation pathways destructively interfere to cancel the absorption effects within the medium. Besides the cancellation of the absorption, the medium shows steep anomalous dispersion within the transmission line-width that greatly slows down the light to several orders of magnitude. So far, the lowest speed for the light pulse (around 17 m/s) has been achieved in an atomic condensate (BEC)[67] using EIT type of interference effects. In such system high density of atomic ensamble with negligeble velocity of atoms in the medium allows the light to slow down to such lowest number. The possibility of achieving the strong resonant dispersion was later proposed in classical systems such as coupled harmonic oscillators/coupled LC circuits[68]. Since MM is an optical analogue of these electrical circuits, EIT type of destructive interference can also be observed in these strongly coupled MM systems. Such effects are termed as Metamaterial Induced Transparency (MIT)[34, 69] or Plasmon Induced Transparency (PIT)[33], where the classical resonators interact strongly with each other to eliminate the absorption effects within the MM unit cell, leading to a sharp transmission peak. There are numerous demonstrations in this line using various types of designs and structural configurations that have allowed to passively tailor the strength of the transparency peak in an adequate manner.

Focus of the current chapter is on designing and characterizing the composite concentric MM system displaying the metamaterial induced transparency at terahertz frequencies, where the MM unit cell consists of concentrically arranged split ring resonator (SRR) and closed ring resonator (CRR) MM structure. The competing electric and magnetic interactions have shown to tailor the amplitude of the

transparency window under the influence of various structural asymmetries. The observed sharp transmission window results in the anomalous variation of dispersive properties of the medium at the resonance. The proposed designs show the slow light effects and also can be applied as amplitude or phase modulators in the broadband communication technologies, filters and power attenuators at terahertz frequencies. In the following sections, the design, principle and optical characterization of the concentric MM structure are discussed. In the later part of the chapter, a theoretical model is proposed to unveil the coupling mechanisms in the structure that reveals the interactions between the radiant (bright, CRR) and subradiant (quasi-dark, SRR) modes and their relative coupling to the free space field. The results discussed in this chapter are published in [70].

## 2.2 Design of the composite concentric MM

In order to study the effect of SRR position and the structural asymmetry on the strength of transparency window, we considered four sets of composite metamolecule structure consisting of concentrically arranged SRR and CRR meta-atoms. In the case of Metamaterial-1 (MM-1), the symmetric SRR resonator is concentrically placed inside the CRR resonator that defines the control sample. Metamaterial-2 (MM-2) is characterized as 'SRR position asymmetry' with SRR position displaced by $a = 4$ $\mu$m towards the upward arm of the CRR. Metamaterial-3 (MM-3) is characterized as 'SRR gap asymmetry', wherein the gap of the SRR is displaced by $b = 5$ $\mu$m. The last set of sample is labeled as Metamaterial-4 (MM-4) possesses both SRR position and gap asymmetry, with the gap in the SRR is displaced by '$b = 5$ $\mu$m' from the center of Y-symmetry axis and the position of the inner SRR ring is displaced upward by '$a = 4$ $\mu$m' from the center of X-symmetry axis. MM samples with various structural asymmetries are graphically displayed in Fig. 2.1.

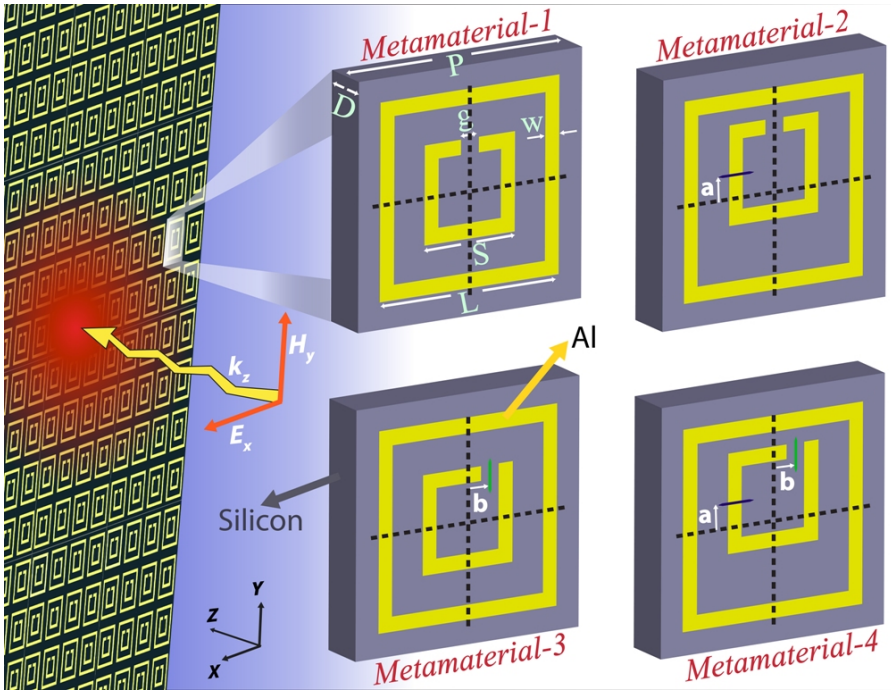


Figure 2.1: An artistic representation of the MM structures and the corresponding unit cell dimensions for the MM-1, MM-2, MM-3 and MM-4 samples are shown. All four MM samples have same material dimensions, defined by length of CRR, $L$ = 40 $\mu$m; length of SRR, $S$ = 20 $\mu$m; SRR gap, $g$ = 4 $\mu$m; resonators width, $w$ = 3 $\mu$m; SRR positional asymmetry, $a$ = 4 $\mu$m and SRR gap asymmetry, $b$ = 5 $\mu$m. The square periodicity ($P$) of the unit cell is 50 $\mu$m with metal thickness ($T$) of 200 nm and substrate thickness ($D$) equal to 640 $\mu$m.

## 2.3 Numerical simulations and discussion

The electromagnetic response through all the designed MMs were first numerically simulated using the CST microwave studio software. In the model, aluminum metal (lossy) was chosen as the resonator and silicon (loss free) was chosen as the substrate. The Frequency domain solver simulation was performed for all modes by defining a unit boundary condition and accurate mesh size. The polarization of the incident THz waves is along the gap-bearing side of the SRR i.e. along X-direction as shown in Figure 2.1 and this allows for the direct excitation of LC mode resonance of the SRR and the dipole resonance of the CRR. Firstly, the transmission response through the individual SRR and CRR resonators are numerically simulated. The transmission

plots are shown in Fig. 2.2, where the SRR (red line) exhibits a relatively sharp resonance of quality ($Q$)-factor equal to 10.6 and the CRR supports the broad dipolar type of resonance possessing $Q$-factor of 1.2 (black line).

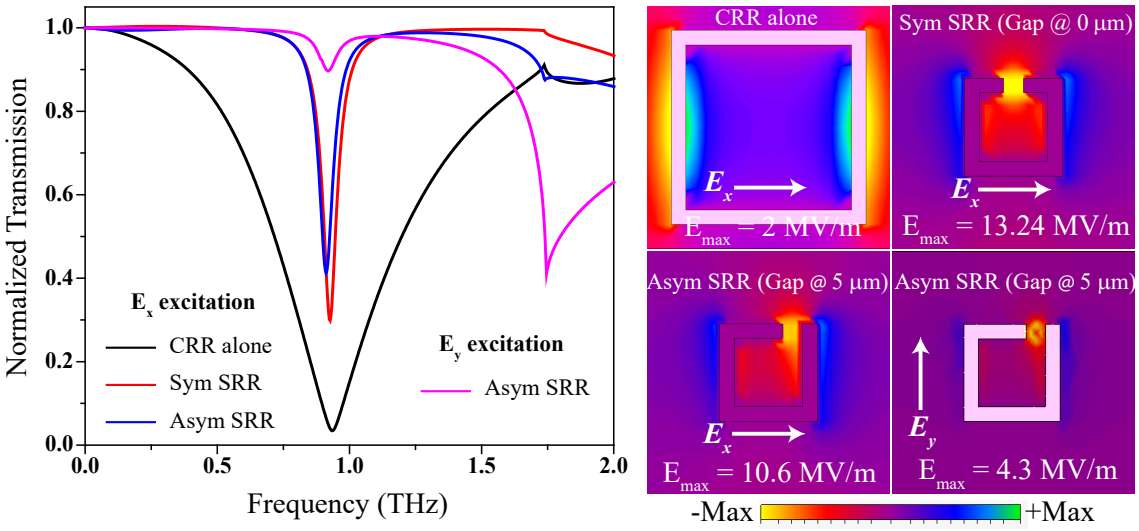


Figure 2.2: Graph displays the individual resonance dips for the outer closed square ring (CRR) alone (black), the inner symmetric SRR ring (red) and the asymmetric SRR ring (blue and magenta for the $E_x$ and $E_y$ excitation, respectively). Electric field strengths for the CRR, symmetric and the asymmetric SRR (gap displaced by 5 $\mu$m) rings are also shown.

The asymmetric SRR structure with gap displaced towards the edge by $b = 5$ $\mu$m possess a weaker LC resonance feature compared to the symmetric SRR structure (blue line). The $Q$-factor of the weakened LC mode for the asymmetric SRR is 11, which is slightly greater than the symmetric resonator. However, its resonance amplitude is lower than the symmetric SRR structure, thereby, possessing the reduced oscillator strength. The strength of the LC resonance excitation in the symmetric and the asymmetric SRR resonators is quantified by the intensity of the electric fields confined in the gap region of SRRs, which is shown in the Fig 2.2. Stronger the electric field confinement, higher the strength of the resonance mode. As shown, the confinement of the electric field in the gap for symmetric SRR is $13.24 \times 10^6$ V/m, which is greater than that for the asymmetric SRR structure ($10.6 \times 10^6$ V/m).

This is because, creating an asymmetry by moving the gap sideward results in a small transfer of electric energy into other polarization mode ($E_y$) dictated by the energy conservation rule. It is quite evident from the figure 2.2 that the asymmetric SRR supports a LC magnetic resonance feature (magenta line) for the perpendicular polarization that assists in confining the electric energy at the gap of SRR resonator.

The highlighting point here is that both the LC and the dipolar resonances for the symmetric/asymmetric SRR and CRR respectively appear at the same resonance frequency but possesses contrasting line widths. This defines the sufficient condition for the excitation of EIT type of transmission resonance when they are coupled with each other in a composite metamolecule consisting of SRR and CRR structures. The LC resonance of the SRR with the higher $Q$-factor behaves as the quasi-dark (subradiant) mode, whereas the dipole resonance of CRR resonator with the lower $Q$-factor behaves as the bright (radiant) mode in the composite system. Hence, in the composite metamolecule, the bright-dark type of interference mechanisms between the CRR and the SRR meta-atoms results in the sharp transmission peak. Unlike other studies on classical EIT effects, in our design and experiments both the resonators are directly excited by the incoming THz wave but with contrasting coupling strengths. The SRR is weakly excited by the incoming wave, whereas, the CRR resonator is strongly excited by the incoming THz wave, which will be quantitatively elaborated in the coupled oscillator analogue disused in the following section 2.7.

The simulated transmission responses through the composite MM samples (MM-1 to 4) are shown in the Fig. 2.3. For the MM-1 sample, as the THz pulse of polarization $E_x$ is incident on the MM, the simultaneous excitation of LC resonance of SRR and dipole resonance in CRR causes strong coupling of SRR and the CRR meta atoms. The interaction between the near-fields of these resonators results in the cancellation of absorption resulting in a sharp transparency peak at the far-field, as show in the Fig. 2.3(a). As the SRR is displaced upwards (MM-2) by a = 4 $\mu$m,

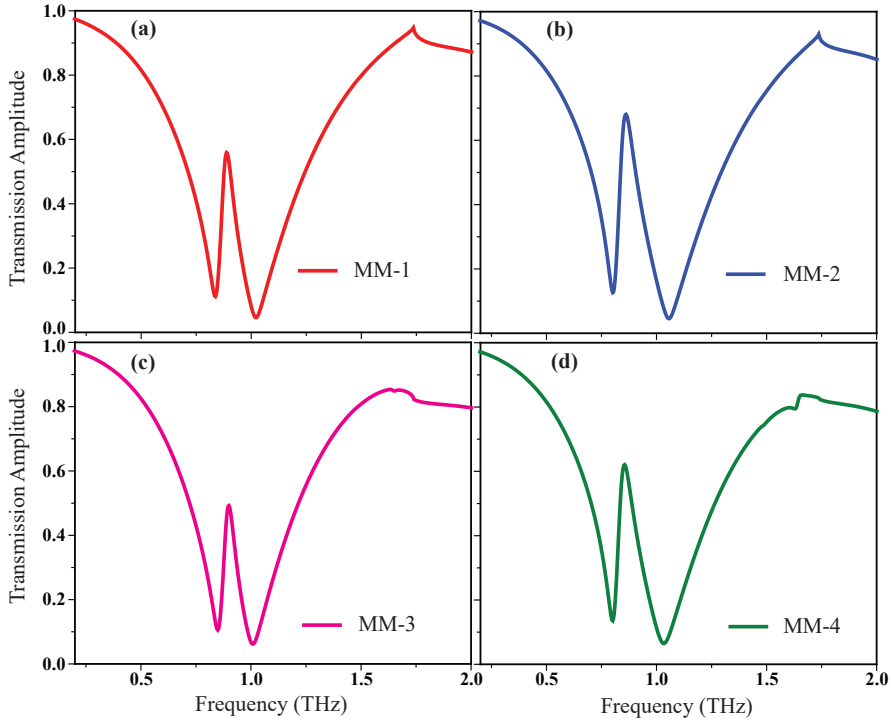


Figure 2.3: Depicts the numerically simulated THz transmission spectra calculated through the MM samples that show a sharp transparency peak (MIT) at each the resonances. Amplitude of the transparency peak vary as MM-2 > MM-4 > MM-1 > MM-3.

an enhancement in the transmission peak is observed (Fig. 2.3(b)). In the case of MM-3 possessing SRR gap asymmetry, the transmission response through the sample shows decreased strength in the induced transparency peak. For the MM-4 sample with both SRR position and gap asymmetry results in a transmission peak possessing the strength that lies in between the transmission strengths for MM-2 and MM-3. In other words, once the SRR position asymmetry is introduced by displacing the gap side of SRR towards the upper arm of CRR that results in the increased strength of the transparency window. Whereas, introducing the SRR gap asymmetry in the composite structure results in the decreased strength of the transparency window. These changes in the far-field characteristics can be clearly explained by the surface currents and the charge distributions in the near-field regime.

## 2.4 Near-field surface currents and electric field distribution

Tailoring of the metamaterial induced transparency peak in the transmission spectrum depicted in Fig. 2.3 are precisely explained using the induced surface currents diagram (Fig. 2.4(a)), obtained from the numerical simulations of electric and magnetic fields at the resonance frequencies. In the case of MM-1 sample, at the frequency of the resonant transparency peak (TP), the SRR resonator that has high confined fields and a dense and strong circular surface current distribution, induces image charges on CRR that run opposite to the direction of SRR surface currents, as shown in Fig. 2.4(a)(TP). These opposing currents induced on SRR and CRR interfere destructively at the resonance frequency to give rise to a sharp transparency peak at the resonance. This destructive interference between the two fields of the classical resonators leads to metamaterial induced transparency (MIT), which is a classical analogue of electromagnetically induced transparency observed in atomic and other classical systems.

Near-field coupling in these classical resonators is explained based on hybridization model of the plasmonic coupling, where the system gives rise to anti-symmetric mode (AM) and symmetric mode (SM) precisely described based on the orientation of the corresponding dipole fields (surface currents). At the transmission dips (AM and SM), surface currents on the SRR and CSR at 0.83 THz and at 1.02THz run anti-parallel and parallel to each other respectively, for the AM and the SM as shown in figure 2.4(a) signifying plasmonic hybridization in the system. Existence of the AM at the lower frequency signifies strong transverse dipole-dipole interaction within the coupled system. This dipole-dipole interaction can be electric as well as magnetic, as their respective dipoles (electric/magnetic) are aligned in the transverse way to the coupling displacement. Electric dipoles are aligned anti-parallel to each other in the

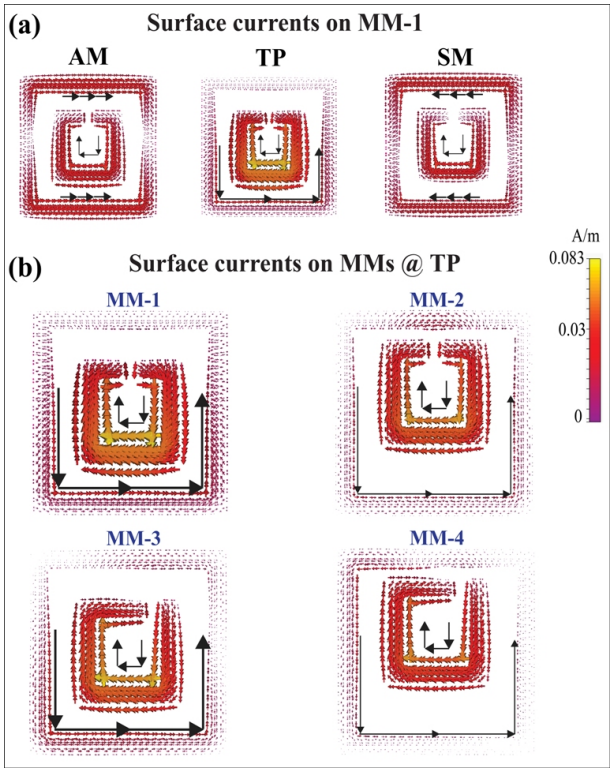


Figure 2.4: (a) Showing the surface current distributions for the anti-symmetric mode (AM), transparency peak (TP) and the symmetric mode (SM) of the composite MM-1 structure. (b) Showing the surface current distributions at the transparency peak (TP) for all the composite MM structures (MM-1-4).

plane of the MM and the induced magnetic dipoles are oriented inward and outward of the MM surface.

On changing the geometry/symmetry of the coupled composite MM, we observed a change in the transmission of the THz pulse. When the gap in the SRR displaced by $b = 5$ $\mu$m (MM-3) will lead to suppression in the amplitude of resulting transparency peak (figure 2.3(c)). This suppression in the transparency peak is solely due to the weakened surface current density and capacitance in the SRR resonance (ref blue curve in figure 2.2(a)), because of its structural asymmetry. As a result, effective strength of the SRR decreases and results in a reduced strength of the transparency peak. This is analogous to the wave interference phenomenon, where decreasing the amplitude of one of the wave, results in the decreased strength of the interference

pattern. The observed enhancement in the transmission peak for the SRR position asymmetry case is due to the increased strength of the electric coupling mediated by the capacitive gap of the SRR, which results in strong destructive interference of the two fields at the transmission peak. As the gap side of the SRR nears to the one of the dipolar arms of CRR, the electric field confined in the gaps strongly influences the CRR structure thereby enhancing the coupling and destructive interference of the induced fields. The increased destructive interference strength in the structures reduces the strength of surface currents within the system, as shown by the surface current distribution in figure 2.4(b) at the transparency peaks.

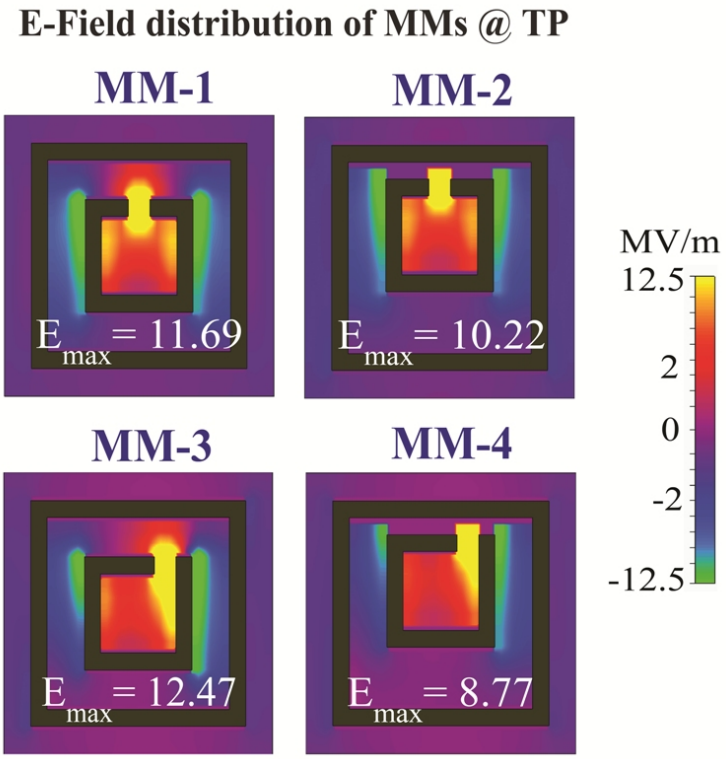


Figure 2.5: Showing the electric field distribution at the transparency peak of the composite MM samples. The strength of the electric field vary as $E_{MM-3} > E_{MM-1} > E_{MM-2} > E_{MM-4}$.

The observed interference mechanisms provide a strong evidence on the coherent nature of the observed transmission curve that can be closely analogue to the coherent EIT effects seen in atomic systems. In figure 2.5, the electric field distributions at

the transparency peak (TP) are provided for all the composite MM samples. By introducing the SRR positional asymmetry (MM-1 to MM-2 and MM-3 to MM-4) results in enhanced transmission peak and reduced confined electric field strengths. Since the confined fields are proportional to the strength of absorption, therefore increasing the transmission reduces the absorption and the confined electric fields at the transmission peak (Fig. 2.5). As the gap asymmetry is imparted in the SRR structures of the composite MM (MM-1 to MM-3), the strength of the electric fields increases (increased absorption) due to the reduced strength in the transparency peak (Fig. 2.3(c)). The MM-4 structure possessing both the gap and structural asymmetry gives the lowest field confinement.

## 2.5 Fabrication and Terahertz characterization

In order to experimentally realize the metamaterial induced transparency effect, the proposed MM designs were fabricated using the conventional photolithography technique described in the chapter 1. 200 nm thick aluminum (Al) metal patterns were fabricated on 640 $\mu$m thick n-type silicon substrate using the photolithography followed by the metal deposition using the thermal evaporation technique and the finally the lift-off process using acetone. The optical microscope (OM) images of the fabricated MM samples are shown in the insets of Fig. 2.6. The unit cell dimensions of the fabricated MM samples are same as the artistic design shown in the figure 2.1.

Optical characterization of fabricated MM samples is carried out using photoconductive antenna based THz-TDS system, described in chapter 1. A sequential terahertz time signal scan is performed through the sample and the bare silicon substrate for the referencing. After post processing, the fast Fourier transformed data of the sample is normalized with the substrate data, which is plotted in the Fig. 2.6 that show good agreement with the simulated results (Fig. 2.3). The MM-

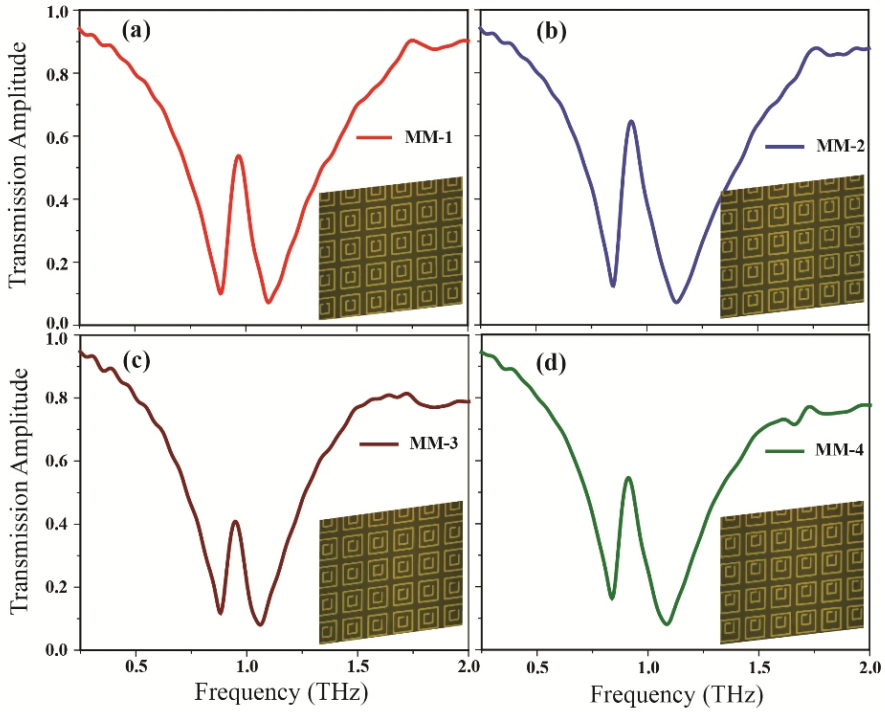


Figure 2.6: (a-d) Experimentally measured THz transmission spectra for the composite MM structures (MM-1 to 4) showing a sharp transparency peak at the resonance. Inset figures are the OM images of the corresponding MM samples.

1 with the concentric SRR and CRR shows the sharp transparency window within a broad dipolar absorption resonance. As predicted by the simulation results the SRR position asymmetry by displacing the SRR resonators upwards by 4 $\mu$m shows increased transmission window, whereas the SRR gap asymmetry with SRR gap moved 5 $\mu$m sidewise displays weaker transmission window. Thereby, by carefully designing the symmetry in the MM unit cell, the metamaterial induced transparency window can be adequately tailored.

Further the transmission response of the composite MM structures to the orthogonal ($E_y$) polarization of the THz beam is shown in Fig. 2.7. For the MM-3 and MM-4 possessing the SRR gap asymmetry, there appears a very weak transmission window, which is due to the interaction of very weak SRR mode of the asymmetric SRR (Fig. 2.2, magenta line) with the dipolar mode of the CRR for the $E_y$ excitation of the

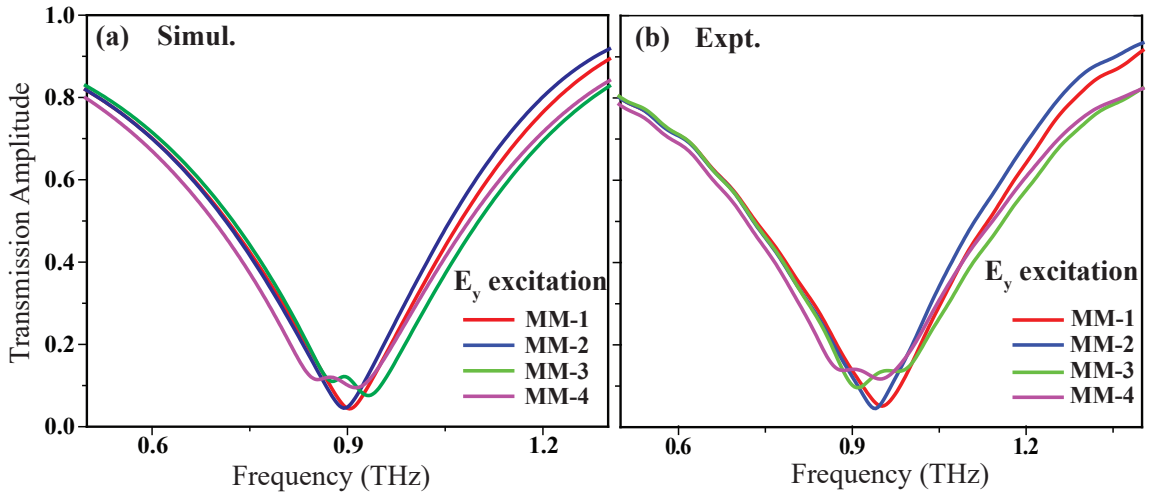


Figure 2.7: Showing the (a) simulated and the (b) measured THz transmission spectra of the MM samples for the $E_y$ polarization of THz beam.

sample. For MM-1 and MM-2 structure with shifted SRR position, strong dipolar types of resonances are observed at the resonance frequencies.

## 2.6 Tailoring the slow light effect in the composite MMs

The phenomenon of interference effects leading to metamaterial induced transparency (MIT) results in the anomalous change in the dispersion within the material along the propagation direction. A steep gradient in the dispersion (change in the refractive index/phase with wavelength/frequency) within the medium results in the delay in the group velocity of the incident pulse and thereby, exhibiting the slow light phenomenon. In metamaterials, the slow light effect is characterized by the group delay values $t_g$, determined by the derivative of phase ($\phi$) of the transmitted field with respect to angular frequency ($\omega$), given by,

$$t_g(\omega) = -\frac{d\phi}{d\omega} \tag{2.1}$$

The group delay value signifies the time delay of the pulse in the medium compared to its propagation time in vacuum. The stronger the dispersion in the medium results in higher delay time that depends on the slope of phase change in the medium around the resonance of the transparency peak. The group delays for the pulse propagating through the sample extracted for the simulated and the measured transmission data are shown in Fig 2.8(a) and (b), respectively. The simulated and the measured values show good correspondence with each other, with the group delay reaching as high as 5 ps and 3 ps, respectively for the symmetric MM-1 sample at the transmission resonance. The group delay for the proposed MM structures decrease with the asymmetry in the structure, where the MM-4 possessing SRR position asymmetry (MM-2 and MM-4) shows the lower group delay numbers compared to the MM-1 and MM-3 structures having the highest group delay numbers (Table. 2.1). The observed small deviations in the measured and the simulated group delay values are predominantly due to the real material losses in the experimentally fabricated samples, which result in broader dispersion within the medium. From the expression 2.1, we see that the group delay numbers are proportional to the slope of the dispersion (or phase change, as shown in insets of Fig. 2.8(a) and (b)) within the medium. Hence, broader dispersion results in the reduced magnitude of the group delay and steeper dispersion enhances the group delay of the pulse within the medium. In the simulations these material losses are not accounted for and hence it gives steeper dispersion within the propagation length through the medium. The other factors causing these deviations are the possible fabrication errors and the measurement uncertainties involved with respect to the limited scan length of the THz pulse in the THz-TDS measurements that could directly affect the value of $d\omega$.

Further, in order to enhance the relevance of the proposed slow-light based MM structures in the communication networks, the delay bandwidth products are calculated, which quantifies the capacity the device in the communication channel to

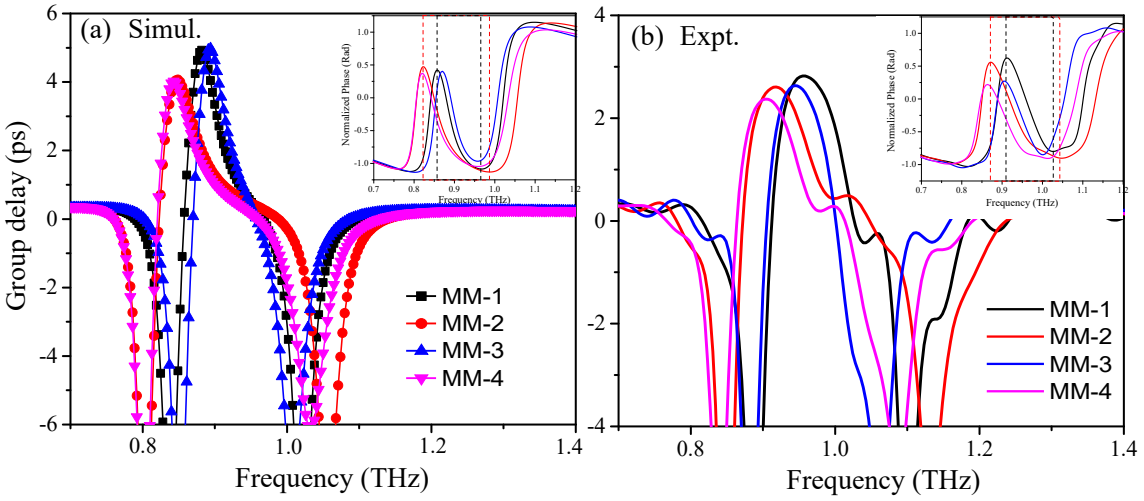


Figure 2.8: Simulated and experimentally measured (a and b) group delay ($t_g$). The inset diagrams show the change in the phase of the propagating THz light within the transparency window, which results in a steep dispersion through the medium.

transmit and receive the information. In other words, it represents the volume of bits/data that can be transferred before the first bit reaches the receiver. Larger the DBP, larger the number of bits in the transmission channel and will ensure the efficient transmission control protocol (TCP) networks. Table 2.1 presents experimentally measured values for group delay ($t_g$), delay band-width product (DBP) at the transparency peak and the respective $Q$-factors for all the four composite MM samples. Delay bandwidth product (DBP) is defined as the product of the frequency bandwidth ($\Delta f$) and the time delay ($t_g$) of the transmitted pulse (DBP $= \Delta f \times t_g$). From the data shown in Table 2.1, we see that as coupling strength increases, DBP increases and the corresponding $Q$-factor decreases and vice versa. For example, MM-2 that displays stronger mode coupling compared to all other samples possesses maximum DBP and minimum $Q$-factor. The proposed planar MM samples offer largest DBP at the lower terahertz frequencies[71], indicating increased buffering capability for the high bit-rate broadband telecommunication networks.

| MM Samples | $t_g$ (ps) | DBP | $Q$-factors |
|---|---|---|---|
| MM-1 | 2.78 | 0.21 | 11.74 |
| MM-1 | 2.52 | 0.217 | 9.83 |
| MM-3 | 2.63 | 0.174 | 13.35 |
| MM-4 | 2.34 | 0.18 | 11 |

Table 2.1: Calculated group delay, DBP and $Q$-factor values for the experimentally measured transmission curves shown in figure 2.8

## 2.7 Two-Coupled Oscillator model

The observed metamaterial induced transparency is a result of interference phenomenon between the near-fields of the CRR (termed as bright resonator) and the SRR (termed as quasi-dark resonator) and is theoretically analogued to the classical system of two coupled oscillators[68, 72–74]. The two-coupled classical oscillators system, where each particle is attached by a spring to the wall and another spring connecting two particles together has been used to understand the interference mechanisms behind the electromagnetically induced transparency and Fano type of interactions in the optical systems. The solutions of the coupled oscillators have been commonly used for theoretically fitting the numerical and the experimental spectra of the optical and atomic systems.

The schematic of the two-coupled oscillators system is shown in Fig. 2.9, where the two resonators, bright and quasi-dark are respectively treated as damped oscillators modes (particles) of mass $m_b$ and $m_d$ driven by an incident electromagnetic wave $\mathbf{E}(t) = E_0 e^{-i\omega t}$. Each of the particles masses $m_b$ and $m_d$ are attached to the wall by springs of spring constant $k_b$ and $k_d$, respectively and both the particles are coupled to each other by a spring of spring constant $K$. Strength of their interaction with the incoming field $\mathbf{E}(t)$ depends on the $\frac{charge}{mass}$ ratio of resonators. The particle with mass $m_b$ is termed as the 'bright' mode ($x_b$) that couples to the electric field of the incoming light radiation determined by the '$q_b E_0/m_b$' (Eqn. 2.2), whereas the

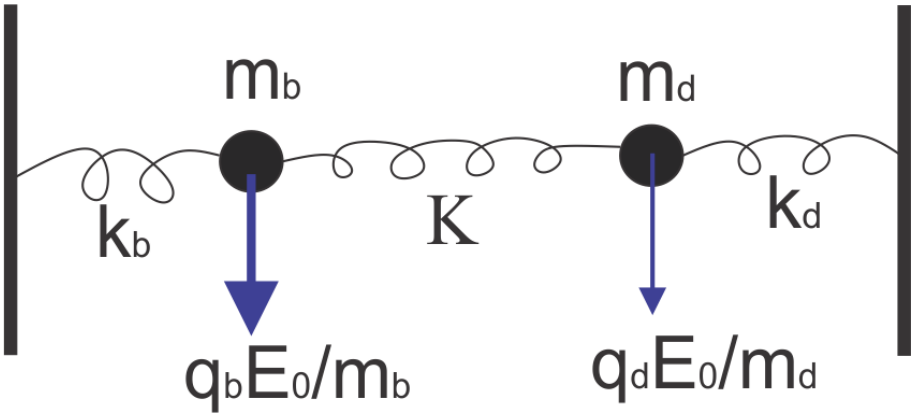


Figure 2.9: The coupled oscillator model that is proposed to fit the observed experimental results is schematically presented. $m_b$ and $m_d$ are the masses of the bright and quasi-dark resonators, respectively. $k_b$ and $k_d$ are individual coupling constants of the bright and the quasi-dark resonators. $K$ represents the coupling constant between the bright and the dark resonators. The bright resonator is driven by the external field of strength $q_bE_0/m_b$, whereas the quasi-dark mode is coupled to the external field by strength $q_dE_0/m_d$.

other resonator mode of mass $m_d$, is weakly coupled to the incident electric field with strength '$q_dE_0/m_d$' and hence is termed as 'quasi-dark' mode ($x_d$) as given by Eqn 2.3.

The equations of motion for the two-coupled oscillators system are given by,

$$\ddot{x}_b(t) + \gamma_b\dot{x}_b + \omega_b^2 x_b(t) + \Omega^2 x_d(t) = \frac{q_b E}{m_b} \tag{2.2}$$

$$\ddot{x}_d(t) + \gamma_d\dot{x}_d + \omega_d^2 x_d(t) + \Omega^2 x_b(t) = \frac{q_d E}{m_d} \tag{2.3}$$

Here, $\omega_b = \sqrt{k_b/m_b}$ , $\omega_d = \sqrt{k_d/m_d}$ and $\gamma_b$, $\gamma_d$ are the resonance angular frequencies and the loss-factors of the bright and quasi-dark particles respectively. $\Omega = \sqrt{K/M}$ (where $M$ is the effective mass), defines the coupling strength between the bright and the quasi-dark particles. Solutions for $x_b$ and $x_d$ obtained by expressing $q_d = \frac{q_b}{A}$ and $m_d = \frac{m_b}{B}$ are given by,

$$x_b = \frac{((B/A)\Omega^2 + (\omega^2 - \omega_d^2 + i\omega\gamma_d))(QE/M)}{\Omega^4 - (\omega^2 - \omega_b^2 + i\omega\gamma_b)(\omega^2 - \omega_d^2 + i\omega\gamma_d)} \tag{2.4}$$

and

$$x_d = \frac{(\Omega^2 + (B/A)(\omega^2 - \omega_b^2 + i\omega\gamma_b))(QE/M)}{\Omega^4 - (\omega^2 - \omega_b^2 + i\omega\gamma_b)(\omega^2 - \omega_d^2 + i\omega\gamma_d)}. \tag{2.5}$$

Where, $A$ and $B$ are numerical constants that define the relative coupling of bright and quasi-dark modes to the incoming electric field $\mathbf{E}$(t). From these displacement amplitudes the polarization and the susceptibility relations can be derived using the following relations.

$$\chi = \frac{P}{\epsilon_0 E} = \frac{Qx_b + q_d x_d}{\epsilon_0 E}. \tag{2.6}$$

Therefore,

$$\chi = \chi_R + i\chi_I$$

$$= \frac{K}{A^2 B}\left(\frac{A(B+1)\Omega^2 + A^2(\omega^2 - \omega_d^2) + B(\omega^2 - \omega_b^2)}{\Omega^4 - (\omega^2 - \omega_b^2 + i\omega\gamma_b)(\omega^2 - \omega_d^2 + i\omega\gamma_d)}\right. \tag{2.7}$$
$$\left. + i\omega\frac{A^2\gamma_d + B\gamma_b}{\Omega^4 - (\omega^2 - \omega_b^2 + i\omega\gamma_b)(\omega^2 - \omega_d^2 + i\omega\gamma_d)}\right)$$

Here, Re[$\chi$] represents the dispersion and Im[$\chi$] gives the absorption (loss) within the medium. We perform a curve fit using the 1-Im[$\chi$] expression to the experimental data shown in figure 2.10 (colored magenta), which represents the transmission response through a medium. We observe from the fit that our model shows an excellent agreement with the observed results for the following fitting parameters, $A = 40$ and $K_0 = 4 \times 10^{25}$. The remaining parameters are treated as constants and are extracted from the experimental curves itself. The decay constants are $\gamma_d = 5 \times 10^{11}$ rad/s ,$\gamma_b = 3 \times 10^{12}$ rad/s , and the coupling strength for the system is determined from the corresponding experimental curves by using the formula, $\Omega = \sqrt{\frac{\omega_+^2 - \omega_-^2}{2}}$ , where $\omega_+$ and $\omega_-$ are the higher and lower stop band frequencies of the spectrum (symmetric and the anti-symmetric modes of plasmonic hybridization in figure 2.10(c)). The resonance frequencies $\omega_d$ and $\omega_b$ are determined using the following conditions. At

the transparency peak ($\omega = \omega_T$), Re[$\chi$] goes to zero. By applying this condition to Eqn. 2.7, we get,

$$A(B+1)\Omega^2 + A^2(\omega_T^2 - \omega_d^2) + B(\omega_T^2 - \omega_b^2) \tag{2.8}$$

On further simplification, we arrive at the following expression of the dark mode resonance frequency,

$$\omega_d^2 = \frac{A(B+1)\Omega^2 + (A^2+B^2)\omega_T^2 - B\omega_b^2}{A^2} \tag{2.9}$$

For a very large $A$, the expression 2.9 reduces to $\omega_d \approx \omega_T$ , is the frequency of the transmission peak in the observed spectra (transparency peak in figure 2.10(c)). Similarly, at the stop band frequencies ($\omega_+$ and $\omega_-$), where the absorption ideally goes to infinity, we have Im[$\chi$] = $\infty$. Using this condition $\omega_b$ can be determined by equating the denominator of Im[$\chi$] to zero, which gives, $\omega_{b\pm} = \sqrt{\omega_\pm \mp \frac{\Omega^4}{\Omega_\pm^2}}$ . By substituting the calculated values for $\omega_b$, $\omega_d$, $\gamma_b$, $\gamma_d$ and $\Omega$ and by putting $B = 2$ (i.e. mass of SRR is half the mass of CSR) we obtain a closest fit of theoretical model to the experimental data, as shown in the Fig. 2.10(c) - (f).

Therefore, derived susceptibility expression (Eqn. 2.7) provides the best possible information on interaction of the system possessing bright and quasi-dark mode, particularly the type of system studied in this work. This expression helps in estimating the relative coupling strengths of bright mode and quasi-dark mode to the incident electric field, both in coupled and uncoupled system. By obtaining the values of constants $A$ and $B$ from the fit, we can calculate the $\frac{charge}{mass}$ ratio, which determine the coupling strength of the individual resonator with the incident electric field. Knowing the individual coupling of the resonators to the incident radiation is of major importance in the study of coupling in the system and in defining the nature of the resonator. We observed that the coupling of quasi dark state to the incoming

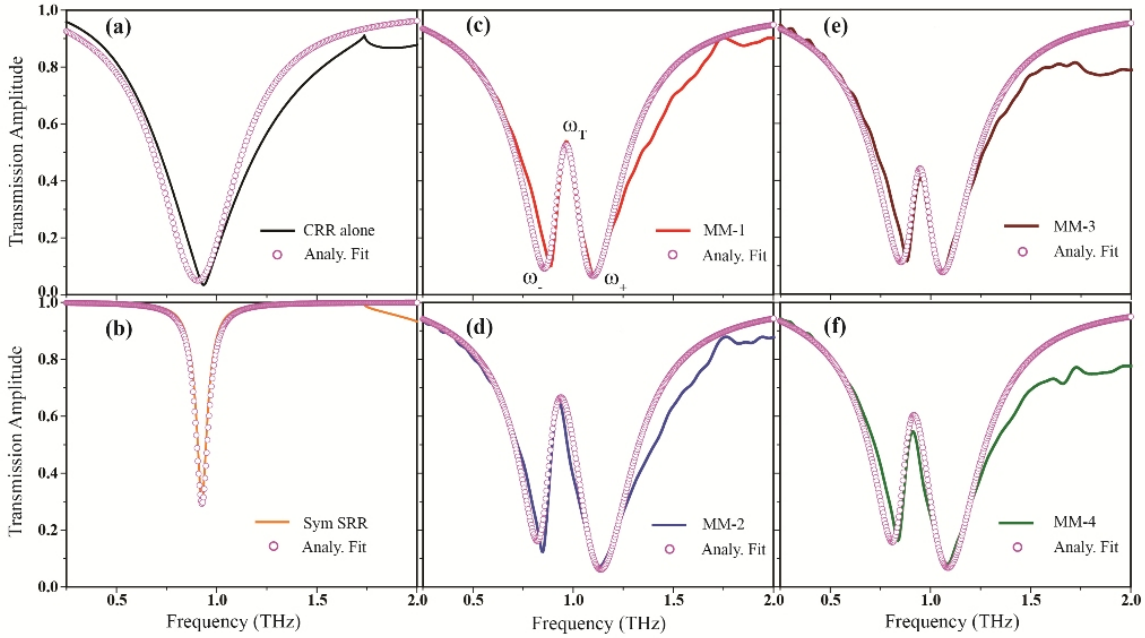


Figure 2.10: (a) and (b) are the dipole and the LC resonance of CRR and SRR resonators with the fitted analytical data. (c)-(f) The analytically fitted measured transmission spectra for the MM-1 to MM-4, respectively.

field in the coupled structure diminishes by 20 times due to the influence of the bright mode resonator. In the uncoupled case, the relative coupling of the CRR and the SRR with the incoming field is quantitatively given by Eqns. 2.1 and **??** for $\Omega = 0$, respectively. From the analytic fit (Fig. 2.10 (a) and (b)), the estimated coupling strength of CRR to the incoming radiation ($E_x$) is "twice stronger than the coupling strength of the SRR. Thus, the strongly coupled CRR with broad dipolar resonance (lower $Q$-factor) behaves as a "bright mode", where as the weakly coupled SRR with sharp LC resonance (higher $Q$-factor) is termed as "quasi-dark mode".

The proposed model was also examined by comparing the variation of $Q$-factors with the change in the coupling strength ($\Omega$). The $Q$-factors are calculated using the formula $Q = f_0/\Delta f$, where $f_0$ is the resonance frequency of the curve and $\Delta f$ is the line width of the curve. The line width $\Delta f$ is extracted using a standard Lorentzian fit to the transmission curves using the Lorentzian formula, $y = y_0 + \frac{2A}{\pi}\frac{\Delta f}{4(x-x_c)^2+(\Delta f)^2}$ , using the Origin software, where '$\Delta f$' is the line width (FWHM) of

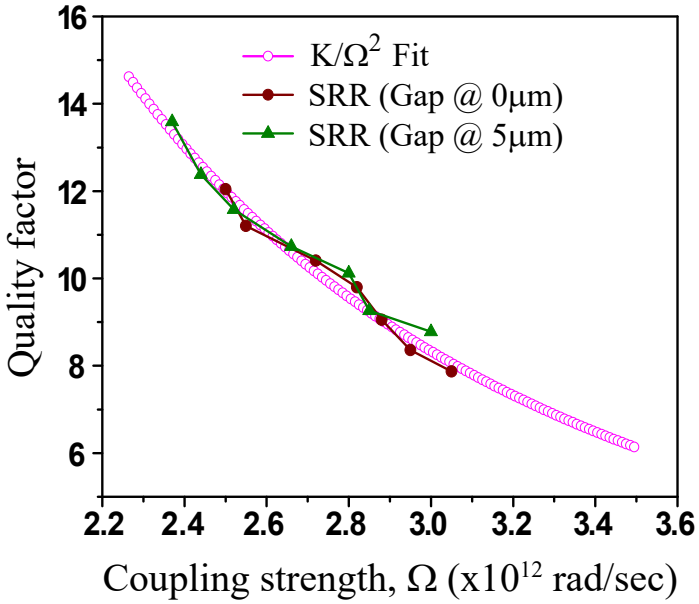


Figure 2.11: The variation in the quality ($Q$)-factors of the transparency peak extracted from the numerically calculated spectrum is fitted with the analytical model ($K/\Omega^2$).

the resonance. We find that the $Q$-factors obtained from the simulated transmission curves for the samples with different SRR positions (SRR position asymmetry) follow $K/\Omega^2$ variation (Fig. 2.11), as predicted by the coupled oscillator model.

## 2.8 Conclusions

In this chapter, we showed the near-field interference effects on the transmission properties of planar MM structures under two type asymmetries in the system. By introducing the SRR gap asymmetry, the amplitude of the transmission window decreases due to the reduced strength in the interference effect. On the other hand, as the SRR gap side is moved towards the bright mode (CRR arm), the electric coupling within the system is enhanced and thus the transmission. The effect of interplay between the strengths of electric and magnetic dipoles on the transmission will provide deeper insights into the classical analogy of the quantum interference effect. The

quantitative analysis using the two coupled-oscillators model gives useful insights on the interference mechanisms occurring in the system, which has shown an excellent agreement with the observed results. The proposed model also gives the relative coupling of the bright (CRR) and the quasi-dark (SRR) mode to the incoming THz wave in the uncoupled and the coupled system. The proposed asymmetric planar MM systems with varying transmission characteristics will allow us to precisely control the group velocity and group index of the pulse within the medium and with the increased DBP. These devices promise potential applications in broadband telecommunication technologies as modulators, filters and slow-light devices terahertz frequencies.

# Chapter 3

# Resonant invisibility of Split Ring Resonator (SRR) at terahertz frequencies

## 3.1 Introduction

The prospects of MMs have given remarkable benefits in controlling and manipulating the effective parameters such as permittivity ($\epsilon_{eff}$) and permeability ($\mu_{eff}$) of the medium. Such control has provided excellent possibility of tailoring and elucidating unique and unnatural phenomena by precisely tuning the structural and geometrical parameters of the MM. The realization of perfect lens[23, 24, 57], negative refraction[75, 76], invisibility cloaking[77–80], and many more intriguing phenomena has been the hallmark of MMs. Particularly, in the THz part of the EM spectrum, metamaterials have provided huge implications by showing many interesting results that include artificial magnetism[26, 81], memory[82], active tuning[54, 58], ultrafast modulators[83, 84], slow-light devices[33, 45] and many more. The strong magnetic response of the metamaterials at THz frequencies have shown bi-anisotropy mediated

interactions in the split ring resonator (SRR) system that enhances both electric as well as magnetic interactions at THz frequencies. Such bi-anisotropy feature of the SRR structures have enabled new type of bright-dark interactions mediated by the inductive coupling in the system, resulting in the excitation of sharp transparency[85], Fano[32] and toroidal resonances[86] at THz frequencies.

In this chapter, we discuss and demonstrate a resonant invisibility phenomenon for a split ring resonator (SRR) in a composite MM structure. In general, the concept of invisibility means reducing or cancelling the scattering effects from the material of interest. In other words, a realistic object can be made hidden from interacting to the incident field under the favorable conditions. This can be achieved by several ways, for instance, transformation optics[77, 78], scattering cancellation techniques (SCTs)[87–90], transmission line techniques[91] and so forth. In our study, the observed invisibility of the SRR is different from the widely observed cloaking phenomena, as in our system only one of the structure (i.e. SRR) is made invisible to the incoming resonant field. The mechanisms for the SRR invisibility effect are compelled by the resonant bright (strong-scatterer) and the quasi-dark (weak-scatterer) interactions in the metamaterial induced transparency medium (discussed in chapter 2). The MM design consists of a closed ring resonator (CRR) covering the SRR, where under the strong magnetic field interactions between the CRR and the SRR, hides the latter structure from interacting to the incoming TE ($E_x$) polarized THz wave. Due to the strong bi-anisotropy in the SRR excitation, the interactions in the structure are dominated by both electric (near to SRR gap) and magnetic interactions (in the vicinity of the curved arm of the SRR structure). This interplay of interactions between the SRR and CRR results in the magnetic annihilation of inductive-capacitive (LC) resonance of the SRR structure in the strong inductive coupling regime, thereby making the SRR non-interacting to the incident resonant THz field. Here, SRR is termed as weak-scatterer with smaller resonance line-width,

whereas, the CRR with broad resonance is termed as strong-scatterer. In the strong inductive coupling regime, the opposing magnetic dipoles induced within the strong scatterer (in our case, CRR) cancel out the scattering effects in weak scatterer (in our case, SRR), thereby rendering the SRR invisible to the resonant THz beam. In the proceeding sections, the design, near-field coupling mechanisms, the magnetic annihilation of SRR effect leading to its invisibility and the active control of the SRR invisibility using the MEMS MM design are discussed and demonstrated. Here, it is important to note that, in the regular cloaking mechanisms such as SCTs[87–91], both the scatterers are made invisible under the cancellation of out-off phase dipoles. However, in our design, the CRR (strong-scatterer covering the SRR) remains visible to the incoming beam, where only SRR structure (the material of interest) is made invisible to the resonant light field, thereby separating this effect from the conventional cloaking techniques.

## 3.2 Design and Fabrication

The composite MM design that consists of an outer CRR structure surrounding the SRR structure is shown in Fig. 3.1 (a). To study the SRR invisibility effect and the tuning of transparency peak, we designed various samples possessing same unit cell dimensions but varying coupling distances $d$ = 7, 5, 3 and 1 $\mu$m, as shown by the optical microscope images of the fabricated samples in Fig. 3.1 (b-e). The resonator structures are made of 200 nm thin aluminum (Al) metal that is fabricated on a high resistivity silicon substrate of thickness 500 $\mu$m. Since the resolution of conventional photolithography process for fabricating the MM structures is limited to $> 2$ $\mu$m, a different fabrication method is used to prepare the samples. A laser based scanning lithography technique is used to obtain the required resolution of $d = 1$ $\mu$m between the SRR and CRR resonators. The AZ1518 photoresist mask was written on a 500 $\mu$m

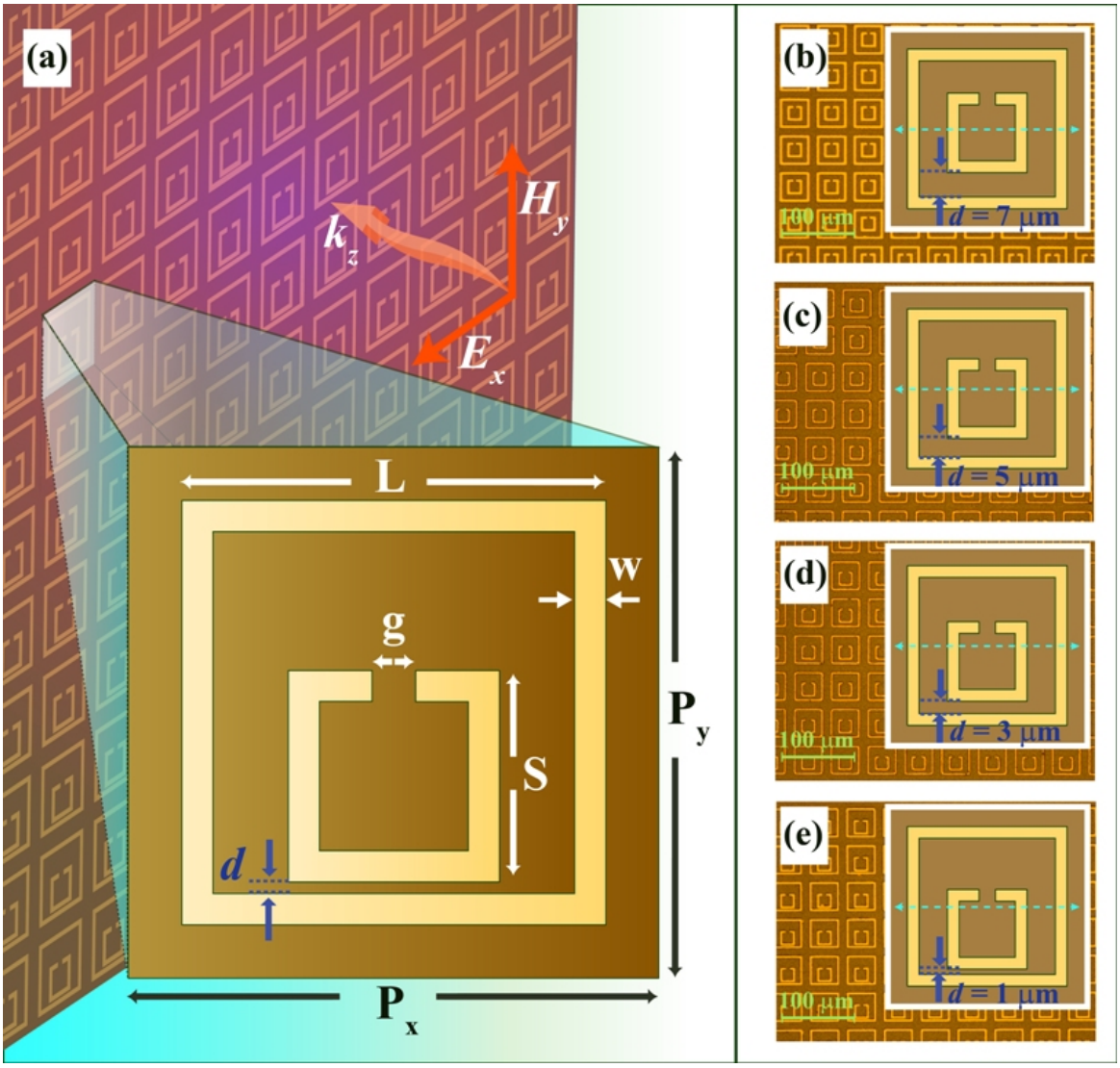


Figure 3.1: (a) Graphical representation of the composite MM structure depicting the unit cell geometry and dimensions. The unit cell dimensions are, length of CRR, L = 40$\mu$m; length of SRR, S = 20 $\mu$m; width, w = 3$\mu$m; SRR gap, g = 4 $\mu$m and the square periodicity, $p_x = p_y = 50$ $mu$m. (b-e) The optical microscope (OM) images with the corresponding unit cell depicting the coupling distances ($d$) from the SRR inductive and the CRR dipole arm.

thick silicon substrate ($\rho > 5000$ Ω-cm) using a 405 nm laser followed by development and thermal evaporation of 200 nm thick aluminium metal. Finally, the desired MM patterns were achieved by performing lift-off process using acetone. The optical microscope images of the fabricated samples are shown in Fig. 3.1(b-e)

## 3.3 Cancellation of metamaterial induced transparency effect in the strong inductive coupling regime

For the incident THz wave of polarization $E_x$, the SRR resonator supports the LC type of magnetic resonance and the CRR being a square symmetric structure supports the broad dipolar resonance. The structural parameters of the SRR and the CRR are chosen in such a way that both the LC and the dipole modes resonate at the same resonance frequency but possess contrasting line widths (scattering rates). The SRR structure displaying a LC resonance with sharper line width (weak scatterer) is termed as the 'quasi-dark mode', where the CRR structure with broad (strong scatterer) dipolar resonance is termed as the 'bright mode'. The presented concentric alignment of the SRR (quasi-dark mode) and the CRR (bright mode) resonators manifests the metamaterial induced transparency effect, which has been discussed in the previous chapter 2.

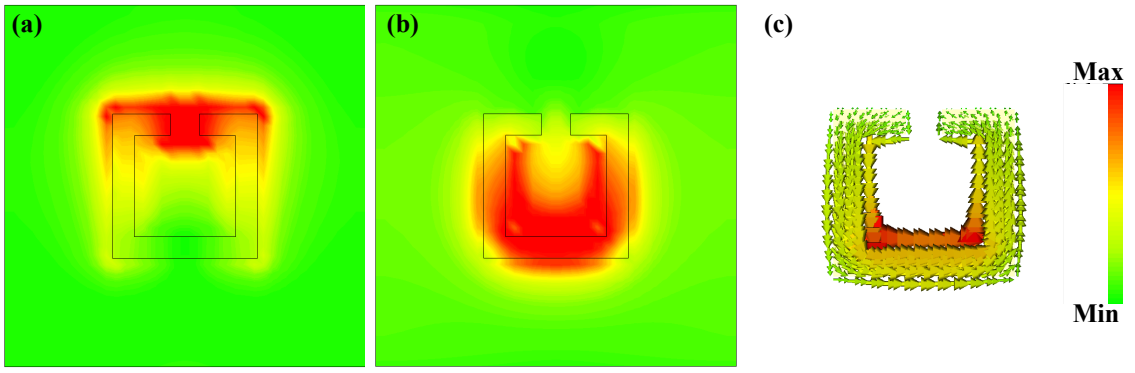


Figure 3.2: Showing the (a) electric (b) magnetic and (c) surface current distributions of the SRR resonator structure illuminated with a THz wave of polarization parallel to gap bearing arm of the SRR. Existence of both Electric and magnetic energy highlights the bi-anisotropy of the SRR structure at THz frequencies.

Numerical simulations were performed using the CST MWS software to study the effect of near field interactions on the transparency peak as the coupling distance

($d$) between the SRR and the CRR is decreased from 7 $\mu$m to 1 $\mu$m and also in the individual SRR and CRR structures. The SRR structure has proven to exhibit both electric as well as magnetic response (bi-anisotropy) in the terahertz part of the electromagnetic spectrum. It is well established that the capacitive gap in the SRR structure signifies the electric confinement of the fields that favors the strong electric coupling between the adjacent resonators (see Fig. 3.2 (a)). On the other hand, the currents flowing through the inductive arm of the SRR resonator give rise to the effective magnetic response with the magnetic dipoles oriented perpendicular to the MM resonator plane (Fig. 3.2 (b-c)). Hence, the near field coupling between the SRR gap and the adjacent resonator is mediated by the strong electric coupling, whereas, the interaction between the SRR resonator arm and the nearby resonator is mainly dominated by the magnetic fields. In the previous chapter 2, we discussed that when the gap side of SRR is near to the CRR arm, the electric field mediated interactions are induced by the SRR gap that results in the enhancement of the transparency peak. Here, when the arm side of the SRR is displaced downwards (near to the lower CRR arm), the inductive coupling between the SRR arm and the CRR arm dominates that results in the decreased amplitude of the transparency window, as shown by Fig. 3.3. Thus the concentric arrangement of the SRR and CRR meta-atoms provides flexibility to thoroughly investigate the competition between the electric and the magnetic near field interactions in enhancing and destroying the transparency effect in the strong coupling regimes.

For the simulation, aluminium metal with the dc conductivity ($\sigma_{dc} = 3.56 \times 10^7$ S/m) is used as the metallic resonators and the silicon ($\epsilon_r = 11.7$) is considered as the transparent substrate at terahertz frequencies. The unit cell boundary conditions are used in the frequency domain solver that uses FDTD method to solve the Maxwell's grid equations to give out the required S-parameters. Fig. 3.3 (a), shows the numerically calculated THz transmission spectrum through the samples with $d$ = 7, 5, 3

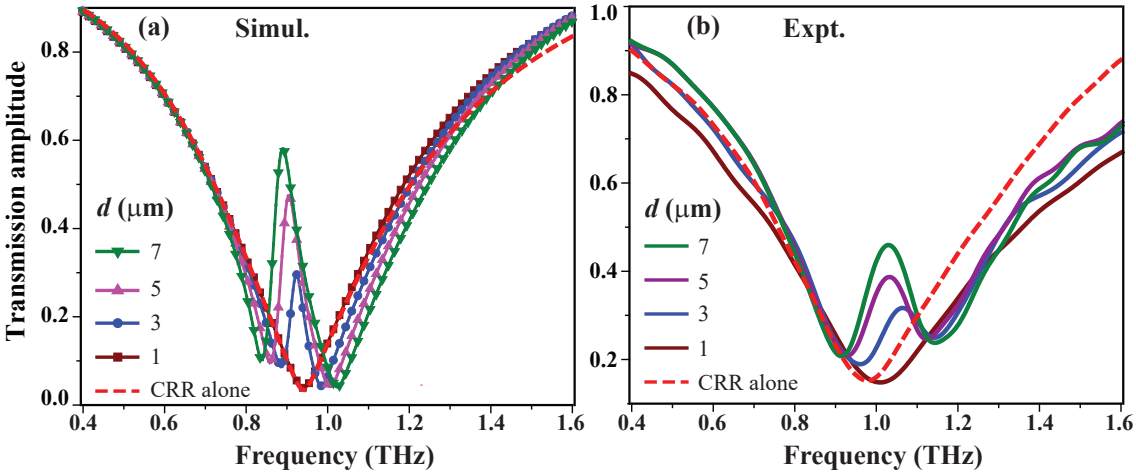


Figure 3.3: (a) Numerically simulated and (b) experimentally measured THz transmission spectra for the composite MM structure with varying coupling distance ($d$) and for the CRR ring alone.

and 1 $\mu$m, which shows gradual decrease in the amplitude of the transparency peak that eventually disappears for the sample with $d = 1$ $\mu$m. Experimentally measured transmission spectrum is displayed in Fig 3.3(b) that shows very good agreement with the simulated data for the corresponding samples with $d = 7$, 5, 3 and 1 $\mu$m, where the complete annihilation of the transparency effect is seen for the sample with $d = 1$ $\mu$m.

## 3.4 Magnetic annihilation of LC Resonance feature in SRR

The most striking feature of the transmission response for the sample with $d = 1$ $\mu$m is that the far-field resonance of the sample shows the broad dipolar type of spectrum that exactly overlaps with the dipolar resonance feature of the CRR alone. This overlapping of the resonances of the composite MM structure ($d = 1$ $\mu$m) and the only CRR structure signifies the complete cancellation in the contribution of SRR resonance effect on the near field interactions in the composite MM structure. In

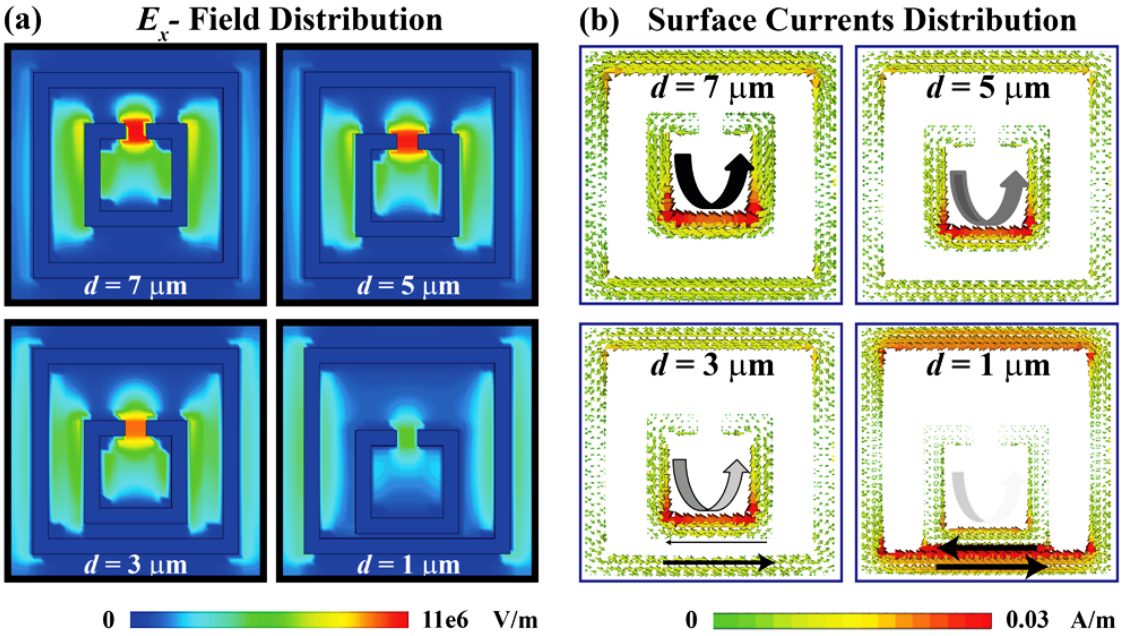


Figure 3.4: Numerically simulated (a) electric field and (b) surface current distributions of the composite MM structure with decreasing coupling distance ($d$) showing the gradual disappearance of the SRR effect in the system.

other words, the SRR resonator that is structurally resonant to the incoming THz field becomes transparent/invisible in the presence of outer CRR structure. The experimental results also show the complete annihilation of transparency effect for the sample at $d = 1$ $\mu$m that shows almost overlapping with the measured dipolar resonance through the CRR alone. However, the observed mismatch in the line widths of resonances of the composite MM structure ($d = 1$ $\mu$m) and the only CRR MM structure in our experimental data can be mainly attributed to the structural irregularities in the fabricated samples, which can have small impact on the strength of the near field interactions in the MM structures. The gradual reduction in the amplitude of the transmission resonance with decreased $d$ in the composite MM structure essentially signifies the weakening of the quasi-dark mode (SRR) resonance, which is more evident from the electric field and the surface current distributions shown in Fig. 3.4 (a) and (b), respectively.

The electric field distribution plot shown in the Fig. 3.4 (a) provides a clear visual

indication of the annihilation of SRR effect that shows a gradual diminishing of electric field confinement in the SRR resonator gap with the decrease in $d$. For instance, at $d$ = 1 $\mu$m, the electric field density in the SRR gap region shows significant reduction, whereas the field across the CRR dipolar arms show larger gain compared to the MM structure with $d = 7$ $\mu$m. This indicates that the composite structure gradually attains the dipolar characteristics as the SRR arm comes in close proximity of the CRR arm. The nature of surface current distributions given in Fig. 3.4 (b) for the composite structure with $d = 7$ $\mu$m the high current density of SRR influences the adjacent CRR resonator and induces opposing surface currents on the CRR arms that destructively interferes with the surface currents of the SRR structure. This destructive interference results in a sharp transparency peak with an anomalous dispersion in the system. As the coupling distance $d$ is decreased, the surface current density of the SRR is gradually reduced and at the same time the current density on the dipole arms of the CRR grows higher. As the inductive arm of the SRR gets closer to the dipole arm of CRR, strong opposing currents develop on the edge of the SRR arm and the CRR arm. These opposing currents gradually grow up in strength with respect to decreased coupling distance and interferes with the fields of the SRR. This interference of the opposing magnetic dipoles will be destructive, thus cancelling the currents induced on the SRR (weak scatterer) making it invisible/non-interacting to the incident resonant TE ($E_x$) polarized THz beam.

## 3.5 Magnetic field ratio $\frac{Hz_2}{Hz_1}$: $Hz_2$ phase reversal point

We further articulate the near-field magnetic interactions responsible for the annihilation of the SRR resonance (invisibility of the SRR resonator) in the form of change in the ratio of magnetic fields ($\frac{Hz_2}{Hz_1}$) in the metamolecule, where $Hz_2$ is the z-component

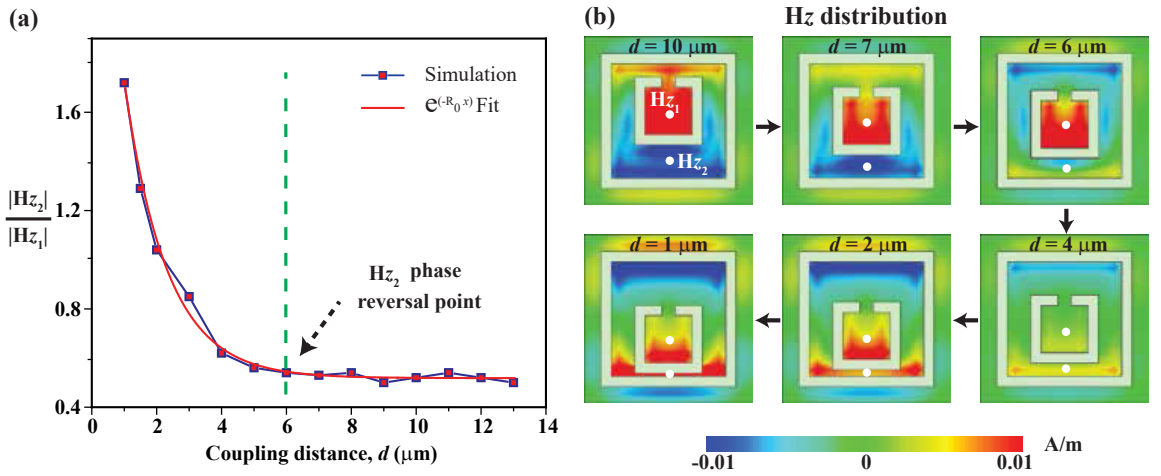


Figure 3.5: Depicts the varying strengths in the competing magnetic fields $Hz_1$ and $Hz_2$ with respect to the coupling distance ($d$). The vertical green dotted line signifies the transition point of the phase of $Hz_2$, where at the regime of inductive coupling ($d \leq 6$ $\mu$m), strength of $\frac{Hz_2}{Hz_1}$ grows exponentially. The solid red curve represents the exponential fit to the simulated data. (b) Simulated $Hz$ distribution showing gradual phase reversal in the $Hz_2$ component near to $d = 6$ $\mu$m, indicating the influence of the strong magnetic interaction (inductive coupling regime) on the SRR excitation. The white dots represents the positions where the magnetic field values are calculated.

of the magnetic field in between the SRR arm and the CRR resonator and $Hz_1$ is the magnetic field within the SRR structure (Fig. 3.5). The magnetic field ratio $\frac{Hz_2}{Hz_1}$ signifies the relative strength of the magnetic fields within and outside the SRR resonator, wherein $\frac{Hz_2}{Hz_1} > 1$ implies the cancellation of magnetic resonance of SRR in the composite system. The $z$-component of the magnetic field represents the strength of the SRR resonator that constitutes the magnetic dipoles oscillating perpendicular to the plane of the sample. Hence it becomes realistic to compare the effect of coupling distance on the strength of the $Hz$ components of the magnetic fields to investigate the strength of the SRR in the composite structure.

From the magnetic field simulations we observe that, as the arm side of the SRR resonator is displaced towards the CRR arm, the strength of the magnetic coupling between them shows a steep increase below the coupling distance $d = 6\mu$m. Magnetic field inside the SRR structure ($Hz_1$) stays higher than the field ($H_{z2}$) between the

SRR and CRR resonator arms (i.e $\frac{Hz_2}{Hz_1} < 1$) for the coupling distances ($d$) greater than 2 $\mu$m, indicating the presence of the SRR effect in the system. As $d < 2$ $\mu$m, the magnetic field $Hz_2$ becomes monotonically larger than the $Hz_1$ (i.e. $Hz_2 > Hz_1$) and hence the field within the SRR resonator is completely suppressed. This condition of $\frac{Hz_2}{Hz_1} > 1$, results in the cancellation of the SRR effect in the composite MM structure at $d = 1$ $\mu$m. In figure 3.5 (b) the spatial distribution of the magnetic near-field ($Hz$) in the composite structure is shown, where the magnetic fields inside the SRR ($Hz_1$) and between the SRR-CRR arms ($Hz_2$) show gradual variation in their intensity and phase as the coupling distance ($d$) is gradually decreased.

As the coupling distance ($d$) decreases, the field inside the SRR structure gradually diminishes and becomes extremely weak after the phase reversal point of $Hz_2$ ($d = 6$ $\mu$m). The phase reversal point is defined as the coupling distance ($d$), where the phase of the $Hz_2$ flips its sign and aligns with the phase of the $Hz_1$. This phase reversal condition signifies the switch from the effective capacitive coupling in the composite medium to the effective inductive type of near-field coupling. As the symmetry along $x$-axis is broken by displacing the SRR downwards, the interaction of the electric field at the SRR gap with the top CRR arm reduces and at the same time the inductive effects due to the SRR arm begin to dominate the coupling effects in the composite system. Below the $Hz_2$ phase reversal point ($d \leq 6$ $\mu$m), where the magnetic interactions dominate, the field between the CRR and the SRR arm gradually grows in strength ($Hz_2 > Hz_1$) to eliminate the SRR resonator effect near $d = 1$ $\mu$m. This indicates the strong magnetic or inductive coupling regime of the composite MM structure. Resulting strong $Hz_2$ magnetic fields between the CRR and SRR cancel the opposing weak magnetic fields ($Hz_1$) generated within the SRR, thereby annihilating its influence in the composite structure. At higher coupling distances ($d >$ 6 $\mu$m), strength of $Hz_1$ is almost twice of $Hz_2$ indicating the strong excitation of SRR structure (weak magnetic coupling regime/strong capacitive coupling regime). Thus,

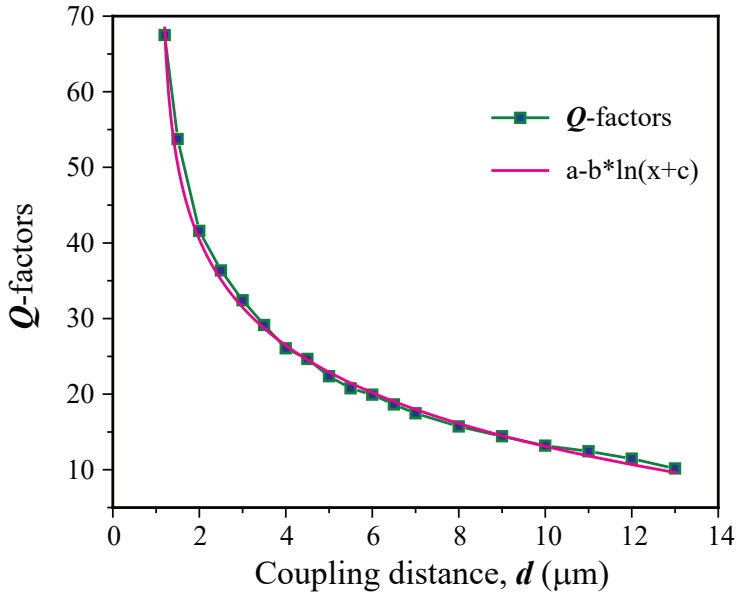


Figure 3.6: Graph depicting the $Q$-factors of the transmission peak with respect to coupling distance ($d$). Variation in $Q$-factors follows the logarithmic behavior indicating the influence of both strong electric and magnetic coupling in the system.

the interplay between the magnetic fields $Hz_1$ and $Hz_2$ in the composite concentric resonator system is majorly responsible for the cancellation of the SRR effect and its invisibility to the incoming THz wave in the strong magnetic coupling regime.

## 3.6 Effects of interplaying electric and magnetic interactions on the $Q$-factor of transmission resonance

As discussed in the previous sections, the competing magnetic and the electric interactions in the proposed composite MM structure with varying coupling distance ($d$) results in the amplitude tuning of classical EIT transmission resonance peak. This shows a direct consequence on tuning the quality ($Q$) - factor of the transmission resonances with respect to the change in the coupling distance ($d$). The $Q$-factor

of the resonance is defined as $Q = \frac{f_0}{\Delta f}$, where $f_0$ is the resonance frequency of the transmission peak and $\Delta f$ is the full width at half maximum (FWHM) of the transmission intensity peak obtained from fitting the simulated curves using the Lorentzian peak function defined by, $y = \frac{2A}{\pi}\frac{\Delta f}{4(x-x_c)^2+(\Delta f)^2}$, where $A$ is the area under the curve. From the extractions, $Q$-factor of the transmission resonance is the highest for smaller coupling distance ($d$), which is in the range of 70 for $d = 1.2$ $\mu$m and it decreases logarithmically with increase in the coupling distance, as shown in Figure 3.6. The logarithmic decay of the $Q$-factors signifies the delayed saturation in the near field interactions within the structure that deviates from the normally observed exponential decay of the $Q$ factors in various kind of resonance features in MMs[92, 32, 93]. Since the SRR exists within the dipolar ring (CRR), the system stays in the influence of either strong electric/weak magnetic (capacitive coupling) or strong magnetic/weak electric (inductive) coupling regime. Hence, the presence of both the electric and magnetic fields causes the slow decay in the $Q$-factor following the logarithmic behaviour.

## 3.7 Active control of resonant invisibility of SRR using MEMS MM

### 3.7.1 Introduction

The MM designs exhibiting the resonance SRR invisibility effect discussed in the previous sections are the passive designs, where each sample with different coupling distance ($d$) are fabricated separately. Such limitation of the passive designs that requires fabricating multiple devices to show tunable functionalities will curb the prospects of the MMs to be used as real time tunable devices to the real-world applications. In this hindsight, a great progress has been made in the form of

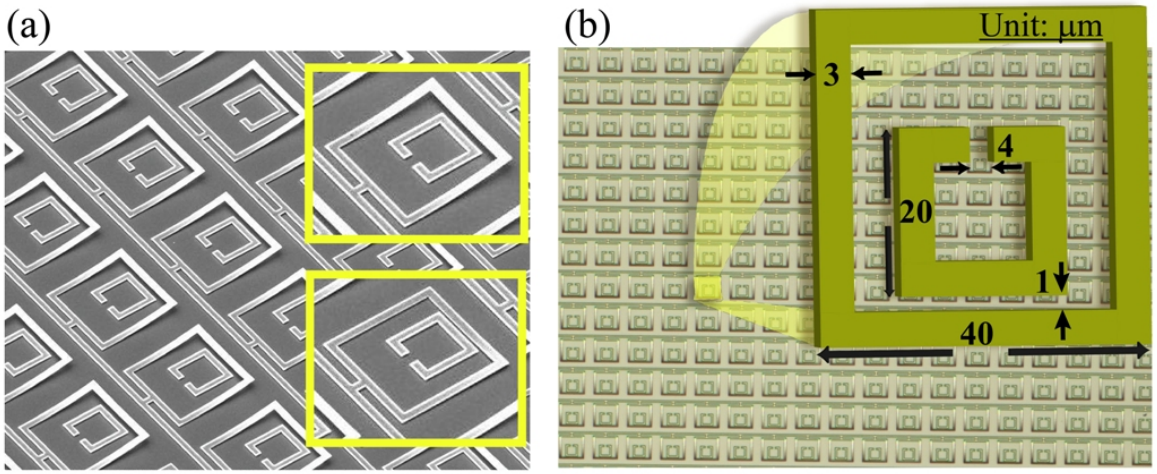


Figure 3.7: (a) Scanning electron microscope (SEM) image of the MEMS incorporated composite reconfigurable MM structure consisting of outer MEMS closed ring resonator (CRR) and the inner split ring resonator (SRR), where the latter becomes invisible to the incoming THz wave in the ON ($V_{DC}$ = 30 V) state of the device. Insets show the SEM image of OFF ($V_{DC}$ = 0 V) and ON ($V_{DC}$ = 30 V) state of the device. (b) The Optical microscope image in the OFF state of the device showing the unit cell dimensions of the MM design with a square period of 50 $\mu$m

tunable and reconfigurable metadevices[94, 95], where their structural and optical properties can be controlled and tailored actively by using the external stimuli such as electrical signals[96, 60, 61], temperature[58, 97], optical pulse[62, 54] and many more. Here, in the view of expanding the functionalities of the earlier discussed passive control of resonant invisibility effect of SRR, we propose and demonstrate an active and reconfigurable design that is composed of MEMS actuated closed ring resonator (CRR) cantilever that is actively reconfigurable using voltage control and a split ring resonator (SRR) structure placed non-concentrically within the CRR.

### 3.7.2 Design and Fabrication

The proposed 2-D and actively tunable resonant invisibility device is composed of a SRR placed nonconcentrically within a MEMS actuated CRR. The scanning electron microscope (SEM) image of the fabricated sample is shown in the left inset of the Fig. 3.7(a), where in the inset both released and snapped down states of outer CRR

are presented. The unit cell dimensions of the sample are given in the right inset of Fig. 3.7 (b), where the total length of SRR is half that of the MEMS actuated CRR, with their metal arms separated by a distance of 1 $\mu$m when the device is in ON state. The device is fabricated using the complementary metal-oxide-semiconductor (CMOS) compatible process (process in detailed in chapter 1.4. The MM is made of varying thicknesses of Al ($T$ = 900 nm) on top of 50 nm aluminum oxide ($Al_2O_3$) deposited on the lightly doped silicon substrate. The selective part of CRR is released by isotropically etching away the sacrificial $SiO_2$ layer from underneath the bimorph structure. Due to the residual stress in the bimorph layers, the microcantilevers are bent up (released state), thereby creating an air gap between the substrate and bimorph cantilevers, as shown by the SEM image of the sample in the inset of Fig. 3.7 (a). The out-of-plane actuation of the released arm of the CRR structure is achieved through electrostatic control, by applying voltage ($V_{DC}$) across the Al metal lines and silicon substrate. The $Al_2O_3$ layer in the bimorph ($Al_2O_3$/Al) structure electrically isolates the metal interconnect lines and the Al layer of CRR cantilevers from the substrate when the device is in its ON state. These electrically isolated interconnects allow for the voltage controlled out-of-plane actuation of the CRR microcantilever.

### 3.7.3 Active control of SRR invisibility effect

The active tuning of the invisibility effect of SRR is shown in the form of presence and absence of metamaterial induced transparency effect in the far field spectrum of composite structure. The THz light polarized parallel ($E_x$) to the gap bearing arm of the SRR resonator is incident in a normal angle on to the sample. The measured THz far-field transmission spectra for the ON and OFF voltage states of the device are given in Fig. 3.8(a) along with the corresponding SEM image of the device configuration. As shown, in the OFF (released, $V_{DC}$ = 0 V) state of the CRR microcantilevers of the device, the transmission spectra exhibit a strong coupling

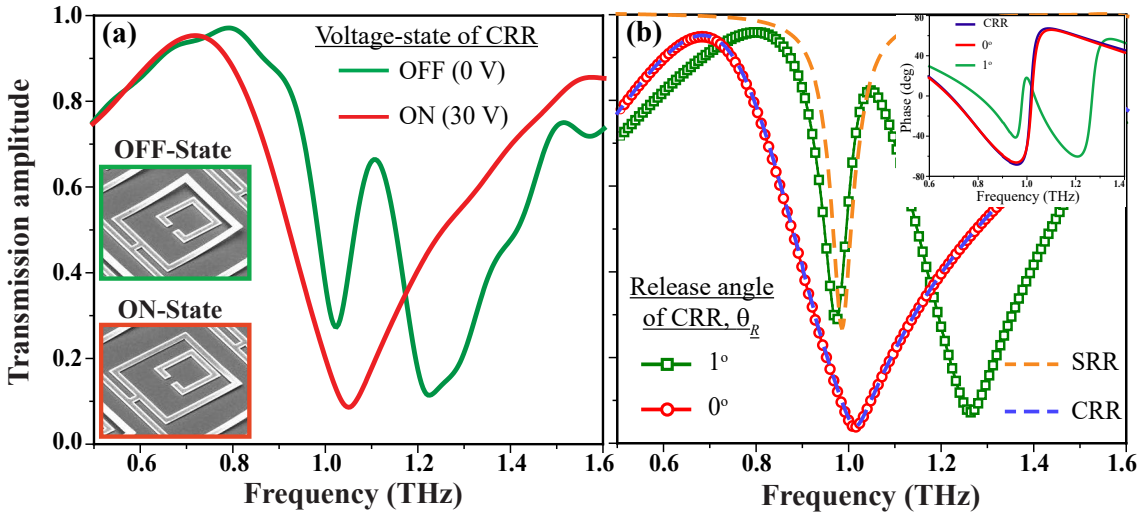


Figure 3.8: (a) Experimentally measured THz transmission spectra of the composite MEMS MM without (green line) and with (red line) the voltage ($V_{DC}$) applied across the metal lines and the silicon substrate. The measurements are performed on the sample with the metal thickness $T = 900$ nm. The insets show the OFF and ON states of the MEMS MM with $V_{DC} = 0$ V and 30 V, respectively. (b) Depicts the numerically simulated THz transmission spectra for the composite MEMS MM and the individual CRR and SRR resonators. The spectrum for the release angle of CRR ($\theta_R$) of 1° and 0° respectively correspond to the OFF and ON states of the experimentally measured data shown in (a). The inset represents the phase spectra of the transmitted THz light for CRR alone and ON/OFF state of the composite MEMS MM device.

behaviour signifying the mode hybridization of the SRR and the CRR resonances leading into a transmission peak at 1.1 THz. This configuration represents the widely studied MM induced transparency effects, leading to a sharp transmission window at the resonance frequency (discussed in the previous sections 2). The appearance of transparency peak in the spectrum signifies a strong influence of the eigen (LC) resonance of the SRR in the composite MEMS MM structure. As the CRR microcantilever is snapped down (ON state, $V_{DC} = 30$ V) on the substrate, the transparency peak completely disappears and a strong dipole type of resonance is observed in the transmission spectrum (red line). It is important to highlight that, in the ON configuration of the device, the coupling distance between the SRR and the CRR is $d = 1$ $\mu$m, which is same as the structure discussed in section 3.2.

The numerical simulations were performed using the CST microwave studio frequency domain solver (discussed in Chapter 1.3) to study the near- and far-field optical characteristics of the MM structure for the ON (snapped) and OFF (released) states of the CRR microcantilevers. The numerically obtained transmission spectra are shown in Fig. 3.8(b). The voltage states ($V_{DC}$) in the experiments can be expressed in terms of released angle ($\theta_R$) of the CRR microcantilever, where $V_{DC}$ = 0 V (OFF) and 30 V (ON) corresponds to $\theta_R = 1^\circ$ (released) and $0^\circ$ (snapped), respectively. The curves shown in green squares and the red circles represent the OFF (1$\circ$) and the ON ($0^\circ$) states of the CRR microcantilever are in good agreement with the corresponding measured spectra shown in Fig 3.8(a). Further, simulations were carried out for the uncoupled (individual) SRR and the CRR structures possessing the same unit cell dimensions and periodicity as specified in Fig. 3.7(b) and the resulting transmission spectra are shown by orange-dash and blue-dashed lines, respectively in Fig. 3.8(b). Particularly, the LC resonance feature of SRR coincide with the low frequency hybridized mode of the composite MEMS MM structure in the OFF state ($\theta_R = 1^\circ$) of CRR, whereas in the ON state ($\theta_R = 0^\circ$), the dipole resonance of CRR alone precisely overlaps with the observed broad dipole type feature in the composite MEMS MM structure. Further, the phase of the propagating wave passing through the composite MEMS MM for ON ($\theta_R = 0^\circ$) state shows no distortion with respect to the phase of the field passing through the CRR alone, as shown in the inset of Fig. 3.8(b). On the other hand, for the OFF state ($\theta_R = 1^\circ$) of composite MEMS MM device, due to the influence of SRR scatterings, the phase profile of the propagating light wave (green line) is strongly altered, thus modifying the wave front of the transmitting wave. This confirms that the SRR present in the composite MEMS MM in the ON state of the device does not alter the phase or wave front of the propagating beam, thereby remains invisible to the incoming THz wave.

The nature of confined electric, magnetic fields and the surface current distribu-

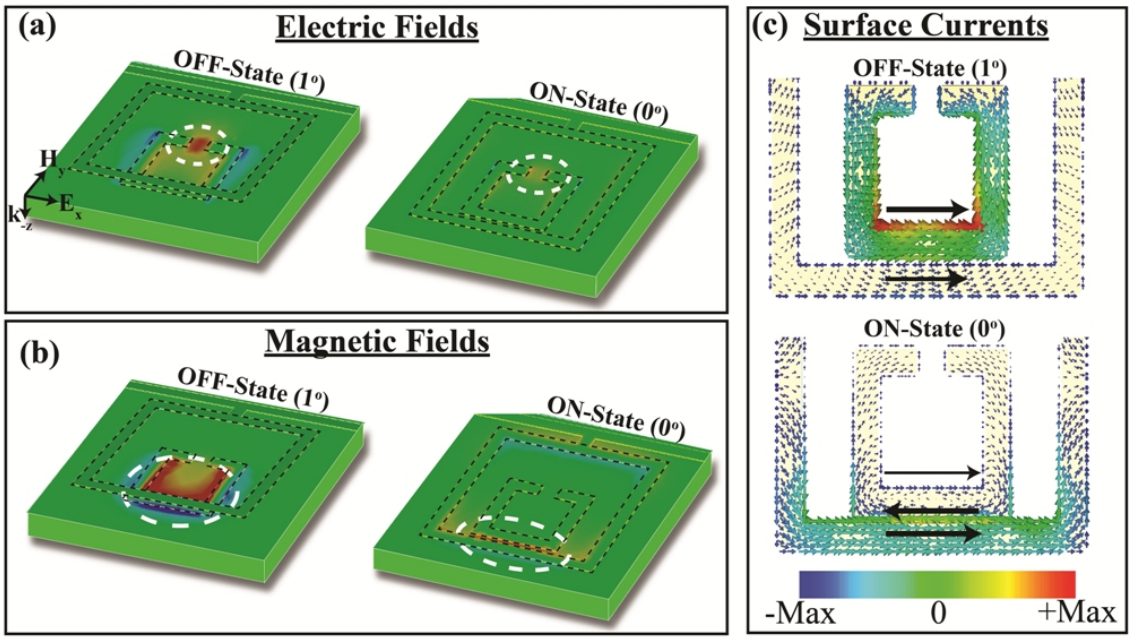


Figure 3.9: Numerically simulated (a) Electric field, (b) magnetic field and (c) surface current distributions shown for the OFF and ON state of the MEMS MM highlighting the cancellation of SRR fields in the ON state.

tions shown in Fig. 3.9(a)-(c) clearly highlights the change in the influence of SRR effect in the composite MEMS MM device, as the device is switched from OFF to ON state of the CRR microcantilevers. In the OFF (released) state, the electric and magnetic fields are confined in the gap and around the metal arm of the SRR structure, respectively, indicating a strong resonant interaction of the SRR resonator with the incoming THz wave of polarization $E_x$. This represents the weak coupling regime of the composite system. As the CRR is snapped down onto the substrate (ON-state), with the separation between the SRR inductive arm and CRR arm being $d = 1$ $\mu$m, the confined electric and magnetic fields within the SRR structure disappears, thereby making the resonant SRR structure invisible to the incident $E_x$ polarized THz light.

As highlighted in the previous sections 3.4, the mechanism of the observed resonant invisibility is understood by studying the surface current distributions, which are shown in the Fig. 3.9(c). In the OFF state, SRR shows a strong surface current distribution, signifying a stronger coupling of SRR with the incident THz wave,

where most of the near-field energy is confined within the SRR structure. In the ON state, once the inductive arm of the SRR is in a close proximity (1 $\mu$m) of the CRR arm, strong opposing currents develop on the outer edge of the SRR and the CRR arms. These currents induce magnetic fields of opposite phases between the SRR and CRR arms with their magnetic dipoles aligned perpendicular ($H_z$) to the plane of the sample. The induced surface current (magnetic dipole) possesses the opposite sign and greater strength with respect to the intrinsic surface currents (magnetic field) of the SRR structure, thereby cancelling the surface currents (near-field effects) of the SRR structure. Further insights on magnetic interactions in the composite MM structure and their coupling mechanisms are discussed in detail in the previous section 3.4. Hence, the strong resonant interaction between the opposing magnetic dipoles of SRR (weak scatterer) and the CRR (strong scatterer) results in the cancellation of SRR magnetic dipoles thereby making the SRR structure invisible to the incoming resonant and $E_x$ polarized THz light.

### 3.7.4 Tailoring the permittivity and permeability of the composite MEMS MM medium

The major factors governing and responsible for the invisibility effects are the effective parameters of the medium such as electric permittivity ($\epsilon$) and magnetic permeability ($\mu$). Here, the complex permittivity ($\epsilon = \epsilon_{Re} + i\epsilon_{Im}$) and permeability ($\mu = \mu_{Re} + i\mu_{Im}$) of the composite MEMS MM structure are extracted for varying $\theta_R$ of CRR. The effective parameters of the medium were calculated using the expression[21, 98] for the impedance ($Z$) and the refractive index ($n$) by using the scattering (S) parameters $S_{11}$ (reflected) and $S_{21}$ (transmitted) extracted from the numerical simulations. Later, the complex electric permittivity and complex magnetic permeability were calculated by using the formulae $\epsilon = \frac{n}{Z}$ and $\mu = n \cdot Z$, respectively and the $\epsilon_{Re}$ and $\mu_{Re}$ are plotted in

Fig. 3.10 along with the transmission response for varying $\theta_R$ of CRR microcantilever. At larger angle (i.e. $\theta_R = 50°$), the electric permittivity ($\epsilon$) in the medium dominates the resonance response (orange line in Fig. 3.10(b)), whereas the strength of magnetic permeability ($\mu$) becomes insignificant and the $\mu_{Re}$ takes the positive values (orange line in Fig. 3.10(c)) signifying electric response in the system. This observation is true since, at the larger angles (weak coupling regime) SRR resonance shows the dominating effects, where the resonant interactions are dominated by the electric response of the SRR showing the negative values and anomalous change in the $\epsilon_{Re}$.

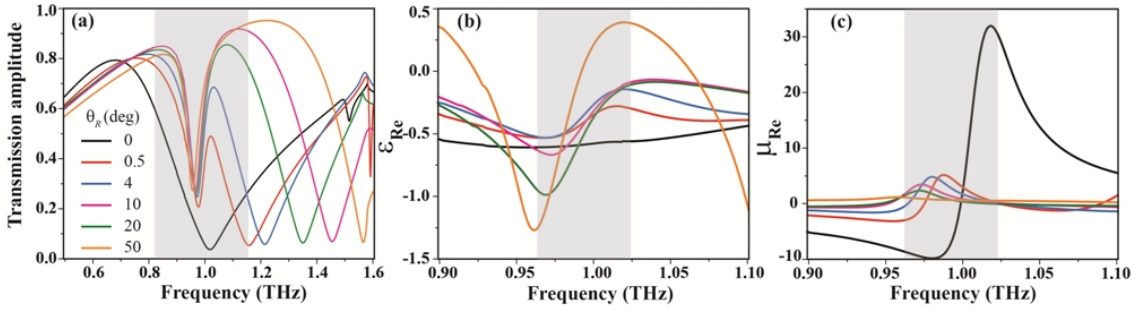


Figure 3.10: Numerically simulated (a) transmission spectra (b) Real permittivity ($\epsilon_{Re}$) and (c) Real permeability ($\mu_{Re}$) plots for varying release angles ($\theta_R$) of the CRR cantilever showing the switch between purely electric medium (in the OFF state, $\theta_R = 50°$) to completely magnetic medium (in the invisible state, $\theta_R = 0°$) of the MEMS MM medium.

As the release angle ($\theta_R$) is decreased, the $\epsilon$ of the medium gradually decreases, meanwhile the magnetic response ($\mu$) of the medium starts to grow stronger in strength. For $\theta_R = 0°$, the broad resonance spectrum near 1 THz exhibits strong magnetic response with anomalous change in the magnetic permeability of the medium (black line in Fig. 3.10(c) ), whereas the electric permittivity shows no response (black line in Fig. 3.10(b)). This result justifies that the broad resonance feature in the composite MEMS MM medium shows rich magnetic response due to the strong magnetic interactions between the inductive arm of the SRR and the CRR arm in the ON state ($\theta_R = 0°$, SRR invisible state) of the device. Hence, in this configuration (i.e. $\theta_R = 0°$), the composite device behaves as the magnetic medium showing the

negative values for $\mu_{Re}$ near the resonance as shown in Fig. 3.10(c). Therefore, by actively tuning the release angles ($\theta_R$) of the CRR microcantilever using the voltage input enables the gradual switching between the electric and magnetic response of the composite MEMS MM medium, thereby aiding the dynamic control over the invisibility of SRR in the system.

### 3.7.5 Influence of THz incidence angle on the SRR Invisibility

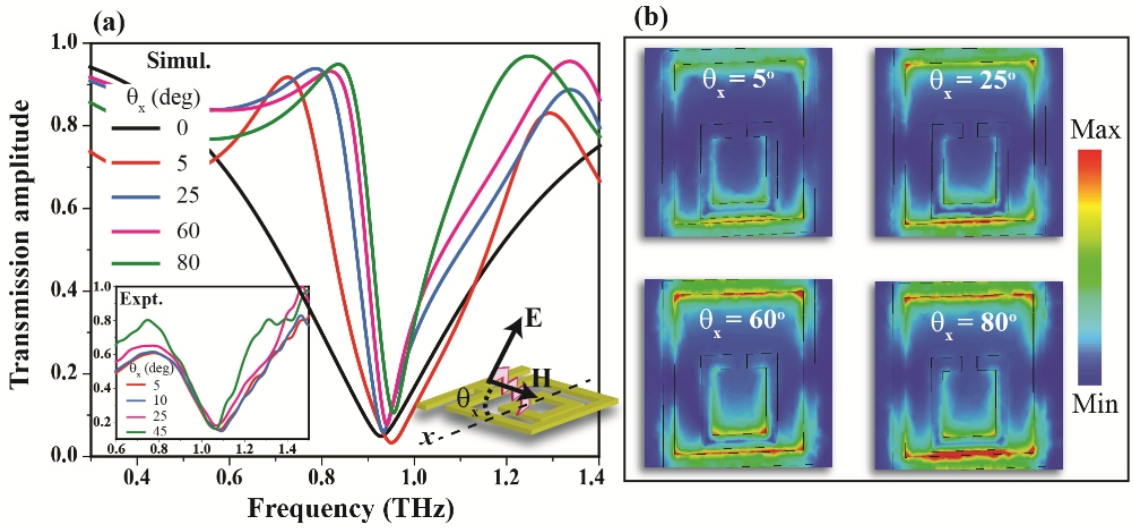


Figure 3.11: Numerically simulated (a) transmission spectra (b) Magnetic distribution plots for varying angle of incidence along x-axis ($\theta_x$) shows that the invisible state of the SRR is preserved under the angle in the angle of incidence. Inset in the Fig (a) shows the experimentally measured THz transmission spectra for varying angle of incidence of THz beam.

To study the effect of incidence angle of the THz light on the SRR-invisibility, numerical simulations were carried out by tilting the angle of the sample to the incident THz light (same as tilting the incident beam angle/oblique incidence) along $x$ and $y$-axis separately. In Figs. 3.11 and 3.12, the numerically calculated far-field transmission response and the near-field energy distribution in the composite MEMS MM device are given for varying angle of incidence ($\theta_x$, $\theta_y$) of the incoming THz

beam. For $\theta_x$ variation, the $H$-component of the THz wave always remain in the plane (along $y$-axis) of the sample and the $E$-component forms a projection along the $z$-axis (out-of-plane) of the sample, whereas for $\theta_y$ variation, the $E$-component of the THz wave remain in the plane (along $x$-axis) and the $H$-component forms a projection along the $z$-axis (out-of-plane) of the sample. Varying the incident angle ($\theta_x$) by keeping the $H$-component of THz wave in the plane of the sample results in the gradual decrease of resonance line width in the far-field transmission spectra with no significant change in its resonance amplitude, as shown in Fig. 3.11(a). Meanwhile, the near-field confinement of the magnetic distribution for varying $\theta_x$ shown in Fig. 3.11(b) highlights gradual increase in the magnetic field confined in the region between the SRR and CRR arms, which therefore results in the significant reduction of the line width of the far-field resonance spectra (Fig. 3.11(a)). Absence of the magnetic field confinement within the SRR for increased incident angles $\theta_x$ affirms that the invisibility of SRR is insensitive (independent) to angle of incidence ($\theta_x$) along the $x$-axis of the sample. The experimentally measured far-field transmission spectra for varying angle of $\theta_x$ are shown in the inset of Fig. 3.11(a) that match well with the resonance narrowing trend seen in the simulation data, where for $\theta_x = 45°$ (green line), the line width of the resonance becomes narrower than for $\theta_x = 5°$ (red line).

On the other hand, when the angle of incidence is varied along the y-axis ($\theta_y$), line width of the far-field spectra becomes narrower till $\theta_y < 80°$, as shown in Fig. 3.12(a), which shows a similar trend in the resonance behaviour seen for $\theta_x$ variation. At $\theta_y = 80°$, the far-field spectrum shows a strong mode splitting characteristic (green line, Fig. 3.12(a)) indicating reappearance of SRR response in the composite MEMS MM device that can be clearly shown by the enhanced magnetic fields near the inductive arm of the SRR shown in Fig. 3.12(b) for $\theta_y = 80°$. At large $\theta_y$, rather than the electric ($E$)-component of the THz wave, it is the magnetic ($H$)-component of the field that directly excites the SRR resonator in the system, thereby making it visible

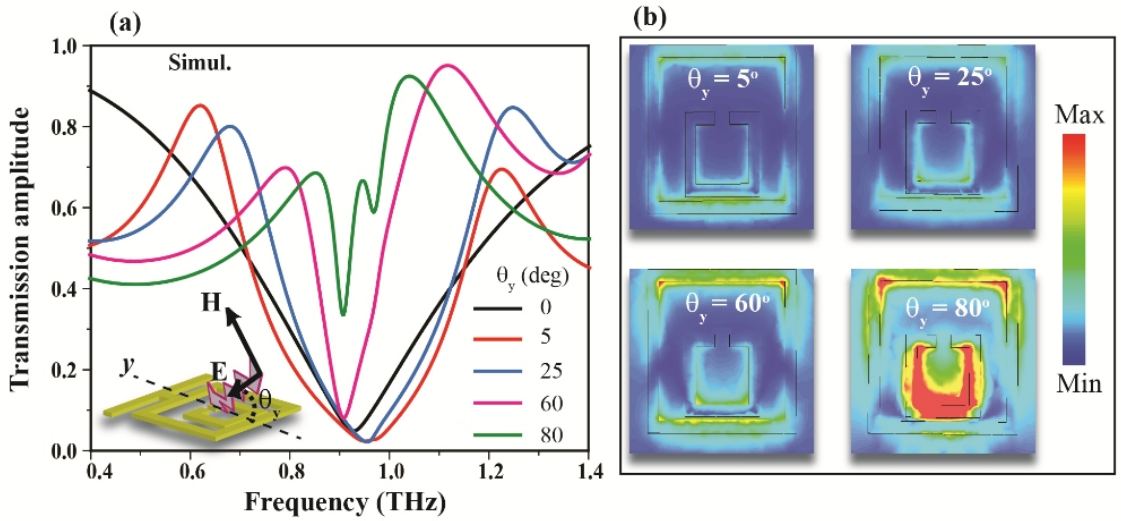


Figure 3.12: Numerically simulated (a) transmission spectra (b) Magnetic distribution plots for varying angle of incidence along x-axis ($\theta_y$) shows that the invisible state of the SRR is preserved under the angle in the angle of incidence. For $\theta_y \geq 80°$, the SRR resonator becomes visible to incident THz light.

to the incident THz wave. The optical response of the sample at larger incident angle ($\theta_x$ and $\theta_y > 45°$) is not realistic in the experimental conditions at THz frequencies, because of the violation of effective and homogeneous medium conditions for the fabricated planar samples. Hence, the reported resonant invisibility of SRR structure to the THz wave with an added advantage of insensitiveness to the angle of incidence benefits the realization of plasmonic/MM coupling induced resonant invisible devices at THz and higher frequencies.

## 3.8 Conclusion

In this chapter, a simple 2-D MM design was proposed to tune the sharp transparency effects and to realize the resonant invisibility of SRR structure in the THz frequencies. In the influence of strong near field magnetic interactions the SRR structure (weak scatterer) placed in the close proximity to the CRR structure becomes invisible to the incident THz light. Further, using the MEMS MM composite design, an active

control of the SRR invisibility is demonstrated that shows a switch between the invisible ($V_{DC}$ = 30 V) and visible ($V_{DC}$ = 0 V) states of the SRR structure to the incoming resonant $E_x$ polarized THz light using a voltage control. Further, active tailoring of the medium parameters- permittivity and permeability, showed that the device can be switched from a rich magnetic medium to a rich electric medium with permeability values of the medium changing from negative to positive values. These magnetic effects are facilitated by the strong bi-anisotropy of the SRR at THz frequencies. The reported invisibility effect of SRR depends on the polarization of the incoming THz beam due to the structural anisotropic nature of the SRR itself, but is insensitive to the incidence angle of the incoming beam. The proposed technique provides a simple design and new way to realize invisibility effects by utilizing the strong resonant near field interactions in the subwavelength structures across large part of the electromagnetic spectrum, thereby circumventing the need for materials with complex geometry and exotic material parameters.

# Chapter 4

# Lattice Induced Transparency (LIT) phenomenon in planar metamaterials.

## 4.1 Introduction: Lattice engineering of near field coupling in metamaterials.

In addition to the intrinsic plasmonic or cavity modes in metamaterials(MMs), there are also dominant intrinsic surface lattice (photonic) modes, which can further couple with the plasmonic modes thereby, enhancing their optical properties. These lattice modes often appear due to the discontinuity in the dispersion curves at the ambient medium-substrate interfaces at Rayleigh cut-off wavelengths[99, 100] of the incident field. These are also referred to as diffractive modes or Wood anomalies[101], whose spectral position depends on the periodicity of the unit cell and the incident angle of the excitation field. The periodic resonant structures such as MMs possess favourable characteristics to probe the effects of lattice interactions on their near- and far-field optical characteristics. For a regular periodic array of resonators illuminated at the

Rayleigh cut-off wavelength, the diffracted beams propagate along the surface of the substrate and interact with resonators thereby giving origin to a lattice mode. These lattice modes are near-field in nature, where their energies are confined or propagated on the resonator surface and fail to propagate to the far-field. They appear in the far-field spectra as a sharp 'kink' possessing extremely high $Q$-factor resonances. For a rectangular periodic array with periodicities given by $p_x$ and $p_y$ for normal beam incidence, the lattice mode frequencies are given by the following expression[99, 100],

$$f_{ij} = \frac{c}{n}\sqrt{i^2(\frac{1}{p_x})^2 + j^2(\frac{1}{p_y})^2} \tag{4.1}$$

Where, $n$ is the refractive index of the substrate, $(i,\ j)$ are the pair of indices determining the order of the lattice/diffractive mode and $c$ is the speed of light in vacuum. For a square lattice period with $p_x = p_y = p$, the expression for the lattice mode frequencies is simplified as,

$$f_{ij} = \frac{c}{np}\sqrt{i^2 + j^2} \tag{4.2}$$

For the first order lattice mode (FOLM), where the indices $(i,\ j) = (1,\ 0)$, the Eqn. 4.2 further simplifies to,

$$f_{10} = \frac{c}{np} \tag{4.3}$$

The anomalies appearing due to diffraction/lattice are intrinsic to subwavelength periodic structures such as MMs and despite their attractive features like extremely narrow resonances and broadband tunability that depends on the lattice geometries, they have not been much explored. In the recent past, there are handful number of works that demonstrated the implications of these lattice modes in the periodic structures. Coupling the plasmonic resonances to the lattice modes has has resulted in resonant suppression in the light extinction[102] and observed extremely high $Q$

resonances at near infrared[103, 104] and far infrared frequencies[105–107] and these observations have not shown any signature that alters the nature of the plasmonic resonance. Enhancing the $Q$-factors by resonantly coupling to the lattice mode resonances to the plasmonic modes have greatly helped in overcoming the limitation of losses in the plasmonic structures by decreasing the radiative losses in the system. On the other hand, Fano type of interference mechanisms such as metamaterial induced transparency effects and Fano resonances in the plasmonic metamolecules have shown greater prospects in realizing the high $Q$-factor resonances by overcoming the material losses in the system[29]. As discussed in the previous chapter 2), these resonances appear due to the destructive interference of the broad bright mode and the discrete dark mode in the system. Such sharp features have been engaged in realizing slow-light devices and ultrasensitive sensors across wide band of far-infrared to visible frequencies. However, the sharpness of these resonance features is limited by the line width or free space coupling factor of the dark mode that hinders in achieving ultra-sharp response features exhibiting steep dispersion for strong slow light effects and for sensor applications. Therefore, in this chapter we discuss a new coupled resonators system where, by coupling a bright resonance with multiple dark resonances will enhance the sharpness of the resulting resonances by increasing the strength of the dark mode interactions in the system.

The current chapter describes a new interaction mechanism involving a bright mode and two dark mode resonances that results in a transparency peak possessing increased sharpness and strong dispersion. We call this phenomenon as Lattice Induced Transparency (LIT), as the intrinsic lattice mode resonantly enhances the strength of the dark mode in the system, thereby resulting in a very sharp transparency peak. Although it involves the Fano-type of interference coupling mechanisms, the proposed LIT system is different from the previously studied classical analogue of EIT systems, as it constitutes coupling between three modes, one bright and two

dark modes, rather than one bright and one dark mode in conventional classical EIT systems[68, 33, 85]. The uniqueness of the current LIT system is that the two dark modes involved in the coupling can enhance the sharpness of the transparency window by an order of magnitude. The transmission peak resulting from LIT effects can be adequately controlled by varying the lattice constant of the MM structure, hence provides an efficient way to modulate frequency, amplitude, and the line width of the transmission resonances. In the following sections, the design and principle of the MM system exhibiting the LIT phenomenon is discussed together with the experimental results on the high $Q$-transmission and strong slow-light effects in the system. A phenomenological model based on the three-oscillator system is proposed, which clearly describes the interaction and effects on the lattice mode on tailoring the transparency peak in the system. The results discussed in this chapter are published in [108].

## 4.2 Design and Numerical Simulations

The proposed MM design for realizing the LIT phenomenon is shown in Fig. 4.1, where the metamolecule consists of two asymmetric split ring (ASRR) resonators structured using the $T = 200$ nm thick aluminium (Al) metal and are separated by $g = 3$ $\mu$m. This structure is famously known as asymmetric split ring MM (ASRR MM) structure that exhibits Fano-type of resonance for the incident field polarized perpendicular to the gap bearing arms of the resonator structure. In the current discussion, the MM response is probed for the incident polarization of light parallel ($E_x$) to the gap bearing arms of the resonators, as highlighted in the figure 4.1. The pair of ASRR structures forms a composite metamolecule that exhibits structural asymmetry with one of the gaps being displaced by $r = 8$ $\mu$m from the center of the resonator arm. In the view of studying the effect of lattice (periodicity) on the structural resonances of the MM, we

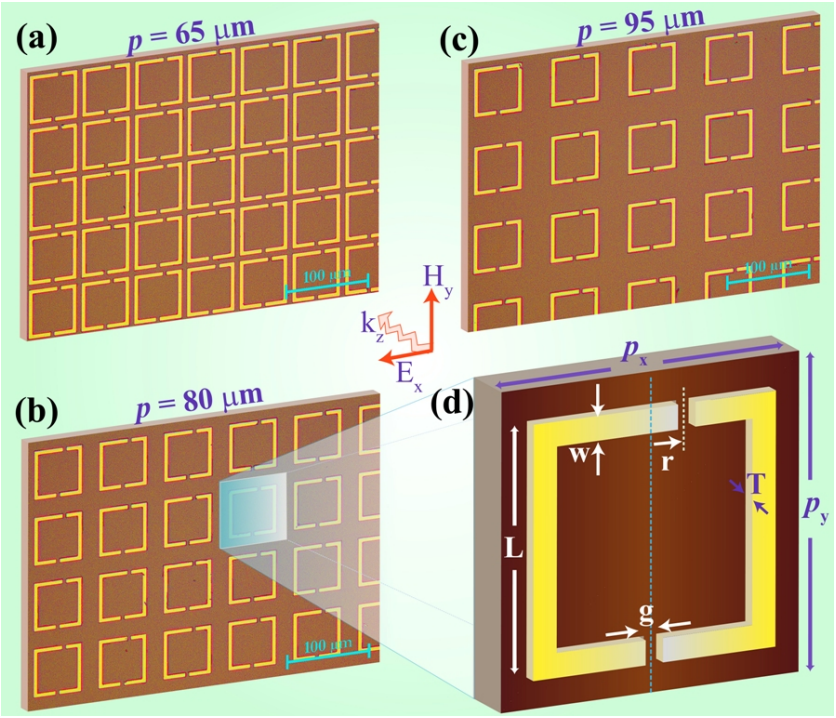


Figure 4.1: (a-c) Optical microscope images of the fabricated ASRR MM (LIT) samples possessing varying periodicities, $p$ = 65, 80 and 95$\mu$m, respectively. (d) Depicting the structural dimensions of the unit cell metamolecule where, length of the resonator arm, $L$ = 60 $\mu$m; width, $w$ = 6 $\mu$m; gap, $g$ = 3 $\mu$m; asymmetry, $r$ = 8 $\mu$m; thickness of metal, $T$ = 200 nm.

considered three designs, each having the same geometrical dimensions for the unit cell metamolecule, but possessing varying periodicities ranging from $p$ = 65, 80 and 95 $\mu$m, as shown in the Fig. 4.1 (a-d). As determined by the Eqn. 4.3, for the MM design with $p$ = 65, 80 and 95 $\mu$m, the first order lattice mode (FOLM) is respectively at the blue side, resonant and at the red side of the dipole resonance frequency of the MM structure. Therefore, by sweeping the frequency of the FOLM across the MM resonance, resonance characteristics of the MM can be tailored adequately.

The numerical simulations were carried out by the help of commercially available CST Microwave Studio software that adopts FDTD methods to calculate the S-parameters in the system. It is important to note that in the numerical simulations, where the resonances possess high $Q$-factors, choice of the material parameters plays

a crucial role[109]. Hence, material parameters for the numerical simulation were chosen to be an aluminium metal with DC conductivity ($\sigma_{DC} = 3.56 \times 10^7$ S/m) as the ASRR metallic resonators and silicon with dielectric constant $\epsilon = 11.66$ used as the transparent substrate at THz frequencies. The simulations were performed using the unit cell boundary conditions in frequency domain solver environment. For each design of the MM, the periodicity of the structure is varied that results in the gradual tuning of FOLM frequency across the dipole resonance of the MM. The lattice constant ($p$) for the MM unit cell is chosen in such a way that for $p = 80$ $\mu$m, the FOLM is precisely matched to the dipole resonance of ASRR structure at 1.1 THz, whereas for $p = 65$ $\mu$m and $p = 95$ $\mu$m, FOLM is towards the blue and the red side of the ASRR resonance, respectively.

The numerically calculated THz transmission spectra through the MM samples excited with the THz wave polarized along $E_x$ direction for $p = 95$, 80 and 65 $\mu$m are shown in Fig. 4.2(a). For $p = 95$ $\mu$m, the transmission spectra shows a broad and asymmetrically shaped dipolar resonance feature for the ASRR structure. In this case, the FOLM frequency is far to the red side (0.9 THz) of the dipolar resonance (1.1 THz) that results in a weak and asymmetric coupling of the lattice mode with the dipole resonance of the MM structure. Despite possessing the structural asymmetry, no mode splitting due to bright-dark coupling is observed as reported by some of the previous works. This is because, for $E_x$ excitation, the dark mode due to structural asymmetry remains unexcited in this system, showing the symmetric dipolar currents running parallel to the polarization of the excitation field, $E_x$ (see Fig. 4.4 (a)). The observed asymmetry in the absorption dip is due to the weak coupling of the dipole resonance with the FOLM appearing at 0.9 THz and the little stronger coupling of the higher order lattice mode appearing at 1.3 THz that corresponds to the higher order (1,1) lattice mode.

When the periodicity of the structure is equal to 80 $\mu$m, the FOLM is resonantly

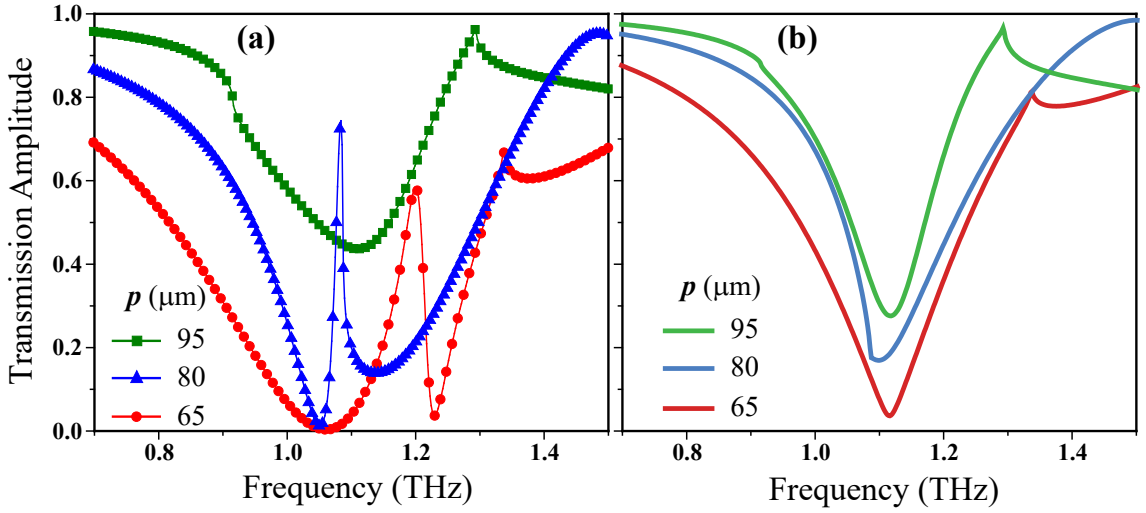


Figure 4.2: (a) Numerically simulated transmission spectra showing the effect of periodicity ($p$) on the ASRR MM resonances leading to the LIT phenomenon. (b) Numerically simulated transmission spectra for symmetric split ring MM designs with varying periodicities, which fails to show the effect of LIT in the structure.

couples to the dipole mode, which results in a sharp transmission window at the resonance. As the $E_x$ polarized light is incident on the sample, broader dipolar resonance centred at 1.1 THz interacts resonantly with weakly oscillating FOLM that propagates on the surface of the substrate. Lattice mode whose energy gets trapped within the MM array couples to the other surface modes rather than to the free space and mediates the excitation of the otherwise unexcited dark mode within the ASRR MM system. This interaction between the broad MM resonance and the weakly excited dark resonance that is mediated by the lattice mode undergo Fano-type of interference to give rise to a sharp transmission window. With further decrease in the periodicity of the structure to 65 $\mu$m, the FOLM is blue shifted with respect to the ASRR MM resonance, which results in the blue shift of the observed transmission peak, as shown by the red circles curve in Fig. 4.2(a). Observed frequency shift of the transparency peak with lattice constant of the unit cell affirms our claim that the resulted transparency is mediated by the lattice mode propagating on the surface of the substrate.

The observed anisotropic type of lattice mode coupling and the excitation in the transparency window at either side of the dipole mode is due to the competing interactions between the change in the lattice mode coupling and the inter unit cell coupling of the neighbouring resonators. For instance, at the lower periodicity of the structure ($p = 65$ $\mu$m), although the FOLM is off-resonant from the dipolar mode, the strong inter-unit cell coupling between the close by neighbouring metamolecules enhances the interactions of FOLM with the dipolar resonance. Therefore, due to the strong FOLM-dipole interactions, a strong and broad transparency peak is observed for $p = 65$ $\mu$m. on the other hand for the ASRR MM sample with $p = 95$ $\mu$m, the separation between the neighbouring unit cell is large and together with the off-resonance of the FOLM with the dipolar mode results in the very weak coupling of the FOLM with the dipolar resonance. Hence, no transmission peak is observed in this case. However, the amplitude and the frequency of the transparency peak are tailored by the coupling of FOLM rather than the inter-unit cell coupling. The inter unit cell coupling just acts an additional coupling term in enhancing the strength of the FOLM coupling to the dipolar mode of the ASRR MM resonator.

In order to understand the role of lattice mode and the structural asymmetry in the lattice induced transparency effects, different configuration of the unit cell structures is considered. A MM structure with its unit cell consists of a pair of symmetric spilt ring resonators is designed with varying lattice constants, $p = 65$, 80 and 95 $\mu$m. The dimensions of the unit cells are same as depicted in Fig. 4.1 (d) except the asymmetry $r = 0$ $\mu$m in this case. The resulting transmission spectrum for the symmetric split rings resonator (SSRR) structures for varying periodicities are shown in Fig. 4.2(b). The results show no signature of transmission peak as the FOLM is swept across the dipolar resonance of the symmetric split ring resonator. These results give an indication that existence of both lattice modes and the asymmetric mode that results from the asymmetry of the structure are necessary condition to realize the lattice

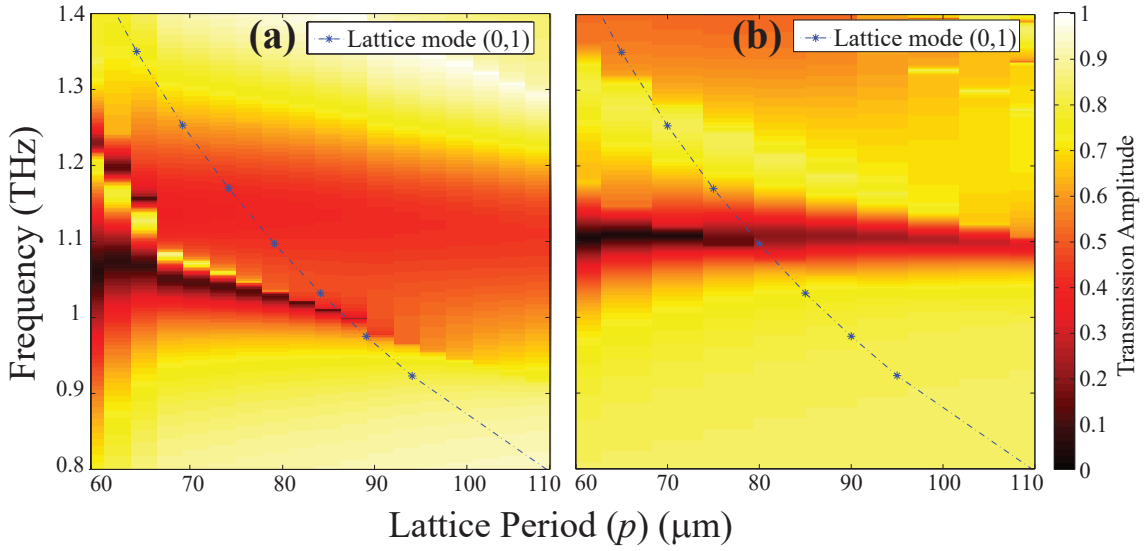


Figure 4.3: (a) The contour plot showing the tuning of transparency peak in the ASRR MM structures for varying periodicities displaying the LIT effect. Frequency tuning of LIT follows the frequency change of the FOLM, as shown by the dotted lines. (b) Contour plot showing the evolution of dipolar resonance the symmetric SRR structure with respect to the variation in the periodicity of the structure. The dotted lines represent the resonance frequency of FOLM calculated using the Eqn. 4.3.

induced transparency phenomenon.

Figure 4.3 provides further evidence that the FOLM, which mediates the LIT, also tunes the frequency of the induced transparency peak to the lower frequencies as it is swept across the dipolar mode of the ASRR MM structure. This behaviour indicates that the as the FOLM is tuned across the MM resonance, it couples strongly to the asymmetric (trapped/dark) mode of the ASRR MM structure thereby enhancing the strength of the trapped mode that results in the strong dipole-trapped mode coupling giving rise to a sharp transmission due to the opposing nature of the fields. Unlike the traditional transparency effects, this lattice mediated and tailored transparency phenomenon can provide an adequately control to modulate frequency, amplitude, and the line width of the transmission resonances by varying the lattice constant of the MM structure. In the SSRR structures, the tuning of the FOLM across the dipole resonance only results in the increasing $Q$-factors without any signature on the mode

splitting behaviour, as shown in Fig. 4.3(b). Here, the presence of the lattice mode (dark mode) is necessary, which mediates and enhances the dark mode (resulting from the asymmetry) strength in the system, thereby strengthening the bright-dark-dark interactions that results in the enhanced and sharp transparency peak. This is supported by the theoretical model based on the three coupled oscillators system, which is further discussed in the following section 4.6.

## 4.3 Surface current and Electric field distributions

The surface current distributions are numerically calculated using the CST microwave numerical solver. The density and directions of the retrieved current distributions provide the strength and the nature of the resonance characteristics observed in the far-field. The underlying phenomenon behind the LIT is further understood by studying the surface current distribution calculated at the resonance dip for $p = 95$ $\mu$m and at the transparency peak for $p = 80$ $\mu$m as shown in Fig. 4.4(a). For the ASRR MM structure with the periodicity, $p = 95$ $\mu$m, the coupling of the dipolar resonance to the FOLM is non-resonant and hence is extremely weak. The resulting surface current distributions at the resonance dip (1.08 THz) reveal a dipolar type of surface currents, where the currents on the resonator arms run parallel to the electric component of the excitation field, $E_x$. When the ASRR MM dipolar resonance is perfectly matched to the FOLM (for $p = 80$ $\mu$m), whose energy is propagated on the surface of the ASRR MM interacts with the asymmetric dipolar resonance to induce the antiparallel currents along the opposite arms of the resonator. These opposing currents are quadrupolar in nature and they run antiparallel to destructively interfere, thereby resulting in the cancellation of the fields at the resonance. This cancellation in the near-fields induced by the opposing surface currents gives rise to a sharp transmission peak and steep dispersion within the system. Thus the nature of

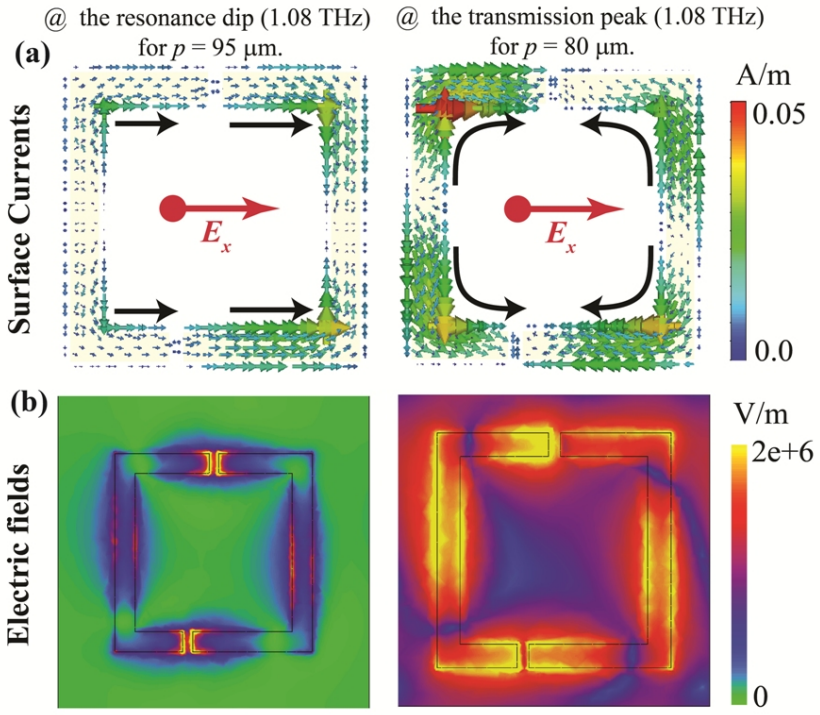


Figure 4.4: Showing the numerically calculated (a) surface currents and (b) electric field distributions at the absorption frequency (1.08 THz) of ASRR MM with $p = 95$ $\mu$m and at the transparency peak of ASRR MM with $p = 80$ $\mu$m, respectively.

the MM resonance is modified by the influence of the lattice mode, which alters the dipolar type of resonance into a sharp transmission feature showing the quadrupolar nature of the surface currents.

The electric field distribution shown in the Fig. 4.4(b) reveals that as the FOLM resonantly couples to the ASRR MM resonance at 1.08 THz ($p = 80$ $\mu$m), the field confinement in the structure drastically increases as compared with the fields for $p =$ 95 $\mu$m ASRR MM structure at the same resonance frequency. This signifies a strong interaction of the surface propagating lattice fields with the dipolar fields in enhancing the electric fields strengths in the structure.

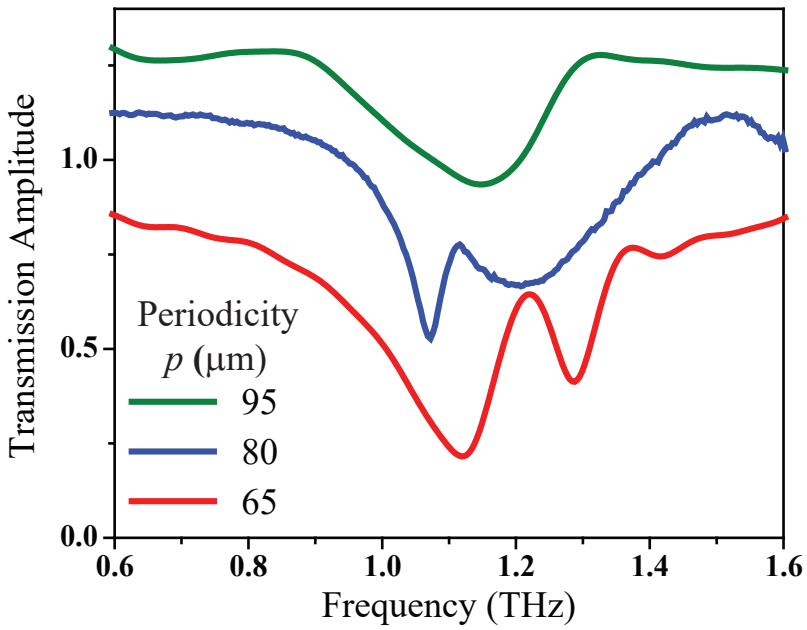


Figure 4.5: Experimentally measured transmission spectra through the ASR MM sample with varying periodicities showing the gradual tuning of lattice induced transparency effect.

## 4.4 Device Fabrication and Experiment

The designed ASRR MM samples with varying periodicities ($p = 65$ $\mu$m, 80 $\mu$m and 95 $\mu$m) are fabricated by using the conventional photolithography technique, where 200 nm thick aluminium metal structures were deposited on a 500 $\mu$m thick high resistivity silicon ($\rho > 5000$ Ω-cm) wafer using thermal evaporation technique followed by the lift-off process in acetone. The optical microscope images of the fabricated samples are shown in the Fig. 4.1 (a), (b) and (c) respectively for $p = 65$ $\mu$m, 80 $\mu$m and 95 $\mu$m. The unit cell dimensions are same for the all three samples with varying periodicities, as shown in Fig. 4.1(d).

THz time domain spectroscopy (THZ-TDS) measurement technique is used to optically characterize the fabricated ASRR MM samples for the normal incidence of the THz pulse. The incident THz pulse has a spot size of 3 mm and is polarized perpendicular ($E_x$) to the ASRR gaps. The measurement was performed in the time

domain by using the standard GaAs photoconductive antenna based THz system that offers high signal to noise ratio (10000:1) in a dry $N_2$ environment. The ASRR MM samples fabricated on the 500 $\mu$m thick double side polished high resistivity silicon substrate ware optically glued to 15 mm thick high resistivity silicon wafer using acetone solution. This method of achieving good optical contact between the two substrates assists in delaying the reflection pulse appearing due to the fabry-perot reflections, which allows long time scan of the THz pulse (about 200 ps) and improves the frequency resolution of our detection to 5 GHz. The optically glued sample was placed at the in the path of the THz beam at its focus for performing THz characterization using the long scan measurements of about 200 ps. The long scan measurements are necessary for the measuring the sharp resonance features possessing high $Q$-factor resonances, where the oscillations in the time signal take very long time to die out. Thus the long scan measurements using the THz-TDS technique is an ideal and useful technique to capture the very sharp resonance features in the photonic structures. The long scan THz time signals were measured through the sample and the substrate, alternatively. The post processed transmission spectra of the sample ($T_{samp}(\omega)$) was normalized to the spectra of the reference substrate ($T_{Ref}(\omega)$) by using the expression $|T(\omega)| = \frac{|T_{samp}(\omega)|}{|T_{Ref}(\omega)|}$ and are shown in the Fig. 4.5. The experimental results reproduce numerical predictions (Fig. 4.2(a)), there by demonstrating the effect of lattice induced transparency in the planar MMs. The small discrepancies seen in the line widths of the measured and simulated values are attributed to the minor imperfections and losses in the fabricated ASRR MM devices.

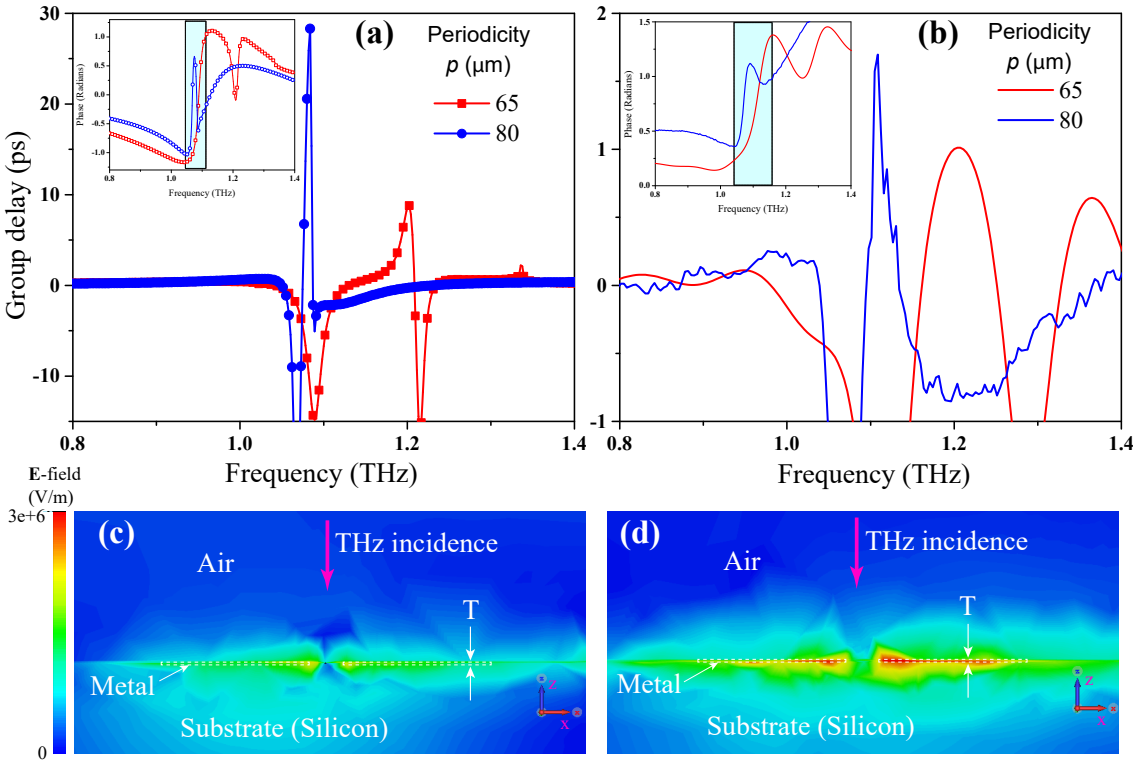


Figure 4.6: (a) Numerically and (b) experimentally calculated group delay values for the ASRR MM medium possessing the periodicity of $p = 65$ and 80 $\mu$m, respectively. The inset figures represent the phase change in the medium for the corresponding ASRR MM structures. (c) and (d) Electric field confinement in the $x$-$z$-cross section plane of the sample at the transmission peaks for $p = 65$ $\mu$m and 80 $\mu$m, respectively. 'T' is the thickness of the resonator metal.

## 4.5 Slow-light effects in LIT medium: Strong dispersion and enhanced group delay

The slow light behaviour in a dispersive medium is quantified by the group delay of the propagating pulse through the interacting medium. As highlighted in the Chapter 2.6, the group delay of the pulse is proportional to the steepness of the phase change (dispersion) within the medium for the propagating pulse at the transmission resonance. Increased sharpness in the resonance feature results in the steep anomalous dispersion that can provide strong slow light effects. In the present scenario of lattice induced transparency, the improved sharpness in the transparency peak observed

due to diffraction coupling induces an anomalous resonant dispersion that greatly enhances the slow-light behaviour within the system. As discussed in the previous chapter 2.6, the slow-light nature of the pulse is quantified in terms of the group delay values extracted from the anomalous change in the phase of the pulse propagating through the medium by using the expression $t_g = -d\phi/d\omega$, where $\phi$ is the phase delay in the pulse propagating through the medium and $\omega$ is the angular frequency of the incident pulse. The simulated and the measured group delay plots for the current LIT medium are shown Fig. 4.6(a). The group delay number obtained from the simulated data for the propagating THz pulse reaches as high as 28 ps for the MM structure resonantly coupled to the lattice mode ($p = 80$ $\mu$m). Since the group delay is proportional to the steep change in the phase (insets of Fig. 4.6) of the THz pulse in the medium, increasing the sharpness of the resonance will show a direct consequence on increasing the degree of phase change in the medium there by, enhancing the group delay for the propagating pulse. By changing the periodicity in the structure to $p = 65$ $\mu$m, due to increased inter unit cell coupling of the neighbouring metamolecules, the line width of the transparency peak increases there by reducing the slope of dispersion in the medium. This results in decrease of the group delay values for the LIT system possessing the periodicity $p = 65$ $\mu$m, as shown in the Fig. 4.6. The maximum group delay value extracted from the simulated data for $p = 65$ $\mu$m is 10 ps at the transmission resonance. Such enhancement in the group delay number for the lattice resonant medium is due to the strong confinement of the surface fields that interact strongly with the incoming light waves. As, shown in the Fig. 4.6(c) and (d), the surface field confinement is stronger for the lattice resonant ($p = 80\mu$m, Fig. 4.6(d)) sample, than for the lattice detuned ($p = 65\mu$m, Fig. 4.6(c)), which enhances the dispersion in the lattice resonant system and hence the larger group delay number. Fig. 4.6 (b) shows the group delay plots for the experimentally measured transmission data, where for $p = 80$ $\mu$m, the measured maximum group

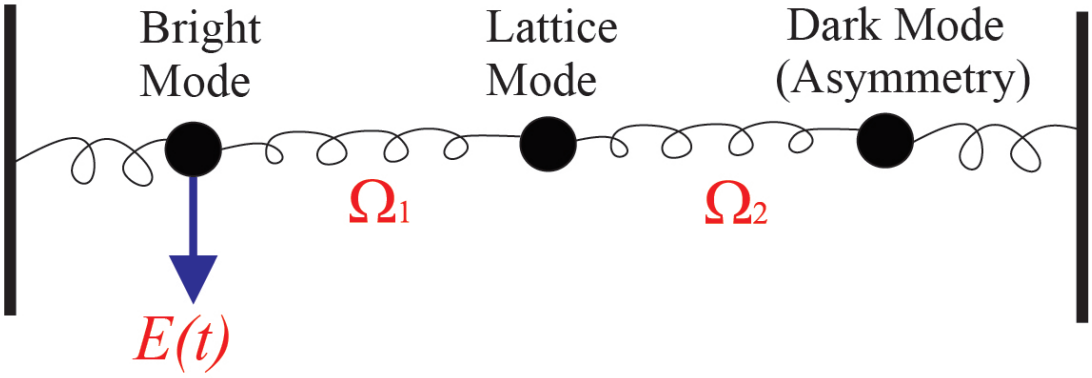


Figure 4.7: Showing the schematic representation of the three-coupled oscillator model mimicking the LIT system, where the lattice mode mediates the coupling between the bright (dipolar) mode and the dark (trapped) mode with the coupling strengths $\Omega_1$ and $\Omega_2$, respectively.

delay value is about 1.75 ps and for $p = 65$ $\mu$m, measured $t_g = 1.2$ ps. The observed large discrepancy in the measured and the simulated group delay numbers are due to the possible imperfections in the fabricated samples and the real material losses that could curb the sharp resonance features in the sample. Since, the lattice coupling is highly sensitive to the angle of incidence of the incoming THz wave, the measurements inaccuracies might also contribute to the lower values of the measured group delay. The reported values on the group delay values for the LIT system are an order of magnitude higher than the reported traditional metamaterial induced transparency effects in the THz part of the electromagnetic spectrum[69, 45, 71, 70]. Recently, such high numbers in the group delay of 25 ps and group index values in the order of $6 \times 10^4$ were reported for lattice enhanced transmission in the periodic array of asymmetric dipoles at THz frequencies [110].

## 4.6 Three coupled oscillator model

To theoretically investigate the coupling behavior responsible for the LIT phenomenon, we employ the coupled oscillator model involving three oscillators system as shown in

the Fig. 4.7 . Unlike in previously studied Fano type of coupled systems (discussed in Chapter 2.7), the currently proposed LIT can be understood as the coupling between three classical oscillators, wherein one of the oscillator, namely the lattice mode mediates the coupling between the bright and the dark mode (resulted from the structural asymmetry) within the system. In the proposed LIT system, bright mode corresponds to the dipolar metamaterial/plasmonic resonance that couples strongly to the incident field ($\mathbf{E}$(t)). The dark mode in the system results from the asymmetry in the structural configuration of the system, whereas the lattice mode arises from the periodicity of the structure and they remain uncoupled to the incident field. The equations of motion for the three coupled oscillators[111–113] namely the bright mode, lattice mode and the dark mode, respectively are given as follow,

$$\ddot{x}_b(t) + \gamma_b \dot{x}_b + \omega_b^2 x_b(t) + \Omega_1^2 x_{LM}(t) = \mathbf{E}(t) \tag{4.4}$$

$$\ddot{x}_{LM}(t) + \gamma_{LM} \dot{x}_{LM} + \omega_{LM}^2 x_{LM}(t) + \Omega_1^2 x_b(t) - \Omega_2^2 x_d(t) = 0 \tag{4.5}$$

$$\ddot{x}_d(t) + \gamma_d \dot{x}_d + \omega_d^2 x_d(t) + \Omega_2^2 x_{LM}(t) = 0. \tag{4.6}$$

The terms ($\omega_b$, $\omega_{LM}$, $\omega_d$) and ($\gamma_b$, $\gamma_{LM}$, $\gamma_d$) represent the angular resonance and the damping frequencies of the bright, lattice mode and the dark mode, respectively. $\Omega_1$ and $\Omega_2$ are the coupling constants/strengths between the bright-lattice modes and the lattice-dark modes, respectively. The signs of the coupling strengths and in the above expressions signify the nature of coupling in the entire system. It is worth noting that the coupling of the bright mode to the dark mode is mediated by the lattice mode that results in the transparency window as described by the above coupled expressions (Eqns. 4.4-4.6). The Fourier transformation of Eqns. 4.4, 4.5, and 4.6 leads to the following expressions for the scattering amplitudes in the frequency domain.

$$(-\omega^2 - i\omega\gamma_b + \omega_b^2)\widetilde{x}_b + \Omega_1^2 \widetilde{x}_{LM} = \widetilde{E}(\omega) \tag{4.7}$$

$$(-\omega^2 - i\omega\gamma_{LM} + \omega_{LM}^2)\widetilde{x}_{LM} + \Omega_1^2\widetilde{x}_b - \Omega_2^2\widetilde{x}_d = 0 \tag{4.8}$$

$$(-\omega^2 - i\omega\gamma_d + \omega_d^2)\widetilde{x}_d + \Omega_2^2\widetilde{x}_{LM} = 0 \tag{4.9}$$

Upon solving coupled equations 4.7, 4.8, and 4.9, we arrive at the analytical expression for the scattering amplitude for the bright eigen mode and is given by,

$$\widetilde{x}_b = \frac{-E(\Omega_2^4 + (\omega^2 - \omega_{LM}^2 + i\omega\gamma_{LM})(\omega^2 - \omega_d^2 + i\omega\gamma_d))}{((\Omega_2^4 + (\omega^2 - \omega_{LM}^2 + i\omega\gamma_{LM})(\omega^2 - \omega_d^2 + i\omega\gamma_d))(\omega^2 - \omega_b^2 + i\omega\gamma_b)) - \Omega_1^4(\omega^2 - \omega_d^2 + i\omega\gamma_d)} \tag{4.10}$$

Eqn. 4.10 is a more generalized expression for the three coupled oscillators system. We relate the above expression (Eqn. 4.10) to the mechanisms responsible for the LIT in the system, where the resonance nature of the dark mode is dictated and tuned by the lattice mode resonance and hence we consider $\omega_d = \omega_{LM}$ and $\gamma_d = \gamma_{LM}$ in the Eqn. 4.10. With these realistic considerations, the scattering amplitude for the bright mode (Eqn. 4.10) can be further simplified as,

$$\widetilde{x}_b = \frac{-E(\Omega_2^4 + (\omega^2 - \omega_{LM}^2 + i\omega\gamma_{LM})^2)}{((\Omega_2^4 + (\omega^2 - \omega_{LM}^2 + i\omega\gamma_{LM})^2)(\omega^2 - \omega_b^2 + i\omega\gamma_b)) - \Omega_1^4(\omega^2 - \omega_{LM}^2 + i\omega\gamma_{LM})} \tag{4.11}$$

Using the expression 4.11, we plot the transmission (1 - Im[$x_b$]) by varying the resonance frequency of the lattice mode ($\omega_{LM}$) for the following set of realistic system parameters, $\Omega_1 = \Omega_2 = 1$, $\omega_b$= 6.9, $\gamma_b = 1$, $\gamma_{LM} = 0.15$ and $E = 0.17$, the results are shown in Fig. 4.8(a). The lattice mode frequencies, $\omega_{LM}/2\pi$ = 0.9 THz, 1.084 THz and 1.2 THz in Fig. 4.8(a) correspond to the lattice periodicity of $p$ = 95 $\mu$m, 80 $\mu$m and 65 $\mu$m of Fig. 4.2(a), respectively. It is worth noting that the proposed theoretical model (Eqn. 4.11) does not take into account of near field influence due to inter unit cell coupling for varied periodicities. Hence, there are little discrepancies

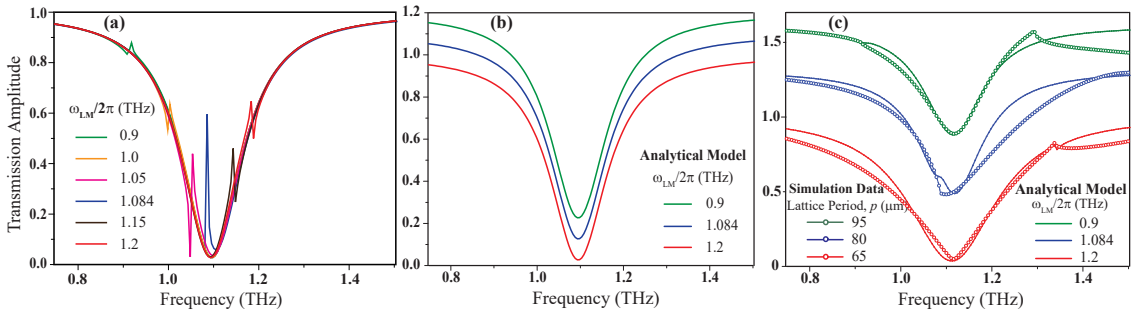


Figure 4.8: Showing the schematic representation of the three-coupled oscillator model mimicking the LIT system, where the lattice mode mediates the coupling between the bright (dipolar) mode and the dark (trapped) mode with the coupling strengths $\Omega_1$ and $\Omega_2$, respectively.

observed in the line widths of the theoretical curves and the simulated/experimental results for the periodicity $p$ = 65 $\mu$m, 80 $\mu$m and 95 $\mu$m (see, Fig. 4.2(a)). In experiments, as the periodicity is decreased from 80 $\mu$m to 65 $\mu$m, it strengthens the inter unit cell coupling that in turn increases the amplitude and the line-width of the transparency peak (this is the case, when $\omega_{LM}$ is blue side of the plasmonic resonance) whereas, when the periodicity of the structure is increased to 95 $\mu$m, the inter unit cell coupling weakens resulting in a very weak excitation of the transmission peak (this is the case when $\omega_{LM}$ is red side of the plasmonic resonance). Apart from these discrepancies, the theoretical curves show a very good agreement with the simulation and the experimental results shown in the Figs. 4.2(a) and 4.5.

To further check the validation of the proposed model, we perform more investigations by altering the coupling terms $\Omega_1$ and $\Omega_2$ in the coupled oscillator expression (Eqn. 4.11). For the case of $\Omega_1 = 0$ (i.e. the lattice mode is decoupled from the bright mode, refer Fig. 4.11), we see no change in the resonance of the system as the lattice mode is scanned through the entire spectrum of the plasmonic mode, as shown in the Fig. 4.8(b). This signifies that in the absence of the lattice coupling, the resonance response of the system is dominated by the dipolar nature of the plasmonic resonance as expected. On the other hand, for $\Omega_2 = 0$, where the dark mode due

to the structural asymmetry is absent, there is a weak coupling observed between the plasmonic mode and the resonant lattice mode, as shown by the curves in Fig. 4.8(c). The theoretical curves show good agreement with the simulation results for the symmetric structures, where dark mode due to structural asymmetry is absent. The weak asymmetric resonances observed around 0.9 THz, 1.1 THz and 1.3 THz are due to the weak interaction of the plasmonic mode with the resonant lattice mode resonance. In the presence of both the coupling terms ($\Omega_1$ and $\Omega_2$), the system shows sharp transmission resonances in the vicinity of the sub-radiant lattice modes. These studies infer that the observed results are in fact arise from the collective interaction of the lattice mode with the bright plasmonic mode and the asymmetric dark mode. As the LIT system involves two sub-radiant modes interacting to each other, a very sharp transmission resonance can be realized with higher $Q$-factor and larger group delays in comparison with the regular classical Electromagnetically Induced Transparency (EIT) systems discussed in chapter 2.

## 4.7 Photoactive tuning of Lattice Induced Transparency

Integrating the dynamical semiconducting materials with the metamaterial structures has allowed manipulating their resonance characteristics in an active way by changing the conducting properties of the semiconductor using the optical pump pulse[56, 95, 45, 114]. The active control of metamaterial properties has benefited the relevance of these devices in the real world applications. In this section, an active way of controlling the lattice induced transparency and dynamic tuning of coupling between the lattice first order lattice mode with the dipolar mode of metamaterial is discussed. By closing the gaps in the asymmetric resonators by using the photoactive silicon patches assists in reconfiguring the geometry of the structure, thereby tuning the

frequency of the dipolar resonance in the structure way from the lattice mode. Such systems can enable the realization of active slow light devices and resonant switches at far-infrared frequencies.

### 4.7.1 Design and Fabrication

The active lattice induced transparency (LIT) design consists of an asymmetric arrangement of a pair of SRR structures made of aluminium (Al) metal possessing a total structural asymmetry of $2r = 10$ $\mu$m fabricated on a silicon on sapphire substrate. The active SoS sample fabrication process is detailed in the chapter 1.4. Optical microscope image of the fabricated sample is shown in Fig. 4.9, where the silicon patches are placed in the gaps of the asymmetric pair of SRR structures. The unit cell dimensions of the LIT structure possessing the square periodicity of $p_x = p_y = p =$ 105 $\mu$m are given in the inset of Fig. 4.9. The periodicity of the structure defines the lattice mode of frequency (Eqn. 4.3) of the structure that appears at 0.84 THz. The geometry and dimension of the ASRR structure is chosen such a way that the for $E_y$ excitation the dipolar resonance of the ASRR metamaterial structure matches with the lattice mode frequency, which results in the sharp transparency peak as discussed in the previous sections 4.2. Here, by actively tuning the resonance frequency of the ASRR's dipole resonance, the coupling between the lattice mode and the dipole resonance mode is tailored.

### 4.7.2 Results and Discussion

In the previous discussion, passive tuning of the LIT, where the periodicity of the structure was varied to tune the resulting LIT peak across the dipole resonance of the ASRR structure. Here, the lattice frequency is kept constant defined by the square periodicity $p = 105$ $\mu$m, and the dipole resonance frequency is tuned by shorting the

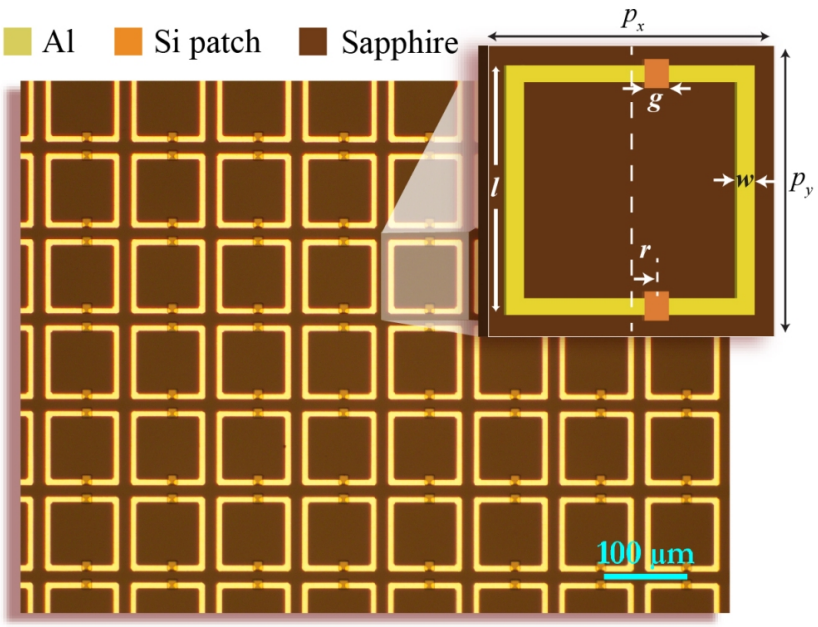


Figure 4.9: Optical microscope image of the fabricated active LIT sample on the SoS substrate. The inset shows the unit cell dimensions, where resonator length, $l = 90$ $\mu$m; width, $w = 6$ $\mu$m, gap, $g = 4$ $\mu$m, one side asymmetry, $r = 5$ $\mu$m (total asymmetry $2r = 10$ $\mu$m) and the square periodicity of $p_x = p_y = p = 105$ $\mu$m.

gaps of the ASRR structures using the photoactive silicon patch. The measured and simulated transmission response of the active LIT sample are shown figure 4.10 (a) and (b), respectively. The measurement of the sample was done using ZnTe based optical pump-terahertz probe (OPTP) system (discussed in chapter 1.1.2), where 800 nm of femtosecond optical pump beam of wavelength 800 nm is incident on the surface of active LIT MM sample and the photoresponse of the dressed MM sample is probed using the normal incidence of time matched THz pulse of beam diameter 4 mm. The pump beam has a diameter of 10 mm and is derived from an amplified laser of pulse width 120 fs and repetition rate of 1 kHz.

In the absence of pump beam, the sample exhibits a strong transparency peak at 0.9 THz as shown in the Fig. 4.10 (a). This transparency is a result of lattice mode coupling to the dipole resonance of the asymmetric structure as discussed in the previous sections. Upon shining the pump beam on the sample the strength of the

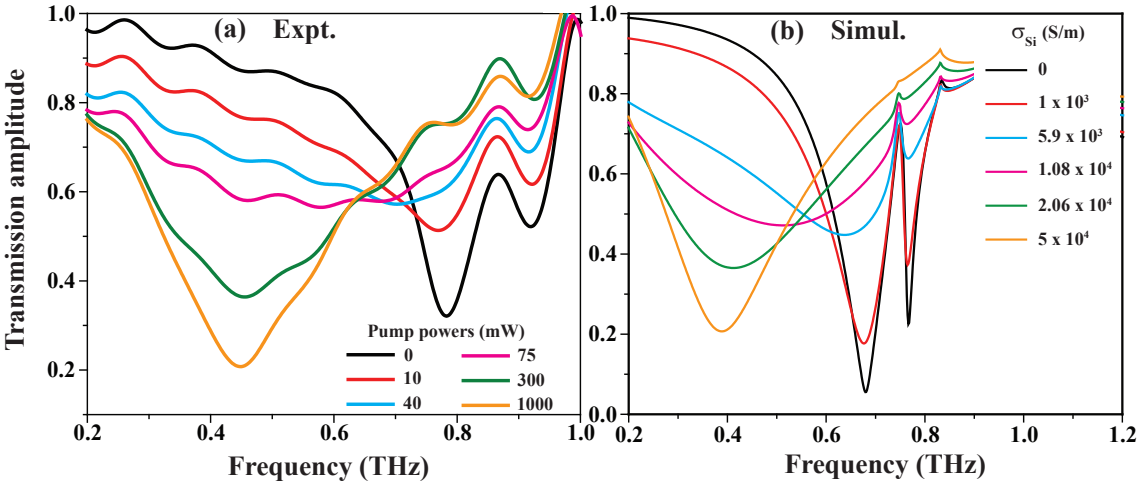


Figure 4.10: (a) Experimentally measured and (b) numerically simulated transmission spectra of the active LIT device showing the gradual tuning of transparency peak and the lattice-dipole coupling for varying incident pump powers and change in conductivity of the silicon patches, respectively.

transparency peak reduces with increasing pump power (10 mW) as shown by the red curve in Fig. 4.10 (a). With further increasing pump powers, the dipole resonance of the ASRR gradually red shifts and decouples from the lattice mode thereby completely cancelling the transparency effects in the system (shown by orange curve in Fig. 4.10 (a)). The reason being, as the pump beam photoexcites the silicon patches present in the gaps of the ASRR structures, the photoconductivity of the silicon increases with increasing pump powers and behaves as a semimetal at higher pump powers. As a result the gaps ($g$) are shorted that increases the total length of the resonator, thereby decreasing the frequency of the dipolar resonance. Hence, the shorted structure behave as a conventional symmetric dipolar closed ring resonator possesing a strong dipole resonance at 0.5 THz. Thus, by using the photoactive control the lattice mediated transparency effects can be adequately controlled, that can show potential applications as active modulators, filters and slow light devices. Fig. 4.10 (b) shows the numerical simulations of the transmission response through the sample by uniformly varying the conductivity of the silicon patches present in the two gaps of the unit cell. The results show good agreement with the experimental results with the pump powers showing

the approximately one-to-one correspondence to the conductivity values of silicon.

## 4.8 Conclusion

In this chapter a new mechanism of inducing a sharp transparency peak by coupling the first order lattice mode of the metamaterial with the dipole resonance of the asymmetric split ring resonator structure was demonstrated. Resonant coupling of the lattice to the metamaterial resonance showed a sharp transparency window with a steep dispersion in the system. Since the lattice guided modes are intrinsic to the periodic structures and can be tuned by varying the periodicity of the structures, it can help in realizing frequency agile transmission resonances. The resulted steep dispersion and the strong confinement of the electric field on the surface of the metamaterial showed large enhancement in the group delay (20 ps) for the propogating beam in the MM medium at the transparency peak. A three coupled oscillator model was proposed to elucidate the coupling mechanisms responsible for the LIT effect, that revealed the interaction of two dark modes (lattice and asymmetric mode) with a bright dipole mode, which results in enhanced sharpness of the transparency peak. Last part of the chapter showed the photoactive control of LIT phenomenon using a external optical pulse that actively manipulates the coupling between the lattice mode the dipole mode of the asymmetric resonator structure by changing the resonance frequency of the dipole mode. These results show promising pathways for realizing ultra-sharp transmission resonances to enhance the light-matter interactions by compensating for the material losses in the metamaterial structure. These devices can find potential applications as slow light devices, modulators and nonlinear devices operating from microwaves to optical frequencies.

# Chapter 5

# Excitation and Active control of Fano resonances in MEMS Metamaterial

## 5.1 Introduction: Fano resonances in Metamaterials

The ability of MMs to engineer their optical properties by precisely configuring their shape and geometry has resulted in formation of new resonance features possessing extremely high $Q$-factors and strong electric field enhancement in the vicinity of the structures. These effects include the excitation of Fano resonances[29], metamaterial/plasmon induced transparency effects[33, 34] and the recent demonstration on toroidal resonances[115]. The Fano resonances in these structures result from the structural asymmetry along the axis parallel to the polarization of the excitation beam. These resonances are spectrally asymmetric in nature and results from the interference between the excitation pathways of the discrete resonance within a broad continuum. Typically, the symmetric spectral features such as Lorentzian line shapes

are described by the Lorentz model that result from overlapping of distinct resonances of different origin, whereas the asymmetric spectral features showing the Fano line shape is a consequence of the Fano type of interference effects in the system. The first theoretical explanation of the Fano resonance was given by Ugo Fano[116] while understanding the discrete and asymmetric spectra features formed by the excitation within auto-ionizing states of helium atoms. Since then there have been enormous interest in studying the significance of Fano resonances in the classical[29, 117] and in quantum atomic systems. The high $Q$ nature of Fano resonances in the metamaterial and plasmonic system have been used to demonstrate ultrasensitive sensors[37, 118], lasing spasers[40] and nonlinear devices[46] across major part of EM spectrum.

This chapter focuses on active excitation and manipulation of Fano resonance feature in a out-of plane reconfigurable MEMS MM system and its potential applications in the field of photonics and communications. The out-of plane reconfiguration of the MEMS microcantilever structure is performed using two independent voltage controls that provides an unique feature and flexibility of probing the near-field interactions in the $z$-direction of the sample. This helps in exploring the nature of exponential decay of the near-field in the $z$-direction of the MM sample near its surface. In the following sections, the design, fabrication and the THz characterization of the MEMS Fano-MM device are discussed together with highlighting on the intrigue features of the Fano excitation in the device. The results discussed in the this chapter are published in [119].

## 5.2 Design and Fabrication

The MEMS Fano-MM design consists of a pair of symmetric split ring resonators (SRR-1 and SRR-2) attached to the electrically isolated metal lines that are connected to the voltage sources $V_1$ and $V_2$ thereby, allows for their independent structural

reconfiguration along the $z$-direction of the metadevice. The selective control at the sub-unit cell level provides the flexibility to introduce a dynamically tunable structural asymmetry along the $z$-axis of the structure, described by the effective structural asymmetry parameter, $\delta = |\frac{(h_1-h_2)}{s}| \times 100\%$, where ($h_1$, $h_2$) and $s$ are the inclination heights and length of the microcantilever arms of SRR-1 and SRR-2, respectively. Experimentally, control of the asymmetry parameter ($\delta$) is dictated by the differential voltage between the two resonators SRR-1 and SRR-2, defined as $\Delta V = |\ V_1 - V_2|$. The periodic array of SRRs made of 900 nm thick aluminum are patterned on top of 50 nm aluminum oxide ($Al_2O_3$) dielectric (forming a bimorph layer), fabricated on a lightly doped silicon (Si) substrate using complementary metal-oxide-semiconductor (CMOS) compatible process (ref. Chap. 1.4 for detailed fabrication process). Due to the residual stress in the bimorph layers ($Al/Al_2O_3$), the microcantilevers are bent up, thereby increasing their released heights ($h_1$ and $h_2$).

An artistic representation of the device is shown in the Fig. 5.1 (a) along with the unit cell dimensions given in the inset figure. In Fig. 5.1(b-d) SEM images of the fabricated device are shown representing the various actuation states of the device starting from the symmetric configuration ($\delta = 0$) in the released states ($h_1 = h_2 = h_{max}$) (Fig. 5.1(b)) to the intermediate state with the maximum asymmetry ($h_1 \neq h_2$, $h_2 = 0$) (Fig. 5.1(c))and finally bringing back to the symmetric configuration ($\delta = 0$) with $h_1 = h_2 = 0$ (Fig. 5.1(d)), where both the cantilevers are brought in contact with the substrate.

The electromechanical characterization of the MEMS Fano-MM device is performed using Lyncee Tec. reflection digital holographic microscope (R-DHM), where the deflection/actuation profiles of released microcantilevers are measured. The released chips are wire bonded to a printed circuit board (PCB). Separate voltage supplies ($V_1$ and $V_2$) are used for the actuation of SRR-1 and SRR-2 microcantilevers, respectively. Silicon (Si) substrate was chosen as the ground potential, and the

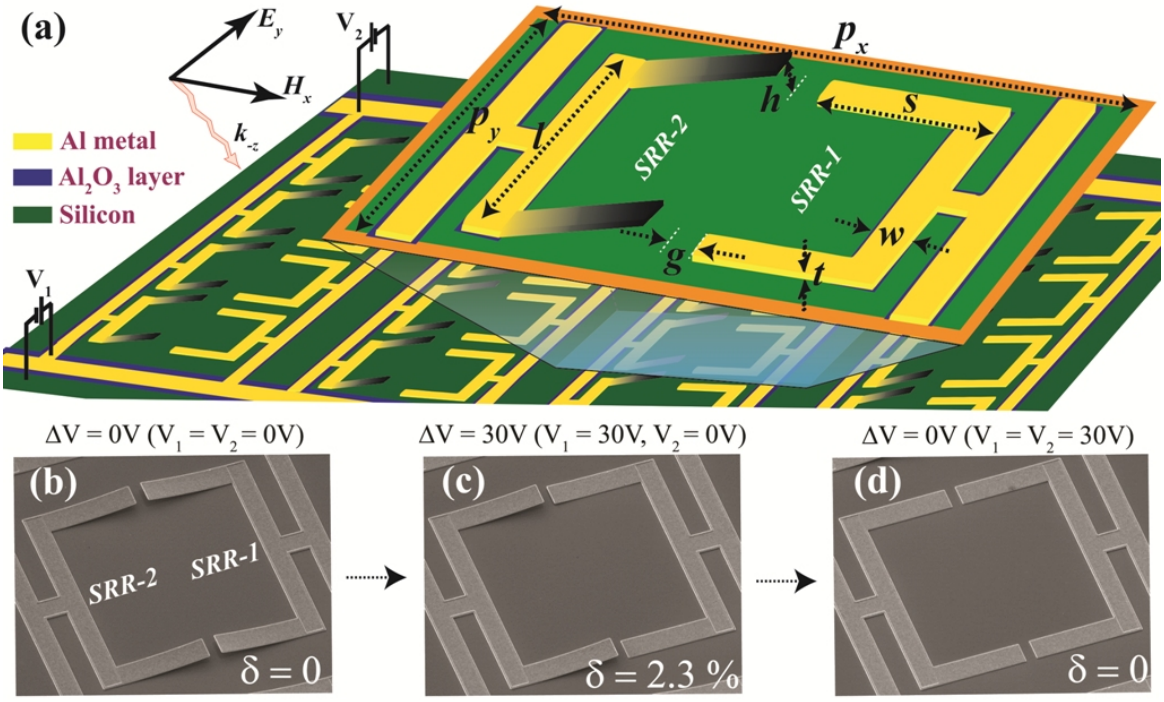


Figure 5.1: (a) Schematic and the unit cell representation of the MEMS Fano-MM device. The unit cell comprises of two SRRs separated by a gap $g$ and their microcantilever arms of length $s$ are released at a height $h$. The dimensions are periods $p_x = 110$ $\mu$m; $p_y = 75$ $\mu$m; resonator length, $l = 60$ $\mu$m ; microcantilever length $s = 25$ $\mu$m ; width, $w = 6$ $\mu$m ; gap, $g = 4$ $\mu$m ; and metal thickness $t = 900$ nm. (b-d) Optical microscopy images of the unit cell showing the sequential actuation of SRRs, where the sequence from (b) to (c) represents the increasing asymmetry ($\delta$) and (c) to (d) represents the decreasing asymmetry ($\delta$) configuration.

microcantilevers are positively biased. When voltage is applied across the released cantilevers and Si substrate, the attractive electrostatic force deforms the suspended cantilevers towards the fixed Si substrate. This mechanical deformation of cantilevers induces a restoring force that opposes the electrostatic force causing the deflection at the first place. Hence, the final position of the cantilever at a given voltage is determined by the equilibrium position, where the electrostatic force and restoring force balances each other. As discussed in the previous chapter 1.2.1, once the applied voltage increases, the electrostatic force increases much higher than the restoring force and at a critical value known as the Pull in voltage ($V_{pi} > 25$ V), the electrostatic force will be higher than the restoring force, thereby bringing the microcantilevers to

be in physical contact with Si substrate (shown in inset of Fig. 5.2(a)).The pull-in can be clearly observed through the optical microscope fitted on the R-DHM. The $Al_2O_3$ layer beneath the Al layer, will ensure that there is no current flowing from Al layer to Si substrate, when pull in occurs. This is crucial because if the current flows through the Al/Si junction, then the temperature will rise up locally thereby melting the Al tips with the Si substrate, and will cause a permanent damage to the device.

## 5.3 Active control of Fano resonances

The MEMS Fano-MM is optically characterized using a conventional GaAs photoconductive switch based THz-time domain spectroscopy system operating in the transmission mode. The wire bonded MM sample is positioned at the focus of the THz beam. The electrical connections to the SRR-1 and SRR-2 resonators structures are established using a two channel variable DC voltage source. The transmission measurements were performed for the sequential and continuous variation of voltages $V_1$ and $V_2$ connected to the SRR-1 and SRR-2 resonators, respectively. The measurements were carried out following the THz-TDS procedures discussed in Chap. 1.1.1 for each configuration of the applied voltages continuously varying from $V_{1,2} = 0$ V to 35 V in steps.

The measured transmission spectra for the continuous and sequential increase of $V_1$ and $V_2$ are shown in Fig. 5.2(a) and (b), respectively, where the inset diagram in (b) presents the experimentally measured electrostatic actuation of the cantilevers by applying the voltage on one of the resonators' arm using the R-DHM characterization. Initially, for the case where no voltage is applied across the resonators i.e. $V_{1,2} = 0$ V, the two SRR arms are symmetrically inclined ($\delta = 0$) along the $z$-direction that results in the excitation of strong dipole type of resonance at 0.78 THz for the incident THz radiation polarized in the $E_y$ direction. When voltage ($V_1$) is applied across

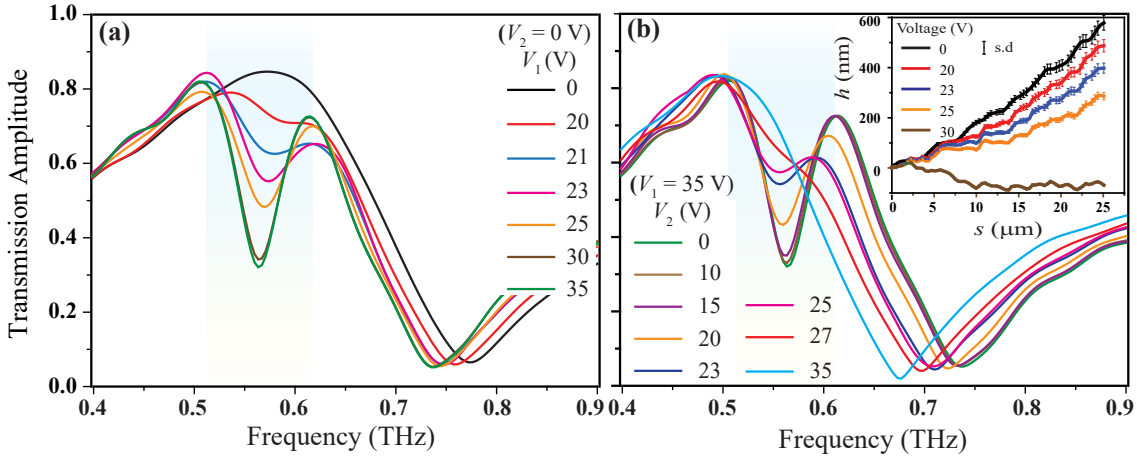


Figure 5.2: Experimentally measured THz transmission spectrum of the MEMS Fano-MM device for (a) increasing asymmetry ($V_1$ varying and $V_2 = 0$ V) and (b) decreasing asymmetry ($V_2$ varying and $V_1 = 35$ V) configuration of the device. The inset figure in (b) represents the experimentally mapped actuation angles under the applied voltage for the designed MEMS structure using R-DHM technique.

the Al lines of the released cantilevers of SRR-1 and Si substrate, the cantilevers gradually deflect toward the fixed substrate due to the attractive electrostatic force. This deformation in the height of one of the cantilevers due to the applied finite $\Delta$V across two resonators creates the structural asymmetry ($\delta$) along the $z$-axis of the sample. As a result, near field coupling between the asymmetric structures exhibits Fano type of interference effects that excites a sharp trapped mode (Fano-type) resonance feature (at 0.6 THz) within a broad dipolar resonance. This Fano feature is a consequence of the destructive interference between the broad dipolar mode of the resonator structure and the dark (discrete) mode that results form the asymmetry in the structure. This dark asymmetric mode weakly couples to the free space field thereby trapping all the energy on the surface of the resonator sample, thus strongly enhancing the confinement of the electric/magnetic energy in the gaps of the resonator structures. Upon continuously increasing $V_1$, the amplitude/intensity of the Fano resonance grows stronger and reaches its maximum value for $V_1 = 35$ V (and $V_2 = 0$ V), as shown in Fig. 5.2 (a). Subsequently, when the voltage $V_2$ is

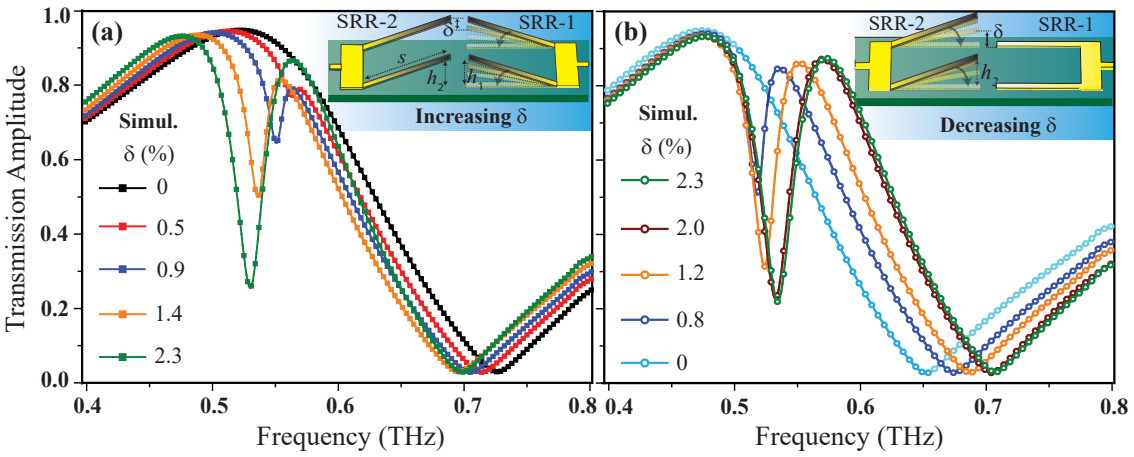


Figure 5.3: Numerically simulated THz transmission spectrum of the MEMS Fano-MM device for (a) increasing asymmetry and (b) decreasing asymmetry configuration of the device. The asymmetry values given in the legends show one to one correspondence with the voltage values given in Fig. 5.2, respectively.

applied across SRR-2, its cantilever arms are gradually pulled towards the substrate and thereby reducing the asymmetry in the structure. Therefore, the amplitude of Fano resonance starts to weaken and shows a monotonic decrease with increasing $V_2$ and completely diminishes as the $V_2$ finally reaches 35 V, as shown in Fig. 5.2(b). In this final configuration, both SRR-1 and SRR-2 are snapped down on the substrate with $V_1 = 35$ V and $V_2 = 35$ V, (i.e. $\Delta V = 0$), thereby restoring the symmetry of the structure.

The correlation between the sequential voltage actuation in the experiment and to the asymmetry $\delta$ of the structure is established by the numerically simulated transmission spectrum performed using finite difference time domain (FDTD) calculations offered by commercially available CST microwave studio software (ref. Chap. 1.3), as shown in Fig. 5.3(a) and (b). The value of the structural asymmetry parameter ($\delta$) is estimated based on the experimentally measured dissimilarities in the inclined heights of the cantilevers of resonators SRR-1 and SRR-2 using the expression for $\delta$ defined in the previous sections. The insets in Fig 5.3(a) and (b) represents the schematic showing the sequential actuation of SRR-1 and SRR-2 resonators that corresponds

to the continuous increase and decrease in the structural asymmetry parameter ($\delta$), which signifies one complete ramp of the asymmetry parameter from a symmetric state (both cantilevers are released) to maximum asymmetric state and back to symmetric configuration (both cantilevers are down). The simulated transmission spectra show good agreement with the experimental results in Fig. 5.2, where initially, while both cantilever arms of SRR-1 and SRR-2 are inclined at a height $h_1$, $h_2 = h$ ($\delta = 0$), the system is symmetric and exhibits a dipolar type of resonance. As $\delta$ in the system increases, the transmission spectra shows gradual increase in the Fano resonance strength. While on the other hand, subsequent decrease in $\delta$ of the structure by decreasing the height $h_2$ of SRR-2, results in weakening of Fano resonance and is completely switched-off when SRR-2 arm is snapped down on the surface of the substrate (brings back to symmetric state with $h_1 = h_2 = 0$).

## 5.4 Multiple input-output (MIO) states : Meta-hysteresis

As of now, the optical characterization in metamaterials have been majorly restrained to investigating the system responses in terms of single-input-output (SIO) configurations. In our current MEMS Fano-MM design using the two independent voltage controls ($V_1$ and $V_2$) the optical characteristics can be maneuvered to show multiple-input-output (MIO) behavior in the electro-optical properties of Fano resonances. These MIO states resemble the closed loop hysteritic properties in the near- and the far-field properties of the MEMS Fano-MM. MIO states are created by the anistropic type of excitation of the Fano resonance using the nonlinear spatial distribution of the near fields extended along the $z$-axis during increasing and decreasing pathways of the asymmetry parameter ($\delta$) in the structure. This distinctive behaviour in the Fano excitation is more clearly shown in terms of change in the Fano resonance

transmission intensity ($|\Delta T|$), with respect to change in the differential voltage ($\Delta V$). The differential volatge is defined the volatge dirrence bewnn the two input voltages $V_1$ and $V_2$ for a constant asymmetry parameter (i.e. $\Delta V = |V_1 - V_2|$ at constant $\delta$). In Fig. 5.4 (a), the variation in $|\Delta T|$ for the measured Fano transmission data is is plotted with respect to $\Delta$V that demonstrates distinctive variation pathways for $|\Delta T|$ signifying an a hysteretic-type of closed loop behavior. Although this scenario showing the distinctive pathways resembles the hysteresis behavior observed in many natural materials[82], but indeed it is two output states for two input controls ($V_1$ and $V_2$) (MIO characteristics) to form a closed loop in $|\Delta T|$. Hence, we term the observed phenomenon as $meta - hysteresis$, as a hysteresis type of loop in a pure metamaterial system can be artificially created and engineered by using intriguing near-field properties of the MM.

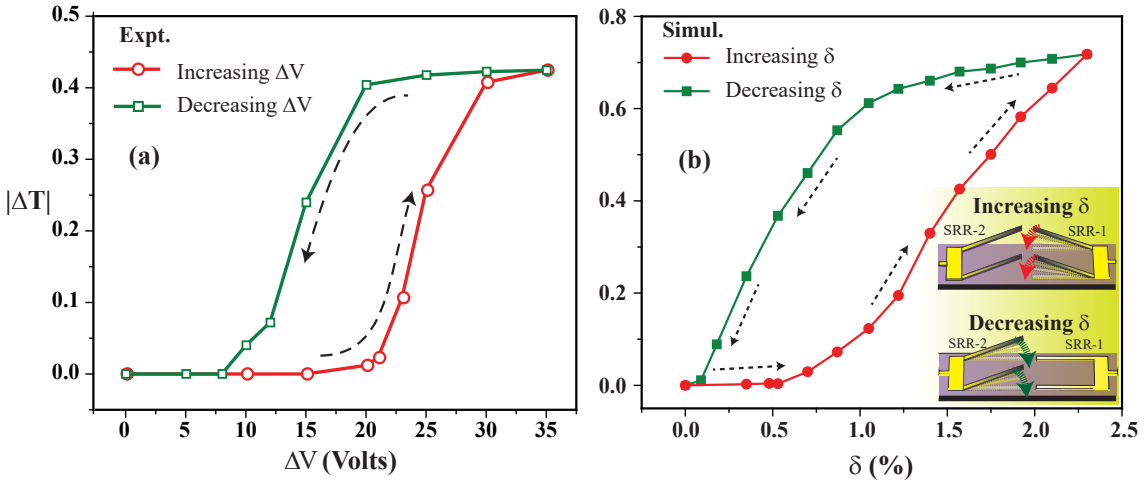


Figure 5.4: (a) Plot showing the measured Fano resonance transmission intensity ($|\Delta T|$) for the two input states of the voltages, $V_1$ on SRR-1 with $V_2 = 0$ V (shown by red circles) and $V_2$ on SRR-2 with $V_1 = 30$ V (shown by green squares) signifying the MIO states and the meta-hysteresis behavior. (b) Simulated Fano resonance intensity ($|\Delta T|$) showing the meta-hysteresis with respect to the structural asymmetry ($\delta$) between the two SRRs. The inset figure in (b) represents the sequential actuation of SRR-1 and SRR-2 that governs the hysteresis-type behavior observed in $|\Delta T|$.

The meta-hysteretic behaviour in the transmitted Fano intensity is purely enacted

by the exponentially extended spatial distribution of near field along the $z$-axis of the metamaterial surface, which shows stronger field strengths closer to the surface and becomes weaker once the resonators are moved away from the substrate. By independently actuating the SRR-1 and SRR-2 structures, we achieve asymmetric coupling between the resonators that shows contrasting coupling strengths depending on whether the fixed resonator is closer to or far away from the substrate. During the increasing $\delta$ configuration, the fixed resonator (SRR-1) is positioned away from the substrate and due to the weak spatial field distribution surrounding the resonator arm, it requires larger asymmetries (higher excitation threshold) to excite the Fano resonance. While decreasing the asymmetry, the SRR-2 positioned on the substrate is likely to have a greater influence the strong near field coupling occurring in the asymmetric structure and results in stronger Fano intensities. Due to this anisotropic nature of near field coupling, variation in the intensity of the Fano resonance follows different paths, which makes a closed hysteresis loop for one complete cycle of the asymmetry parameter ($\delta$). For decreasing $\delta$ configuration, Fano excitation possesses a low excitation threshold as both the resonator structures are closer to the substrate revealing the strong near-field regime of the asymmetric coupling. In Fig.5.4(b), the $|\Delta T|$ of Fano resonance obtained from our numerical simulations is plotted against the change in the asymmetry parameter ($\delta$) of the structure, which shows a likewise meta-hysteretic behaviour (MIO states) as observed in our experiments. For instance, at $\delta = 0.5$ % the calculated values of $|\Delta T|$ are 0.0034 and 0.3675, respectively for the pathways when the asymmetry is gradually increased and decreased in the structure. Shape of the hysteresis loop for $|\Delta T|$ observed in the measurements and the simulations are seen deviating from each other. This is because of the existing nonlinear relation between the applied voltages ($V_1$ and $V_2$) and the actuation heights ($h_1$ and $h_2$) of the MEMS microcantilevers, which is not considered in our numerical simulations.

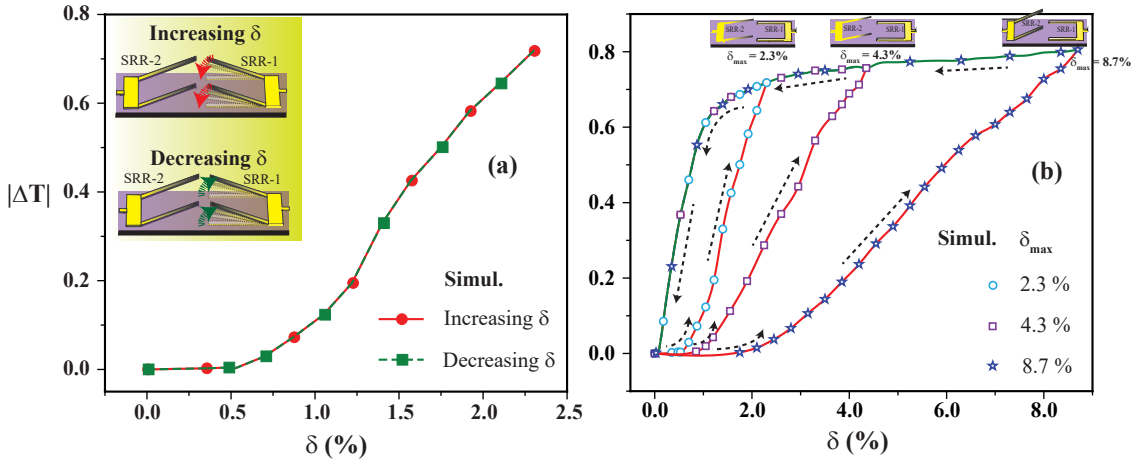


Figure 5.5: (c) Variation in $|\Delta T|$ of Fano resonance for increasing and decreasing $\delta$ configuration, when only SRR-1 actuated by keeping the height of SRR-2 cantilever fixed showing the SIO characteristics in the device. (d) Showing the tuneabilty feature of meta-hysteresis loop in the intensity variation of the Fano resonance with respect to the asymmetry parameter ($\delta$) obtained by the numerical simulations. Black dashed arrows signify the direction of change in the structural asymmetry ($\delta$) parameter.

The continuous and sequential actuation of the adjacent resonators plays a critical role in observed anisotropic excitation of Fano resonances that illustrates meta-hysteresis. To verify this, we performed simulations just by increasing and decreasing the height ($h_1$) of one of the resonators (SRR-1) while keeping the height of SRR-2 fixed. This configuration of varying the asymmetry ($\delta$) fails to show the hysteresis type characteristics in the Fano excitation, which is due to the isotropic nature of coupling between the resonators during the increasing and decreasing pathways of asymmetry, as shown in Fig. 5.5(a). Hence, with the flexibility of tuning the asymmetry of the structure to achieve either isotropic or anisotropic coupling mechanisms in the excitation of Fano resonances, favors this design for many practical applications that can switch between normal and meta-hysteretic state in their optical properties with respect to the asymmetry parameter ($\delta$), just by coding the electrical signalling sequence. Here, we would like to comment that the observed metamaterial induced hysteresis is different from the hysteresis phenomenon observed in the natural materials in the physics of its occurrence. Nevertheless, the aspect of precise engineering

and switching between the normal state to the hysteretic-type state and vice versa is unique to the observed meta-hysteresis in comparison with the all existing natural materials.

Further, the numerical simulations were employed to show that the proposed design can even realize tunable hysteresis loops for $|\Delta T|$, which can be gradually controlled by choosing the maximum attainable asymmetry (that also corresponds to maximum released height ($h$)) in the system, as shown in the Fig. 5.5(b). Area under the observed $|\Delta T|$ hysteresis type loop quantifies the amount of near field energy being dissipated in the system and can be adequately tuned by scanning the asymmetry from the zero state to the maximum asymmetry state ($\delta_{max}$) in the system that is dictated by the maximum inclination height ($h_{max}$) of the resonators. While increasing the asymmetry, variation in the Fano intensity ($|\Delta T|$) follow different pathways for the systems that is dictated by their maximum attainable asymmetry state $\delta_{max}$ = 2.3 %, 4.35 % and 8.7 % for the structures shown in Fig. 5.5(b). On the other hand, when the asymmetry in the system is lowered, the variation in $|\Delta T|$ gradually reduces and follows the same path for the systems with different $\delta_{max}$. The credibility of the proposed Fano design exhibiting the tunable hysteresis loops could have prospective applications in the MM based tunable memory devices at room temperatures with an additional advantage of precise management over the energy dissipative losses in the device.

As we further probe into the optical characteristics of the Fano feature, the meta-hysteretic (or MIO) nature is also seen in the numerically calculated confined electric fields in the resonators' gap at Fano resonance frequency, as shown in Fig. 5.6(a). Variation in the electric field strength takes different trajectories signifying the contrasting field strengths for the same asymmetry parameter ($\delta$), when increased from $\delta$ = 0 to 2.3 % and decreased back to $\delta$ = 0. Such MIO states in the near-field characteristics reveal the NAND logic operation in the form of confined electric fields

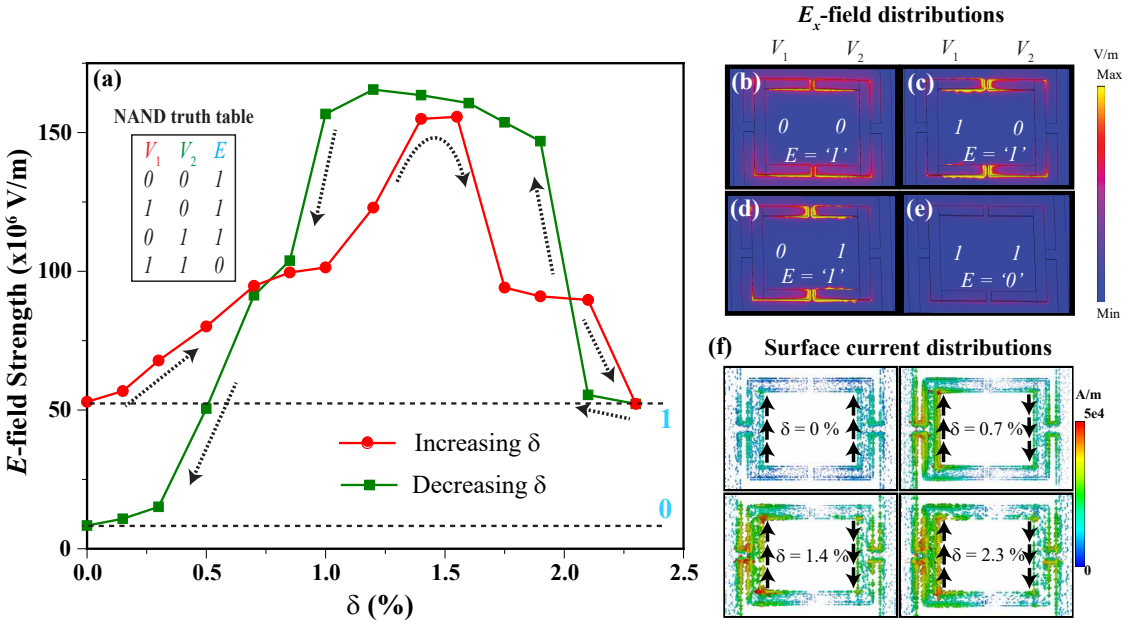


Figure 5.6: (a) Distinctive pathways shown for the enhanced spatial electric field strengths in the MM system at the Fano resonance during increasing and decreasing asymmetry configuration of the system showing the MIO states. (b)-(e) Numerically calculated electric field distributions showing the NAND logical states on the strength of confined fields, where the confinement is maximum (E = 1) for (b), (c) and (d) structural states and minimum for (E = 0) (e) structural configuration. The constructed truth table for NAND feature of the structure is shown in inset of (a). (f) Simulated surface current distributions at the Fano resonance frequency for increasing values of asymmetry, where the surface currents show signatures of circular closed loop currents in the asymmetric resonator cases, which is an evidence of excitation of Fano resonance in the system.

in their ON (snapped) and OFF (released) states. Numerically calculated electric field distributions for various structural states of the MEMS Fano-metasurface are plotted in Fig. 5.6(b-e). The absolute E-field amplitude for structural configurations shown in (b), (c) and (d) represents enhanced field strengths when at least one of the structural states is in released (OFF) state compared to structural configuration (shown in (e)), where both cantilevers are prepared in snapped (ON) states. By choosing the threshold for the electric confinement, we can digitize the near field response for the meta-stable structural states of the sample. Higher amplitude value of the electric field confinement is labeled as binary '1', whereas lower electric field

amplitude is represented by binary '0'. The 'up' and 'down' structural states of SRRs in the structure are labeled as binary '0' and binary '1', respectively. Thus given the structural configurations of (0,0), (1,0), (0,1) and (1,1), the measured strength in the confined E-field constitutes the NAND logic functionality, as described by the truth table in the inset of Fig. 5.6(a). The observed meta-hysteresis (MIO) behavior of the spatially confined near fields in the proposed structure could also show direct implications in all optical switches and near field based memory effects in the subwavelength MM resonator systems. Fig. 5.6(f) shows the numerically simulated surface current distribution for increasing values of the asymmetry of the structure seen at the Fano resonance frequency. For $\delta = 0$, the symmetric surface currents flow through the structure showing the dipole nature of the resonance. Upon introducing an asymmetry ($\delta$) in the structure, electric charges starts to build up in the gaps due to the closed circular currents flowing through the resonator system in Fig. 5.6(f) for $\delta = 0.7$, 1.4 and 2.3 %. Formation of circular currents on the structures signifies the excitation of Fano resonance and results in the strong confinement of the E-fields in the gaps of the resonators. The proposed MEMS design provides a unique control over the modulation of electric field distribution in all three spatial directions of the sample allowing actively tunable mode volumes for the confined fields.

## 5.5 Exclusive-OR (XOR) Metamaterial and its applications in One-time pad cryptographic communication

The versatility of the proposed MEMS Fano-MM device with two input controls and the two output (MIO) states realizes an "$exclusive - OR$" (XOR) logical operation using two electrical controls and an optical readout in the form of absence (false)

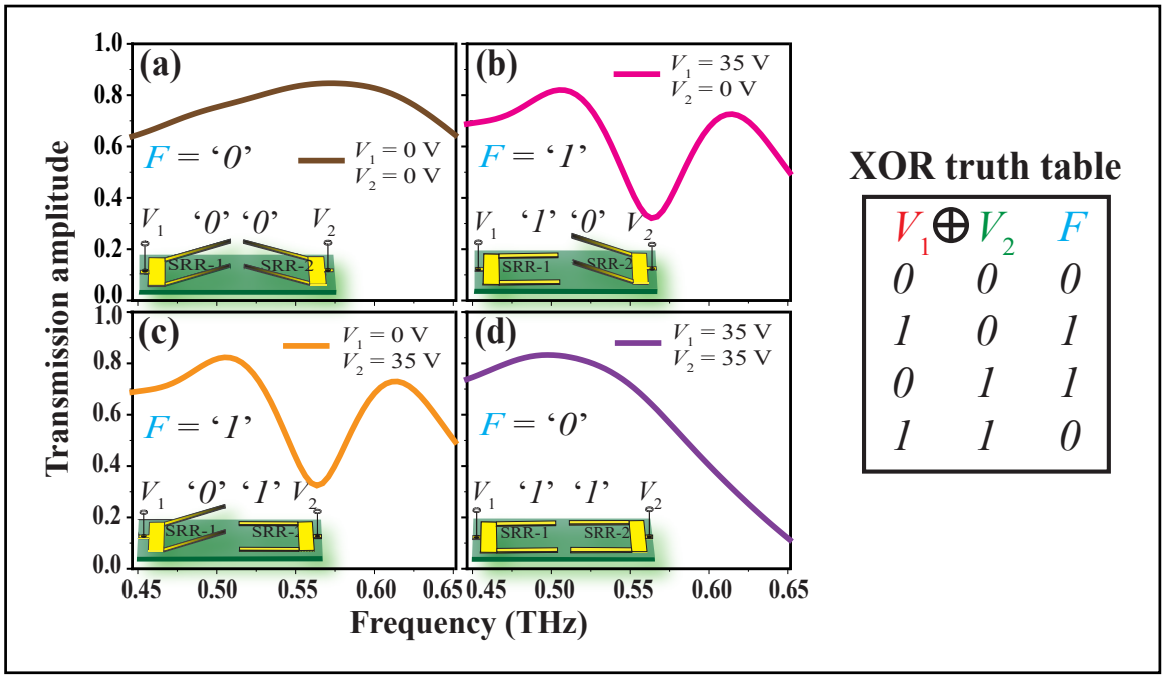


Figure 5.7: (a) Measured THz transmission curves for the symmetric/asymmetric structural meta-stable states of MEMS Fano-MM, respectively showing the absence/presence of Fano excitation near 0.57 THz, which constructs the XOR logic states in its electro-optical characteristics. The inset table shows the derived truth table for the electro-optical response of MEMS Fano -MM, which signifies the XOR logic operation at THz frequencies.

or presence (true) of Fano resonance feature in the metadevice. The structural configurations of the MEMS Fano-MM device that exhibit the XOR logical operation are shown in the insets of Fig. 5.8, where the 'up' state of the metamolecules represents binary '0' and the 'down' state is marked by binary '1'. The optical output state ($F$) of the device is defined by binary bits ('0' and '1') that mimic the absence (false) and presence (true) of Fano resonance feature in the MEMS Fano-MM device, respectively. The structural states of constituent resonators SRR-1 and SRR-2 are labelled as states '$V_1$' and '$V_2$', which can be independently reconfigured using the voltage inputs $V_1$ and $V_2$ in defining the output state of the MEMS Fano-MM. Since, the Fano resonance feature results due to the structural asymmetry, there exists two asymmetric structural configurations 'up-down' (0,1) and 'down-up' (1,0) that results in the true state for the Fano resonance condition (i.e. $F = 1$), as

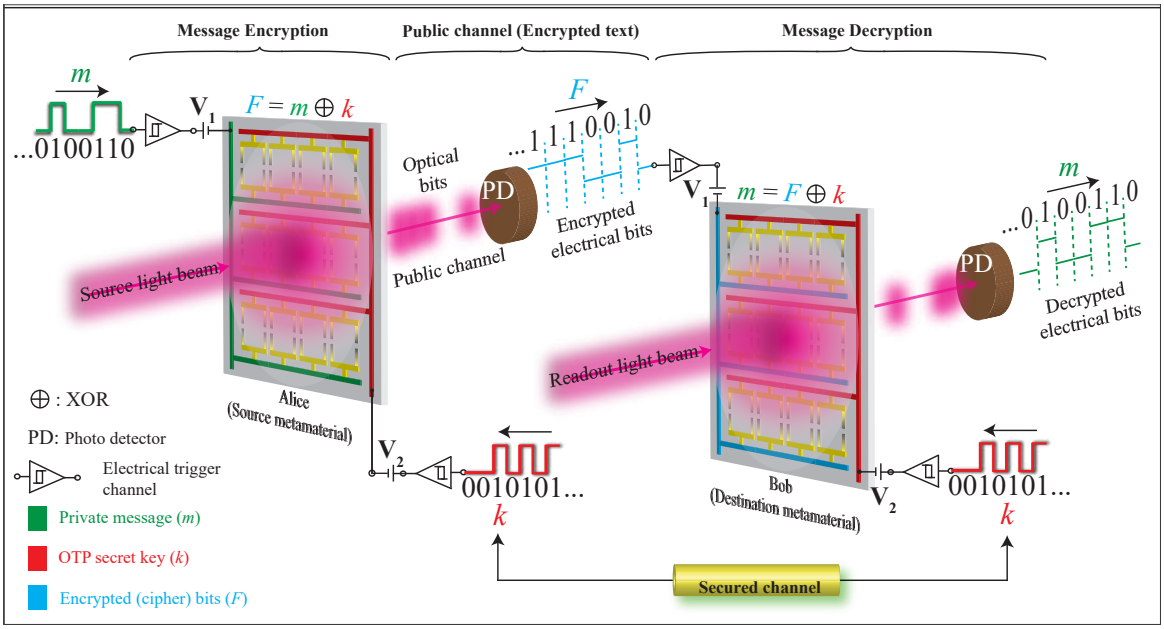


Figure 5.8: Depicts the schematic of MEMS Fano-MM based one-time pad (OTP) cryptographic channel. $m$ = (0100110) is the private message in the form of SRR-1 states encoded in the source place $k$ = (1010100) is the secrete key secured in the from of state of SRR-2. The encrypted message (F = 1110010) is sent through the public channel as the optical states in the form of presence/absence of Fano feature

shown by the transmission response in Figs. 5.7(b) and (c). On the other hand, for the symmetric structural configurations of the device 'up-up' (0,0) and 'down-down' (1,1) results in the $F = 0$ state for the optical Fano resonance, as shown in Fig. 5.7(a) and (d). Thus, digitizing the optical excitation of Fano resonance by independently reconfiguring the structural states of the metamolecules exhibits XOR logical operation given by the truth table in inset of Fig. 5.7. This XOR operation possesses the possible applications in digital/programmable metamaterials, random number generators and in communication systems as secured one-time pad (OTP)[120] cryptographic encrypting/decrypting sequences in secured data transmission channel at sub-terahertz frequencies.

In Fig. 5.8(b), we provide a schematic of the proposed secured OTP cryptographic channel that can be achieved by performing the exclusive-OR (XOR) logical operations in the MEMS Fano-MM. The inputs (private message) $m = 0,1^n$ and (secret

key) $k = 0{,}1^n$ are expressed as the strings of binary digits representing the structural states of resonators SRR-1 ($V_1$) and SRR-2 ($V_2$), respectively and optical readout pulses are represented by $F$ signifies absence (binary '0') or presence (binary '1') of Fano resonance in the metadevice. At the source (Alice's end), for each bits of $m$ = (0100110) and $k$ = (1010100), a XOR operation ($F = m \bigoplus k$) is performed by scanning the terahertz beam through the metadevice that encrypts the message as an optical output state, $F$ (1110010), which is sent as a cipher text (encrypted message) through the unsecured public channel in the form optical signal bits. At the message destination (Bob's end), the optical bits are detected using a photo-detector (PD) and the resulting voltage states ($F$ = 1110010) of the PD are directly fed through a trigger channel to the voltage source $V_1$ that controls the actuation states {0,1} of SRR-1. Finally, the cipher text containing the private message is decrypted by performing the inverse XOR operation, $m = F \bigoplus k$, where $k$ is the secret key (string of random binary digits) that contains the information on the structural state of SRR-2 is exchanged between the source and the destination via a private channel. The inverse XOR operation is executed by performing the terahertz spectroscopy (optical readout) on MEMS metamaterial possessing the structural states defined by the sequential trigger bits of cipher text ($F$) and the secret key ($k$). As the last step, the transmitted optical bits in the form of Fano intensity states are detected by a photo-detector and the private message ($m$) is securely recovered in the form of stream of electrical bits at the message destination. Thereby, by independently reconfiguring the structural state of SRR-1 and SRR-2 using electrically triggered input voltages $V_1$ and $V_2$, a secured information channel is established by encoding and decoding the message in the form of transmitted optical response through the MEMS metamaterial structure. These results provide proof-of-concept study in manifesting the metamaterial based unbreakable one-time pad cryptographic channel that can be efficiently employed in $i$-banking services, super-encryption techniques, random key

distribution and high speed wireless communication channel that is now being pushed towards sub-terahertz bandwidths[6]. The MIO configuration benefits the concept of coding and programmable metamaterials[121, 122] across the far-infrared and optical frequencies for executing complex mathematical operations by expressing the MIO response states of the MM in terms of binary numbers.

## 5.6 Conclusions

The third dimension ($z$-axis) in planar MEMS based MMs is opened up to probe the effects of aerially extended near fields on the Fano-resonance features by independently actuating the SRR resonators within the metamolecule using two voltage controls. The results showed multiple-input-output (MIO) states signifying the meta-hysteretic characteristics in the resonance transmitted intensity and the near field energy of the observed Fano feature with respect to the structural asymmetry parameter/applied voltages. The meta-hysteresis results from the anisotropic near field coupling for the same asymmetric states in the vicinity of nonlinear spatial distribution of the near fields extended in the out-of-plane axis of the MM. Further, with th eproper choice of input sequence, switching of the MM between normal state and hysteretic state was shown, which aids in accurate control of the energy dissipation processes in the system with an added advantage of tunable degree of meta-hysteresis. These results facilitate MEMS Fano-MM based XOR and NAND logical operations in the far- and near-field electro-optical charecteristics of the device. The XOR functionality of MEMS Fano-MM could find potential application as one time pad (OTP) encryption channel that is extremely hard to break without a proper secured key. These results provide proof-of-concept study in manifesting a MM based unbreakable one-time pad cryptographic device that can be efficiently employed in i-banking services, super-encryption techniques, random key distribution and high speed wireless communication channels. The

independent controls in the unit cell of the device leading to MIO characteristics can lay a stepping platform for realizing extremely versatile MMs with optical properties on demand[123]. Further, active reconfiguration of Fano resonances can enable the real time control functionalities of the proposed device in achieving active sensors, nonlinear devices and near field based tunable memory devices operating at room temperatures over the wide region of electromagnetic spectrum.

# Chapter 6

# Localized Plasmon-Phonon interactions in a Semiconductor-Metamaterial hybrid device

## 6.1 Introduction: Semiconductor-Metamaterial hybrid devices

Semiconductor-metamaterial hybrid systems offer a new platform for probing various aspects of resonant and non-resonant light-matter interactions. The nonresonant photoresponsive properties of the semiconductor material such as photoconductivity and ultrafast relaxation of photocarriers provide a flexibility to dynamically control[95] the resonance features of the MMs that has enhanced the real world applications of the devices. In the past, several works have shown the photoactive control of the MM resonances using the dynamic semiconductor materials such as gallium arsanide (GaAs)[55, 54], silicon (Si)[56, 45], graphene[124], and several other 2-D materials

have shown the electrically/optical controlled tuning of MM resonances. However, the switching time of these devices is majorly limited by the relaxation of the photocarriers in the semiconductor materials, which is $> 1$ ns in most of these materials. They also involve defect free lattice matched epitaxial growth of materials that makes an expensive and several steps fabrication processes. In this chapter, new generation semiconducting materials such as solution processed organic-inorganic lead halide perovskite ($CH_3NH_3PbI_3$)[125, 126] and the solution processed lead iodide ($PbI_2$) thin film[127] are spin coated on the MM resonators possessing asymmetric split ring resonators (ASRR)to actively control the strong Fano resonance feature supported by the structure. These designs enable easy and low cost fabrication of the device with additional features of low threshold optical switching and ultrafast modulation. Solution processed semiconductors have shown promising applications and have attracted intense research activities across the globe for their excellent optoelectronic properties combining with their low processing costs. Further to emphasize, the solution processed semiconductor based active design requires simple spin coating technique that is extremely easy process of integrating active substance to the MM, unlike the epitaxially grown silicon on sapphire substrate that requires a tedious fabrication process with the essence of lattice matching. More importantly, the solution processed thin films with considerable lattice/surface defects in the system can act as efficient photo-active material at THz frequencies compared with the defect free and epitaxially grown substrates such as SoS and GaAs. These devices can be of great deal of interest in many real world applications such as ultrasensitive switching and active energy harvesting devices. Blending the unprecedented optoelectronic properties of the solution processed semiconductors and the unnatural MMs can provide an exciting new pathway for exploring entirely new physics[128] and enhanced resonance characteristics in the hybrid semiconductor-metamaterial system.

Resonant interactions in the semiconductor-metamaterial hybrid system involv-

ing strong plasmonic resonances of metamaterial and the vibrational, phononic and excitonic resonances in semiconductor material can lead to new quasiparticles formation. Recent studies have revealed strong plasmon-phonon coupling in a hybrid monolayer $WS_2$-gold nanoparticles[129], graphene layers[130], polycyclic aromatic hydrocarbons[131] and in nanoscale metamaterials[132]. Recently, plasmon-exciton-polariton quasi-particle formation in plasmonic array of silver nanoparticles coated with PMMA doped dye molecules has shown to exhibit low-threshold lasing characteristics at visible frequencies[133]. In the following sections, the design, fabrication and the THz characterization of the $CH_3NH_3PbI_3$ perovskite-metamaterial and $PbI_2$-metamaterial hybrid device. In the later sections, the ultrafast modulations of metamaterial resonances and the localized plasmon-phonon coupling are discussed in perspective of radiant-subradiant Fano interference mechanisms in the hybrid system. part of the results presented in this chapter are published in [114, 134].

## 6.2 Design and Fabrication

To elucidate the properties of the hybrid solution processed semiconductor-MM system, a three layer configuration of the device is considered , where the the $CH_3NH_3PbI_3$ perovskite/$PbI_2$ thin films are spin coated over the MM resonators fabricated on a $z$-cut quartz substrate. Design and unit cell dimensions of the hybrid device is depicted in Fig. 6.1, where the device consists of three layers of materials that includes a 1 mm thick quartz substrate, a metamaterial structure and a thin layer solution processed spin coated semiconductor. The MM resonator design consists of asymmetric split ring resonators (ASRR) possessing the effective structural asymmetry of $r = 15$ $\mu$m that supports the Fano-type of absorption resonance feature. The optical microscope (OM) images shown in Figs. 6.1 (b-d) represent the MM structure without and with the spin coating of the solution processed $CH_3NH_3PbI_3$ perovskite and $PbI_2$ thin film

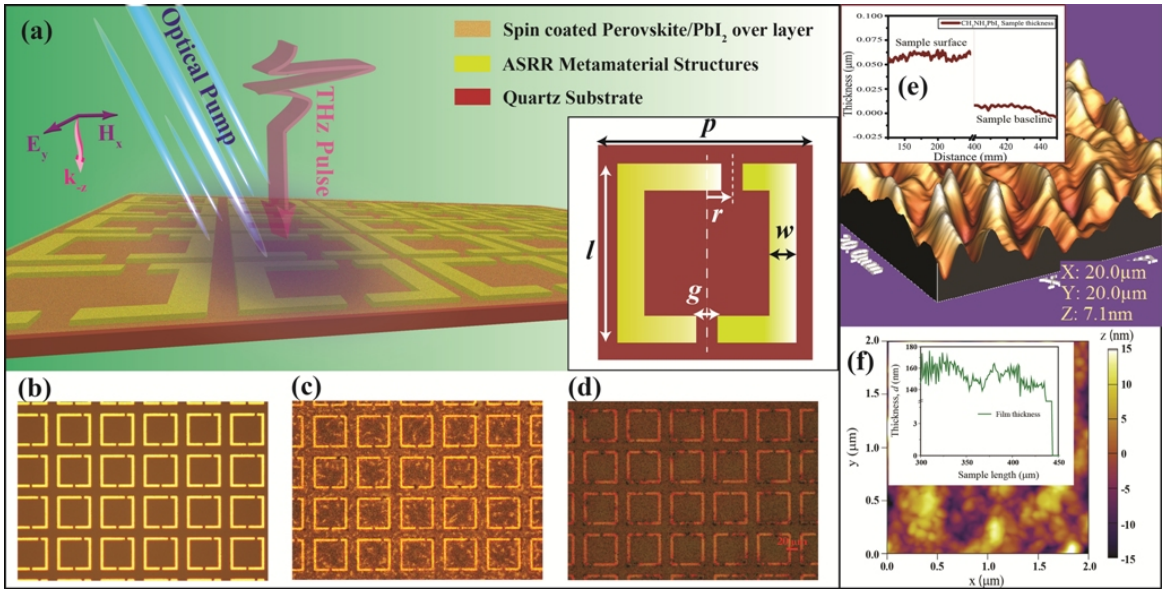


Figure 6.1: (a) Schematic and the unit cell representation of the ASRR Fano-MM device spin coated with the solution processed perovskite and lead iodide thin films. The unit cell comprises of two ASRRs of length $l = 60$ $\mu$m; width, $w = 6$ $\mu$m ; gap, $g = 4$ $\mu$m ; asymmetry $r = 15$ $\mu$m; metal thickness of $t = 200$ nm and periodicity, $p = 75$ $\mu$m. (b-d) Optical microscopy images of the MM structure (a) without spin coating, (b) with perovskite spin coating and (c) with $PbI_2$ spin coating. (e) and (f) are the AFM images of $CH_3NH_3PbI_3$ and $PbI_2$ thin film samples, respectively showing the measured thickness of the thin films.

samples. Thickness of the spin coated $CH_3NH_3PbI_3$ perovskite sample is $d_{Prv} = 60$ nm (Fig. 6.1(e)), whereas the $PbI_2$ thin films samples of two different thicknesses $d_{PbI2} = 160$ nm (Fig. 6.1(f)) and 340 nm are considered.

Metamaterial fabrication on the $z$-cut quartz substrate was performed using the photolithography process described in Chap. 1.4. Further the perovskite ($CH_3NH_3PbI_3$) solution was prepared by using a standard and adequate process based on magnetic stirring, where 78.3 mg/ml lead(II) iodide (Acros Organics $PbI_2$) and 27.0 mg/ml methylammonium iodide (DyeSol CH3NH3I) was dissolved in N,N-Dimethylformamide (Sigma Aldrich DMF) in a $N_2$-filled glovebox to obtain a clear yellow 10 wt. % methylammonium lead iodide ($CH_3NH_3PbI_3$) solution of thickness $d_{Prv} = 60$ nm. Whereas, the lead iodide ($PbI_2$) thin film sample was prepared using the conventional solution-based fabrication protocol. The 500 mg/ml ($d_{PbI2} = 160$ nm) and 1000 mg/ml

($d_{PbI2}$ = 340 nm) $PbI_2$ (purchased from Acros Organics) were mixed in anhydrous DMF (Sigma Aldrich, 99.9%) and stirred at 70°C for two hours. Later, the solution processed thin film samples were spin coated on the ASRR MM and quartz substrate at 4000 RPM for 30 seconds to form a thin over layer film. In the case of $PbI_2$ spin coating, the $PbI_2$ were filtered with 0.45 $\mu$m polytetrafluoroethylene (PTFE) filter before spin coating and solvent engineering of the $PbI_2$ films was performed by dripping 100 $\mu$l toluene, 5 seconds after start of the spin-coating. Samples were subsequently annealed at 100°C for 30 minutes. All the sample preparation and processing steps were performed in $N_2$ filled glovebox. Atomic Force Microscopy (AFM) image of the spin-coated $CH_3NH_3PbI_3$ perovskite and $PbI_2$ thin film samples shown in the Figs. 6.1(e) and (f) were obtained using the Asylum Research MFP-3D AFM system in the tapping mode. Thickness of the spin coated $CH_3NH_3PbI_3$ and $PbI_2$ thin film sample were estimated using the surface profilometry measurements (shown in the inset of Fig. 6.1(e) and (f)). The spin coating method of depositing the solution processed semiconductor on the photonic/MM device can be compatible on much more complex MM structures. For example, they can be spin coated onto the metamaterial patterned on the flexible substrates, multilayered metamaterial structures, hyperbolic metamaterials and various other photonic devices. The spin coating of perovskite also depends on the choice of the substrates such as silicon, indium tin oxide coated glass, polyethylene terephthalate (PET) etc. It is also possible to scale-up applications using screen printing and doctor blade techniques.

## 6.3 Photoactive and Ultrafast modulation of Fano resonance in a metamaterials

Intergrating the dynamic semiconducting material with the metamaterial structure have given a useful way of actively modulating the resonance features in the meta-

material structures. The most common techique is used is the photo-excitation of the semiconducting materials using the pump with a pump of photon energy greater than the energy bandgap of the semiconducting materials. Photodoping increases the free carrier density in the semiconducting materials, there by making them a semi-metal with high conductivity. This change in condutivity in the semiconductors will damp the resonance properties of the metamaterial structures, there by showing the active modulation of metamaterial resonsnces. Whilest there exists many works in this direction, but there remains a strrong quest for realizing ultrasensitive and ultrafast active metamaterial devices for high speed and practicle applications. In this section, we probe and demonstrate photo-active tuning of Fano resonances in metamaterial structres using three teype of semiconduting materials such as silion, solutuion processed hybrid lead halide perovskite ($CH_3NH_3PbI_3$) and solution processed lead iodide ($PbI_2$) thin films. Optical and active response of the hybrid devices were characterized using the optical pump-terahertz probe (OPTP) technique described in Chap. 1.1.2. An ultrafast optical pump pulse of wavelength 800nm (for silicon) and 400 nm (for $CH_3NH_3PbI_3$ and $PbI_2$) are used to optically excite the semiconductor+MM samples and the excitation and relaxation dynamics of the photoexcited carriers are probed using the THz pulse. Energy of the respective optical pump pulses ($E$ = 1.56 eV (800nm) and 3.1 eV (400nm)) are greater than the energy band gap of the silicon and solution processed $CH_3NH_3PbI_3$ perovskite ($E_g$ = 1.55 eV) and $PbI_2$ ($E_g$ = 2.2 eV) thin film samples. The beam spot size of the optical pump for silicon (800 nm) is apprx. 10 mm, whereas for 400 nm is aprox. 5 mm, which is larger than the spot size of THz beam that is 3 mm. Fig. 6.2(a) represents the THz transmission through the silicon+MM sample for varying pump powers of 800 nm excitation beam. The sample consicts of the metamaterial sample deposited on a structured epitaxial grown silicon-on-sapphire (SoS) substrate using the two step photolithograhy process. The details on the design[114] and fabrication are given in section 1.4. As the 800 nm

pump is used to photoexcite the silicon patches in the material, the amplitudes of the Fano (0.6 THz) and the dipole resonances (0.8 THz) gradually modulated (decreased) with the increasing pump power. For the pump power of 40 mW, the Fano feature complete diminishes in the system giving rise to broad dipole resonance. This low power switching demonstrates a sensitive nature of the Fano resonance (high field confinement) to the external perturbation. The switching speed of this resonance is limited by the electronic life-lime of the silicon , which fall in the range of micro-milli seconds (slow relaxation process of silicon is shown in the inset of Fig. 6.2(a)). However, choosing the material with ultrafast electronic relaxation processes helps in achieving the ultrafast switchable metamaterial devices at THz frequencies. The solution processed semiconductors ($CH_3NH_3PbI_3$ and $PbI_2$) with the easy spin coating techniques make them good candidates to realize facile and ultrafast metamaterial based devices at THz frequencies for high-speed device applications.

Fig.6.2(b) represents the THz transmission through the photoexcited perovskite-metamaterial sample for varying fluence of pump beam. For the sample without perovskite over layer, the transmission spectrum results in the mode splitting behaviour with the Fano resonance feature at the lower frequency (0.75 THz) and the dipolar resonance at 1.1 THz. This results in the Fano type of interference mechanisms triggered by the asymmetry of the ASRR MM structure. By spin coating the $CH_3NH_3PbI_3$ perovskite thin film of the ASRR MM, the Fano resonance observes a strong modulation and red shift in its resonance frequency. Thereafter, by shining the pump beam (400 nm) with increasing fluence, strength of the Fano resonance shows gradual modulation. For the fluence of 10.5 $\mu J/cm^2$ the resonance shows strong modulation and increase in the resonance line width. This is a signature of the weak phonon-Fano coupling that will be discussed in the later sections. Therefore, the resonance does not see complete modulation rather it undergoes mode splitting behaviour as shown in Fig. 6.3 . The compelling feature of the system is that the

modulation shows low threshold switching compared to other photoactive MM devices at THz frequencies. However, the switching speed of the modulation stays in the range of few ns (shown in inset of Fig. 6.2(b)) that is comparable to the GaAs based active MM devices [54].

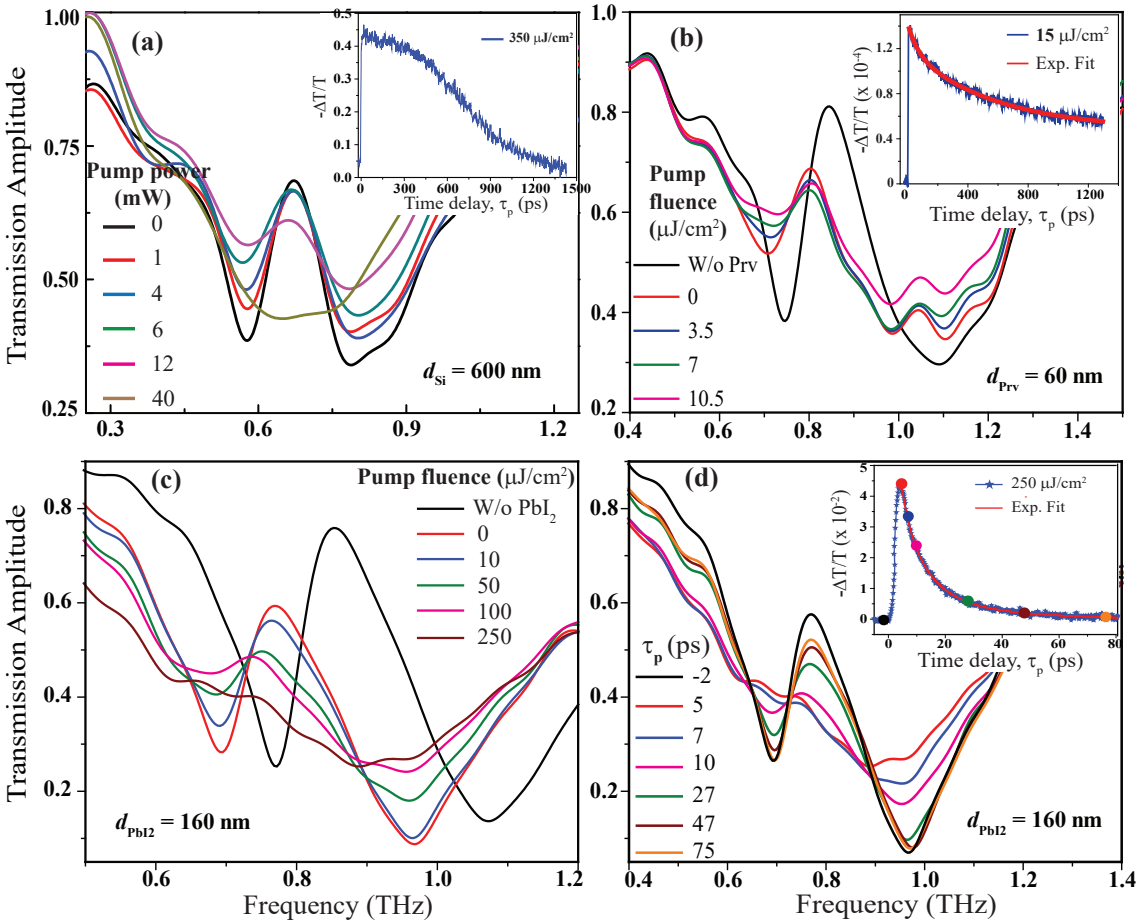


Figure 6.2: (a) Measured THz transmission through the photoexcited silicon implanted metamaterial structure showing pump-power dependent modulation of Fano resonance . The inset figure shows the relaxation of photoexcited carriers in the 600 nm thin silicon-on-sapphire substrate. (b) Measured THz transmission spectrum through the $CH_3NH_3PbI_3$-MM sample for varying pump fluences. Inset figure represents the differential THz transmission response showing the relaxation dynamics of the photoexcited $CH_3NH_3PbI_3$ perovskite sample. (c) Measured THz transmission spectrum of the $PbI_2$-metamaterial sample for varying pump fluences. (d) THz transmission spectrum showing the ultrafast modulation of the Fano resonance feature measured at varying pump-probe time delay. Inset diagram represents the ultrafast relaxation dynamics of the photoexcited carriers in the $PbI_2$ thin film sample.

Fig. 6.2 (c) represents the pump fluence induced variation in the transmission spectrum through the $PbI_2$-MM sample (thickness of $PbI_2$ = 160 nm), where the strength of Fano resonance shows gradual decrease at higher pump fluences as seen for the $CH_3NH_3PbI_3$-MM sample. The fluence required for the modulation is higher than the $CH_3NH_3PbI_3$ perovskite sample because of the low photoconductivity of the $PbI_2$ thin film at THz frequencies. However, the $PbI_2$-MM sample shows near unity modulation of the Fano resonance for the pump fluence of 250 $\mu J/cm^2$. In Fig. 6.2 (d), the ultrafast modulation of Fano resonance feature in the $PbI_2$-MM sample is shown, where the resonance switching is performed within ultrafast time scale of 50 ps. The transmission spectrum was measured in the presence of pump beam (400 nm, fluence = 250 $\mu J/cm^2$) at various pump-probe time delay ($\tau_p$) of the OPTP system that shows ultrafast modulation of the resonance features in $PbI_2$-MM hybrid device. The Fano resonance feature shows complete switch-off after 5 ps of the pump excitation due to the maximum number of photoelectrons in the sample and the resonance is recovered with in 50 ps (shown in inset of Fig. 6.2(d)), as all the photoelectrons recombine and come back to the valance band. In these semiconductor-MM hybrid systems, the life time of the photoexcited carriers in semiconducting material dictates the switching time of the resonator device. Therefore, with ultrafast relaxation of the photoexited carriers in the $PbI_2$ sample along with the easy spin coating process and better stability make it an ideal material and simple technique to realize MM based ultrafast photonic devices at far-infrared frequencies.

## 6.4 Localized plasmon-phonon quasiparticle coupling in $CH_3NH_3PbI_3/PbI_2$-MM hybrid device

Recent studies have confirmed that the low frequency phonon modes that result from the structural (lattice) vibrations[135, 136] of the $PbI_2$ metal-halide (Pb-I) cage play

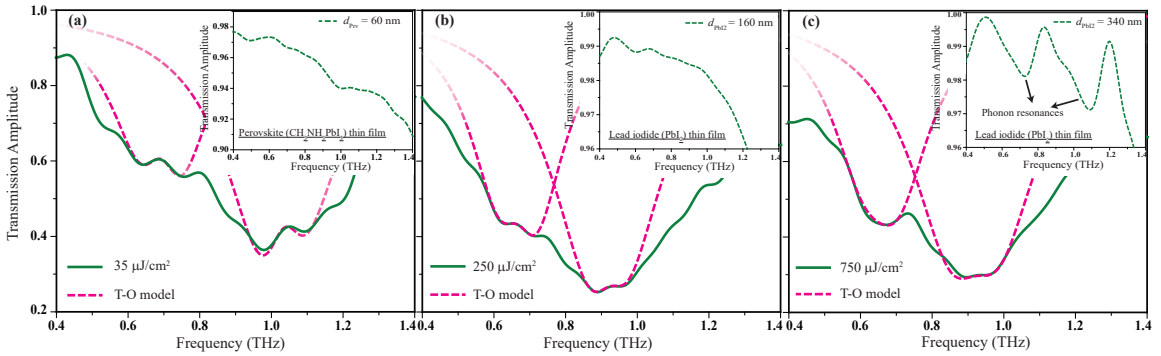


Figure 6.3: Measured THz transmission spectrum of the (a) 60 nm thick $CH_3NH_3PbI_3$ Prv-MM, (b) 160 nm thick $PbI_2$-MM and (c) 340 nm thick $PbI_2$-MM hybrid samples showing the mode splitting and broadening features due to localized plasmon-phonon quasiparticles interaction. Inset figures represent the direct THz transmission spectra showing through the (a) bare $CH_3NH_3PbI_3$ and (b) bare $PbI_2$ thin film showing extremely weak features of phonon resonances, respectively. Whereas, the inset figure in (c) shows the transmission through 340 nm thick bare $PbI_2$ sample highlighting the direct excitation of the phonon modes in the THz transmission response through the thin film sample.

a crucial role in dictating the optoelectronic properties and the charge transporting characteristics of hybrid lead halide perovskites[137]. On the other hand, the resonant phonon-electron coupling in the strong or ultra-strong coupling regime (enhanced cavity finesse) that enhances the coherence by aiding phonon assisted transitions in the system. Therefore, spin coating the perovskite ($CH_3NH_3PbI_3$) and the $PbI_2$ thin films on the metamaterial resonators, it is possible to resonantly sense and couple the phonon modes of these semiconducting material to the plasmonic resonances of the MM structure. This will enable the formation of new localized plasmon-phonon quasiparticles in the lower frequencies that can have great implications on tailoring the resonant energy transfer between the quasiparticles and in controlling the phonon mediated scattering mechanisms in these soft (semiconducting) materials.

In $CH_3NH_3PbI_3$ hybrid perovskite or $PbI_2$ thin films, strength of the low frequency phonon modes that result from the vibrations in the Pb-I cage depends on the temperature and thickness ($d$) of the spin coated thin film. At room temperature, for thinner film ($d_{Prv} = 60$ nm), the thermal fluctuations overshadow the excitation

of the phonon modes in the film and hence there are no visible phonon resonances seen in the transmission spectrum of the $d_{Prv} = 60$ nm thin film $CH_3NH_3PbI_3$ and $d_{PbI2} = 160$ nm thin $PbI_2$ samples as shown in the inset of Fig. 6.3(a) and (b), respectively. However, by spin coating the $CH_3NH_3PbI_3$ ($d_{Prv} = 60$ nm)/$PbI_2$ ($d_{PbI2} = 160$ nm) thin film on the ASRR MM structure, results in a strong enhancement in the strength of the phonon mode due to the energy transfer from the localized plasmons that in-turn resonantly couples to the Fano and dipolar resonance features (plasmonic modes) of ASR MM structure. The resonant localized plasmon-phonon interaction results in the mode splitting behaviour seen in the transmission characteristics of the $CH_3NH_3PbI_3$-MM sample at 0.7 and 1.05 THz frequencies, as shown in Fig. 6.3(a). Similarly, for $PbI_2$-MM sample (where, $d_{PbI2} = 160$ nm), the mode splitting behavior seen in its transmission characteristics at 0.65 and 0.95 THz frequencies, as shown in Fig. 6.3(b). The observed resonance mode splitting is a consequence of the Fano-type of bright-dark mode interactions, where the weak phonon mode (termed as dark mode) in the $CH_3NH_3PbI_3/PbI_2$ sample gets excited by virtue of coupling to the localized plasmons (termed as bright mode) that in turn couples to the weak Fano (low frequency) and the dipolar resonances (high frequency) of ASRR-MM structure. In the case of higher thickness of the $PbI_2$ ($d_{PbI2} = 340$ nm) film, nature of the localized plasmon-phonon interactions possess distinctive characteristics, where we observe a mode splitting in the dipole-phonon resonance coupling, but the Fano-phonon resonance coupling shows a resonance broadening behavior, as shown in Fig. 6.3(c). This change in nature of coupling is attributed to the direct excitation of the phonon modes in the thicker $PbI_2$ film (shown in inset Fig. 6.3(c)) that possess broader resonance line-widths than that for the thinner film. Thus, the Fano-phonon resonance coupling (at 0.65 THz) shown in Fig. 6.3(c) is attributed to the bright-bright type of interactions possessing the comparable resonance line-widths that only favours the constructive superposition of resonances and results in the broadening of the coupled resonance feature. On

the other hand, the dipole-phonon resonance coupling (at 0.9 THz) results in the mode splitting behaviour due to their contrasting resonance line-widths (Fano-type destructive interference) and same resonance frequencies that resembles the bright-dark type of interactions in the system (discussed in previous chapters 2.7 and 4.6).

The resonant localized plasmon-phonon interaction resembling the bright-dark and bright-bright type of mode coupling (interference effects) can be analytically modelled using the two-coupled oscillator model (T-O model) (Chapters 2.7 and 4.6). The resonant interactions in the present semiconductor-MM hybrid system can be described by the following set of equations of motion,

$$\ddot{x}_b(t) + \gamma_b \dot{x}_b + \omega_b^2 x_b(t) + \Omega^2 x_d(t) = \frac{q_b E}{m_b} \tag{6.1}$$

$$\ddot{x}_d(t) + \gamma_d \dot{x}_d + \omega_d^2 x_d(t) + \Omega^2 x_b(t) = \frac{q_d E}{m_d} \tag{6.2}$$

Here, ($x_b$, $x_d$), ($\omega_b$, $\omega_d$) and ($\gamma_b$, $\gamma_d$) are the scattering amplitudes, angular resonance frequencies and the line-widths of the bright and dark modes respectively. $\Omega$ defines the coupling strength between the bright and dark modes. $f_b = \frac{q_b}{m_b}$ and $f_d = \frac{q_d}{m_d}$ quantify the free space coupling strengths of bright and the dark modes with the incident THz light, where ($q_b$, $q_d$) and ($m_b$, $m_d$) are their effective charges and masses, respectively. By defining the charge and mass ratios respectively as $\frac{q_b}{q_d} = A$ and $\frac{m_b}{m_d} = B$, we arrive at the susceptibility expression ($\chi$) by solving for the scattering amplitudes $x_b$ and $x_d$, and is given by,

$$\begin{aligned}\chi = \frac{K}{A^2 B}\Big(&\frac{A(B+1)\Omega^2 + A^2(\omega^2 - \omega_d^2) + B(\omega^2 - \omega_b^2)}{\Omega^4 - (\omega^2 - \omega_b^2 + i\omega\gamma_b)(\omega^2 - \omega_d^2 + i\omega\gamma_d)} \\ &+ i\omega \frac{A^2\gamma_d + B\gamma_b}{\Omega^4 - (\omega^2 - \omega_b^2 + i\omega\gamma_b)(\omega^2 - \omega_d^2 + i\omega\gamma_d)}\Big)\end{aligned} \tag{6.3}$$

The mode split regions in the transmission data shown in Fig. 6.3(a), (b) and

(c) are fitted by the [1-Im($\chi$)] expression that represents the transmission through the medium, where $K$ is the normalizing constant. The individually fitted data shows good agreement with our experimentally measured transmission spectra for the realistic fitted parameters listed in the Table. 6.1. For the Fano-phonon and the dipole-phonon coupling for $CH_3NH_3PbI_3$-MM hybrid sample, the resulting spectral mode splitting is fitted by considering the condition of same resonance frequencies ($f_{fano} = f_{phonon} = 0.67$ THz) and contrasting line-widths ($\gamma_{fano} > 2\gamma_{phonon}$) gives rise to the observed bright-dark mode splitting behaviour, whereas for the dipole-phonon coupling, the resonance conditions are the $f_{dipole} = f_{phonon} = 0.93$ THz and $\gamma_{dipole} \approx 3\gamma_{phonon}$ tat too results in the mode splitting behaviour. More interestingly, the proposed T-O model gives the relative coupling strengths of the dipole, Fano and the phonon resonances to the free space (incident) field that is quantified by the extracted charge and the mass ratios $A$ and $B$, respectively. In the model, the mass of the resonance oscillators are considered to be the same and hence $B = 1$ for all the resonators. The extracted charge ratio ($A$) for the Fano-phonon and dipole-phonon coupling in $CH_3NH_3PbI_3$-MM device are 11 and 250, respectively, which suggests that the free space coupling of the Fano mode is nearly 11 times stronger than that of the weak resonant phonon mode, whereas the coupling of the dipole mode to the free space field is approximately 250 times stronger than that of the resonant phonon mode. Similarly, the analytical fitting is performed for the transmission spectrum of $PbI_2$-MM samples as shown in Fig. 6.3(b) and (c), where for the sample with thinner $PbI_2$ film ($d_{PbI2} = 160$ nm) the similar mode splitting characteristics are observed as seen for the perovskite-MM sample with $\gamma_{fano} \approx 2\gamma_{phonon}$, $\gamma_{dipole} \approx 2.5\gamma_{phonon}$, free space coupling terms $A = 11$ and 35 for Fano and dipole resonances, respectively. On the other hand for the sample with thicker $PbI_2$ film ($d_{PbI2} = 340$ nm) direct excitation of phonon modes in thin film affects the Fano-phonon coupling by broadening the resonance (bright-bright coupling), where the line-widths of both the resonances fall

in same range ($\gamma_{fano} \approx \gamma_{phonon}$). Since the dipole resonance is highly radiative in nature, we still can see a small signature of mode splitting near 0.93 THz for the small difference in their line-widths ($\gamma_{dipole} \approx 1.5\gamma_{phonon}$). The free space coupling constant ($A$) for Fano is 5 times stronger than that of the resonant phonon mode and for dipole it is nearly 25 times greater than the corresponding resonant phonon mode. Here, the point to stress is that the localized plasmon-phonon coupling maximizes in the sample when the strength of the MM (localized plasmonic) resonances is weak at higher pump fluences. This is due to the comparable strengths of the correspondence resonant features (localized plasmons and phonons) to form an efficient coupling between them Therefore, the observed localized plamon-phonon quasi-particle interference can be actively controlled by varying the pump fluences that can enrich the functionality of the proposed device.

| Samples | Quasiparticle coupling | $\omega_b$, $\omega_d$ $\times 10^{12}$ rad/s | $\gamma_b$ $\times 10^{12}$ rad/s | $\gamma_d$ $\times 10^{12}$ rad/sec | $\Omega$ $\times 10^{12}$ rad/s | $A$ |
|---|---|---|---|---|---|---|
| $CH_3NH_3PbI_3$- MM ($d_{Prv}$ = 60 nm) | Fano-phonon | 4.4 | 1.6 | 0.7 | 1.6 | 11 |
| | Dipole-phonon | 6.53 | 2 | 0.7 | 2 | 250 |
| $PbI_2$-MM ($d_{PbI2}$ = 160 nm) | Fano-phonon | 4.25 | 1.5 | 0.8 | 1.5 | 11 |
| | Dipole-phonon | 5.85 | 2 | 1.2 | 2 | 25 |
| $PbI_2$-MM ($d_{PbI2}$ = 340 nm) | Fano-phonon | 4.2 | 1.5 | 1.2 | 1.5 | 5 |
| | Dipole-phonon | 5.85 | 2 | 1.2 | 2 | 25 |

Table 6.1: Theoretically fitted parameters using the coupled two-oscillator (T-O) model (Fig. 6.3(a-c)) that shows a good agreement and accurately describes the interaction mechanisms of the localized plasmons-phonon coupling that leads to the observed resonance broadening and mode-splitting results. The coupling strengths ($\Omega$) between the localized plasmons and the phonon modes are mainly dictated by and nearly equal to the loss-factors of the bright mode that majorly influences the coupling in the system.

## 6.5 Photoactive control of localized plasmon-phonon quasiparticle coupling

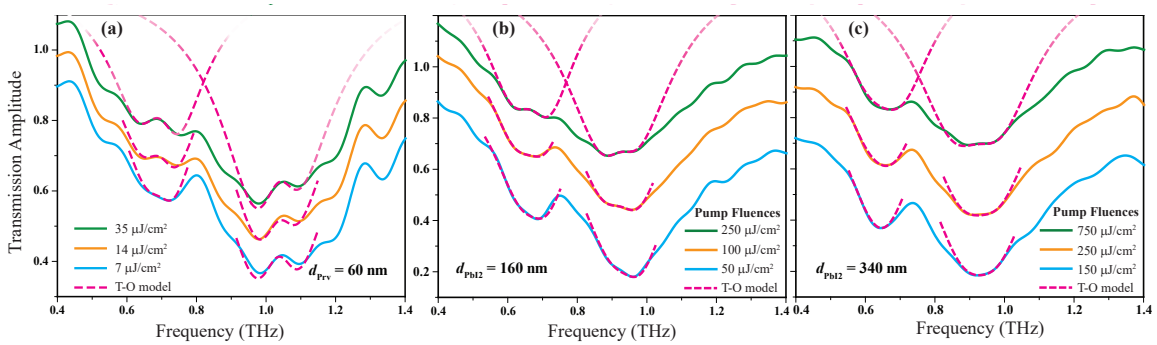


Figure 6.4: Pump fluence dependent THz transmission spectrum of the (a) 60 nm thick $CH_3NH_3PbI_3$ Prv-MM, (b) 160 nm thick $PbI_2$-MM and (c) 340 nm thick $PbI_2$-MM hybrid samples showing the pump dependent mode splitting and broadening features due to modified localized plasmon-phonon quasiparticles interactions.

The dynamic control of localized plasmon-phonon interactions using optical illumination with varying fluences is shown in Fig. 6.4. By increasing the pump fluences, results in a gradual broadening of the coupled resonances and shows a signature of resonance mode splitting at the higher pump fluence of 35 $\mu$m/cm$^2$, 250 $\mu$m/cm$^2$ and 750 $\mu$m/cm$^2$ for 60 nm thick $CH_3NH_3PbI_3$-MM, 160 nm thick $PbI_2$-MM and 340 nm thick $PbI_2$-MM samples, respectively. This observation is further supported by the theoretical T-O model, where the resonance broadening and the mode splitting regions are accurately fitted using [1-Im($\chi$)] of Eqn. 6.3 by changing the coupling strengths ($\Omega$) between the resonance modes and the line widths of the MM resonances, while keeping the remaining system parameters constant, as listed in Table 6.2. Increasing the coupling strengths with respect to the pump fluence highlights that the gradually diminishing Fano and dipolar resonances at higher pump fluences couple strongly with the weak resonant phonon modes resulting in either the resonance broadening or mode splitting nature of the coupled resonances. This result further emphasis the fact that the mode coupling becomes stronger when both the resonant

modes possess comparable resonance intensities otherwise the stronger resonance mode overshadows the influence of the weak resonance in the system. In general, the results show an adequate way to actively control and enhance the localized plasmon-phonon quasi-particles interference mechanisms in a $CH_3NH_3PbI_3/PbI_2$-MM hybrid system that could have larger implications in governing the quasi-particle scattering mechanisms such as electron-phonon and other phonon mediated scatterings in the solution processed semiconductors including the lead metal halide perovskites.

| Samples | Pump fluence $\mu J/cm^2$ | Fano-phonon $\Omega$, $\gamma_b$ ($\times 10^{12}$ rad/s) | Dipole-phonon $\Omega$, $\gamma_b$ ($\times 10^{12}$ rad/s) |
|---|---|---|---|
| $CH_3NH_3PbI_3$-MM ($d_{Prv}$ = 60 nm) | 7 | 1.3 | 2 |
| | 14 | 1.5 | 2 |
| | 35 | 1.6 | 2 |
| $PbI_2$-MM ($d_{PbI2}$ = 160 nm) | 50 | 1.2 | 1.4 |
| | 100 | 1.3 | 1.6 |
| | 250 | 1.5 | 1.7 |
| $PbI_2$-MM ($d_{PbI2}$ = 340 nm) | 150 | 1 | 1.7 |
| | 250 | 1.3 | 1.8 |
| | 750 | 1.5 | 2 |

Table 6.2: Theoretically extracted coupling strengths ($\Omega$) of the localized plasmons-phonon coupling by fitting the transmission spectrum for varying pump fluences using the two-oscillator (T-O) model shown in Fig. 6.4(a-c). While keeping all other resonant parameters constant, the coupling strength ($\Omega$) and loss factor of the bright modes ($\gamma_b$) in the Eqn. 6.3 is varied to fit the spectral region of resonant localized plasmon-phonon coupling for varying pump fluences. Increasing $\Omega$ and $\gamma_b$ numbers for increasing pump powers signify the dynamic tuning of the localized plasmons-phonon coupling by shining an external optical pump pulse in the system.

## 6.6 Conclusion

In this chapter, sensing and elucidation of new localized plasmon-phonon quasiparticle interaction in the THz part of the EM spectrum were probed and discussed. These interactions resemble the Fano-type of interference coupling between the radiant (localized plasmons) and the subradiant (phonon) modes that is analyzed using the two-

coupled oscillator model. The theoretical model revels the resonant energy transfer between the localized plasmons and the phonon resonances possessing contrasting loss factors results in the resonance mode splitting and resonance broadening effects. Such resonant localized plasmon-phonon quasiparticles interaction signify the emergence of new form of quasiparticles that can efficiently couple to the incident THz photons in forming localised plasmon-phonon polaritons at far-infrared frequencies. Further, with a greater significance of phonon mediated scattering in the prominent hybrid perovskite materials that dictate their charge carrier dynamics and efficiency of the device, our results can provide new insights into the understanding the effects of phonon mediated scattering mechanisms in the solution processed lead metal halide perovskites. In addition, the proposed solution processed hybrid perovskite/$PbI_2$-MM device possessing multi-beneficial features offers low cost, stable, ultrasensitive and ultrafast modulation of metamaterial resonances and serves as basis for realizing efficient active subwavelength photonic devices operating at the terahertz and far-infrared frequencies.

# Chapter 7

# Conclusions and Future Directions

Over the years, MMs have offered exciting features and applications in the field of photonics and because of their unique feature of subwavelength nature, they allow to capture and control the near-field excitation in a precise way. These near-fields carry the finest information of the material under the light matter interaction that dies out exponentially within the wavelength distances near the material surface. In the natural materials this finest information of the near-fields is nearly impossible to comprehend and manipulate. Capturing and manipulating such near-fields using MM structures can lead to exciting effects such as perfect lens and super-oscillation concepts, which has been the breakthroughs in the field of optics and photonics. Further, by altering their structural configuration, sharp absorption and the transmission features can be observed that enhance the near-field confinement and aids in strong light-matter interactions. In this thesis, the presented works fall under the umbrella of probing the strong light-matter interactions in MMs in the THz frequency spectrum under various structural geometry and position configurations of the MM device. The studies were performed passively and actively under various structural configuration of the considered MM design.

The works presented in the thesis show great prospects and lay a potential platform

for the new generation MM based photonic devices in the THz part of the EM spectrum. In the initial chapters (Chapts. 1 and 2), strong light matter interactions in a composite MM structure was thoroughly studied that showed sharp transparency effects, slow light phenomenon and resonant invisibility of SRR in the system. Such systems offer potential prospects as the sensors, amplitude modulators, filters, resonant switches and slow light devices for the telecommunication applications in the sub-THz bandwidths. Further, the resonant invisibility effects are shown in the composite MM system (Chap. 3) provides a new invisibility mechanism using MMs that can circumvent the existing limitations of required exciting material properties and need of 3-D structures that hindered the realization of invisibility effects in the THz part of the EM spectrum. These devices also show an active switching between the broad dipolar resonance and sharp LC resonance, thereby providing the flexibility of active control of the loss factors in the resonator systems. Further studying the similar interactions in the complementary design (where the bi-anisotropy in cSRR is absent) of the proposed geometry could provide more insights and new prospective to the observed invisibility effect of SRR in the strong inductive coupling regime. In chapter 4, by choosing a different structural configuration of the MM device and coupling its resonance features with the resonant lattice mode, a strong enhancement in the $Q$-factor and the slow light feature of the transmission resonance are shown. This provides a new mechanism of inducing a sharp transparency window by coupling the radiant (bright) mode with two subradiant (dark) modes that greatly enhances the sharpness of the transmission resonance thereby, resulting in the very steep dispersion within the medium. This phenomenon is termed as lattice induced transparency (LIT) that can be extended to most of the periodic structures to circumvent ohmic losses of the metallic resonators across wide band of EM spectrum.

All the investigations presented in the initial chapters of the thesis were performed by exploiting the in-plane ($x$-$y$ plane) near-field features by altering the structural

configuration in the plane of the MM sample. In chapter 5 of the thesis, properties of the near-fields in the $z$-dimension (out-of plane) of the sample were utilized to demonstrate intriguing phenomena such as meta-hysteresis and complex logic gates in the optical domain of the device operation. The nonlinear exponential decay of the near-fields in the aerial (out-of plane) direction of the sample was cleverly used to demonstrate the anisotropic near-field coupling in the excitation of sharp Fano resonances using two independent input voltage controls on the meta-molecules. This played a critical role in observing multiple input-output states (MIO) that can lay a useful platform for realizing functional and randomly accessible metamaterials by establishing the independent control within the unit-cell of the MM to envisage optical properties[123] on demand with enriched electro-optic performance, which is treated as a next big thing in the MM community. In future, these studies can be extended further to realize Fano resonance based optical switches, optical memory devices, digital and programmable devices and active sensors with tunable mode volumes. Further, the out-of plane asymmetry provides a unique advantage of accessing the optical response to the deep subwavelength changes in the structural asymmetry, which can provide a potential platform for developing a new area of nano-THz photonics[138].

In the last chapter (Chap. 6) of the thesis, a new form of quasiparticle interaction mechanisms were discussed and demonstrated in hybrid semiconductor-metamaterial systems that could lay a potential platform in probing the scattering mechanisms of the elementary excitation across the terahertz and far-infrared frequencies. The concept of blending the rich optical properties of solution processed semiconductors and the unnatural characteristics of the metamaterials can lead to an emergence of an entirely new hybrid heterostructure material system with enriched properties. In the presented work, the concept is probed in room temperature, where the strengths of the phonon modes are very weak that implies sensing and enhancing the strength

of resonant phonon modes of the solution processed perovskites using the strong localized plasmon resonances at terahertz frequencies. These studies open up a new possibility of observing strong resonant energy transfer and strong anti-crossing resonant characteristics in the cryogenic temperature that can lead to a formation of localized plasmon-phonon polaritons in the terahertz frequencies. The future works could involve elucidating the strong coupling regime of the solution processed perovskite-metamaterial hybrid system in lower temperatures and study the influence of structural phase transition of the perovskite material on the hybrid quasiparticle formation. Most of the recent studies have focused on the extracting the influence of photoexcited electrons in the semiconductors on the modulation characteristics of the metamaterials or plasmonic systems. However, the investigations concerning the effect of plasmons on the photoexited free carriers and their relaxation processes in the dynamic materials. This configuration of the spin coating the materials on the metamaterial structure can assist in investigating the influence of trapped plasmons on the properties of the photoexcited electrons, such as its photoconductivity and relaxation processes. Further, such a design of solution processed semiconductor-metamaterial hybrid device can benefit in realizing low-cost, stable and ultrafast switchable metamaterials in the terahertz part of EM spectrum. Next set of studies would involve integrating several other set of solution processed semiconducting materials with metamaterials in order to enhance the switching speed, sensitivity and the stability of the device for the future generation low cost and ultrafast active photonic devices.

# Appendix A

# Publications

## A.1 PhD Work Related Publications

1. Manukumara Manjappa, Sher-Yi Chiam, Longqing Cong, Andrew A Bettiol, Weili Zhang, Ranjan Singh. 'Tailoring the slow light behavior in terahertz metasurfaces'. *Appl. Phys. Lett.* **106**, 181101, (2015). https://doi.org/10.1063/1.4919531.

2. Manukumara Manjappa, Yogesh Kumar Srivastava, Ranjan Singh. 'Lattice-induced transparency in planar metamaterials'. *Phys. Rev. B* **94**, 161103(R) (2016). https://doi.org/10.1103/PhysRevB.94.161103.

3. Manukumara Manjappa, Yogesh Kumar Srivastava, Longqing Cong, Ibraheem Al-Naib, Ranjan Singh. 'Active photoswitching of sharp Fano resonances in THz metadevices'. *Adv. Mater.* **29**, 1603355 (2017). http://dx.doi.org/10.1002/adma.201603355.

4. Manukumara Manjappa, Shuvan Prashant Turaga, Yogesh Kumar Srivastava, Andrew Anthony Bettiol, Ranjan Singh. 'Magnetic annihilation of the dark mode in a strongly coupled brightdark terahertz metamaterial'. *Opt. Lett.* **42**, 2106-2109 (2017). https://doi.org/10.1364/OL.42.002106.

5. Manukumara Manjappa, Yogesh Kumar Srivastava, Ankur Solanki, Abhishek Kumar, Tze Chien Sum, Ranjan Singh. 'Hybrid lead halide perovskites for ultrasensitive photoactive switching in terahertz metamaterial devices'. *Adv. Mater.* **29**, 1605881 (2017). https://doi.org/10.1002/adma.201605881.

6. Manukumara Manjappa, Prakash Pitchappa, Nan Wang, Chengkuo Lee, Ranjan Singh. 'Active Control of Resonant Cloaking in a Terahertz MEMS Metamaterial'. *Adv. Opt. Mater.* **6**, 1800141 (2018). https://doi.org/10.1002/adom.201800141.

7. Manukumara Manjappa, Prakash Pitchappa, Navab Singh, Nan Wang, Nikolay. I . Zheludev, Chengkuo Lee, Ranjan Singh. 'Reconfigurable MEMS Fano

metasurfaces with multiple-input-output states for logic operations at terahertz frequencies'. *Nature Communications* **9**, 4056 (2018). https://doi.org/10.1038/s41467-018-06360-5

8. Wen Xiang Lim, Manukumara Manjappa, Prakash Pitchappa, Ranjan Singh. 'Shaping high-Q planar Fano resonant metamaterials towards futuristic technologies'. *Adv. Opt. Mater.* **6**, 1800502 (2018). https://doi.org/10.1002/adom.201800502. *Review article*

## A.2 Selected Collaborative Publications

1. Longqing Cong, Manukumara Manjappa, Ningning Xu, Ibraheem Al-Naib, Weili Zhang, Ranjan Singh. 'Fano resonances in terahertz metasurfaces: a figure of merit optimization'. *Adv. Opt. Mater.* **3**, 1537 (2015). http://dx.doi.org/10.1002/adom.201500207.

2. Yogesh Kumar Srivastava, Manukumara Manjappa, Longqing Cong, Wei Cao, Ibraheem Al-Naib, Weili Zhang, Ranjan Singh. 'UltrahighQ Fano Resonances in Terahertz Metasurfaces: Strong Influence of Metallic Conductivity at Extremely Low Asymmetry'. *Adv. Opt. Mater.* **4**, 457463 (2016). http://dx.doi.org/10.1002/adom.201500504.

3. Prakash Pitchappa, Manukumara Manjappa, Chong Pei Ho, Ranjan Singh, Navab Singh, Chengkuo Lee. 'Active control of electromagnetically induced transparency analog in terahertz MEMS metamaterial'. *Adv. Opt. Mater.* **4**, 541547 (2016). http://dx.doi.org/10.1002/adom.201500676.

4. Prakash Pitchappa, Manukumara Manjappa, Chong Pei Ho, Qian You, Ranjan Singh, Navab Singh, Chengkuo Lee. 'Active control of near-field coupling in conductively coupled microelectromechanical system metamaterial devices'. *Appl. Phys. Lett.* **108**, 111102 (2016). https://doi.org/10.1063/1.4943974.

5. Ningning Xu, Manukumara Manjappa, Ranjan Singh, Weili Zhang. 'Tailoring the Electromagnetically Induced Transparency and Absorbance in Coupled FanoLorentzian Metasurfaces: A Classical Analog of a FourLevel Tripod Quantum System'. *Adv. Opt. Mater.* **4** (8), 11791185 (2016). http://dx.doi.org/10.1002/adom.201600129.

6. Yogesh Kumar Srivastava, Manukumara Manjappa, Harish NS Krishnamoorthy, Ranjan Singh. 'Accessing the HighQ Dark Plasmonic Fano Resonances in Superconductor Metasurfaces'. *Adv. Opt. Mater.* **4** (11), 18751881 (2016). http://dx.doi.org/10.1002/adom.201600354.

7. Prakash Pitchappa, Manukumara Manjappa, Chong Pei Ho, Ranjan Singh, Navab Singh, Chengkuo Lee. 'Active control of electromagnetically induced transparency with dual dark mode excitation pathways using MEMS based

tri-atomic metamolecules'. *Appl. Phys. Lett.* **109**, 211103 (2016). https://doi.org/10.1063/1.4969061.

8. Kailing Shih, Prakash Pitchappa, Manukumara Manjappa, Chong Pei Ho, Ranjan Singh, Chengkuo Lee. 'Microfluidic metamaterial sensor: Selective trapping and remote sensing of microparticles'. *J of Appl. Phys.* **121**, 023102 (2017). https://doi.org/10.1063/1.4973492.

9. Manoj Gupta, Yogesh Kumar Srivastava, Manukumara Manjappa, Ranjan Singh. 'Sensing with toroidal metamaterial'. *Appl. Phys. Lett.* **110**, 121108 (2017). https://doi.org/10.1063/1.4978672.

10. Riad Yahiaoui, Manukumara Manjappa, Yogesh Kumar Srivastava, Ranjan Singh. 'Active control and switching of broadband electromagnetically induced transparency in symmetric metadevices'. *Appl. Phys. Lett.* **111**, 021101 (2017). https://doi.org/10.1063/1.4993428.

11. Prakash Pitchappa, Manukumara Manjappa, Harish NS Krishnamoorthy, Yuhua Chang, Chengkuo Lee, Ranjan Singh. 'Bidirectional reconfiguration and thermal tuning of microcantilever metamaterial device operating from 77K to 400K'. *Appl. Phys. Lett.* **111**, 261101 (2017). https://doi.org/10.1063/1.5006836.

12. Wen Xiang Lim, Manukumara Manjappa, Yogesh Kumar Srivastava, Longqing Cong, Abhishek Kumar, Kevin F MacDonald, Ranjan Singh. 'Ultrafast AllOptical Switching of GermaniumBased Flexible Metaphotonic Devices'. *Adv. Mater.* 1705331 (2018). https://doi.org/10.1002/adma.201705331.

# References


[1] Y. Lee, *Principles of Terahertz Science and Technology*, Lecture Notes in Physics (Springer US, 2009).

[2] B. Ferguson and X.-C. Zhang, Nature Materials **1**, 26 (2002).

[3] M. Tonouchi, Nature Photonics **1**, 97 (2007).

[4] K. Kawase, Y. Ogawa, Y. Watanabe, and H. Inoue, Opt. Express **11**, 2549 (2003).

[5] T. Kleine-Ostmann and T. Nagatsuma, Journal of Infrared, Millimeter, and Terahertz Waves **32**, 143 (2011).

[6] S. Koenig, D. Lopez-Diaz, J. Antes, F. Boes, R. Henneberger, A. Leuther, A. Tessmann, R. Schmogrow, D. Hillerkuss, R. Palmer, T. Zwick, C. Koos, W. Freude, O. Ambacher, J. Leuthold, and I. Kallfass, Nature Photonics **7**, 977 (2013).

[7] D. H. Auston, A. M. Glass, and P. LeFur, Applied Physics Letters **23**, 47 (1973).

[8] P. R. Smith, D. H. Auston, and M. C. Nuss, IEEE Journal of Quantum Electronics **24**, 255 (1988).

[9] C. Fattinger and D. Grischkowsky, Applied Physics Letters **53**, 1480 (1988).

[10] C. Fattinger and D. Grischkowsky, Applied Physics Letters **54**, 490 (1989).

[11] F. Zernike and P. R. Berman, Phys. Rev. Lett. **15**, 999 (1965).

[12] D. H. Auston and K. P. Cheung, J. Opt. Soc. Am. B **2**, 606 (1985).

[13] A. Rice, Y. Jin, X. F. Ma, X. Zhang, D. Bliss, J. Larkin, and M. Alexander, Applied Physics Letters **64**, 1324 (1994).

[14] A. Nahata, A. S. Weling, and T. F. Heinz, Applied Physics Letters **69**, 2321 (1996).

[15] C. Walther, M. Fischer, G. Scalari, R. Terazzi, N. Hoyler, and J. Faist, Applied Physics Letters **91**, 131122 (2007).

[16] G. Scalari, C. Walther, M. Fischer, R. Terazzi, H. Beere, D. Ritchie, and J. Faist, Laser & Photonics Reviews **3**, 45 (2009).

[17] W. Zouaghi, M. D. Thomson, K. Rabia, R. Hahn, V. Blank, and H. G. Roskos, European Journal of Physics **34**, S179 (2013).

[18] V. G. Veselago, Soviet Physics Uspekhi **10**, 509 (1968).

[19] W. Cai and V. Shalaev, *Optical Metamaterials* (Springer-Verlag New York, 2010).

[20] J. B. Pendry, A. J. Holden, D. J. Robbins, and W. J. Stewart, IEEE Transactions on Microwave Theory and Techniques **47**, 2075 (1999).

[21] D. R. Smith, W. J. Padilla, D. C. Vier, S. C. Nemat-Nasser, and S. Schultz, Phys. Rev. Lett. **84**, 4184 (2000).

[22] J. Pendry, Opt. Photon. News **15**, 32 (2004).

[23] J. B. Pendry, Phys. Rev. Lett. **85**, 3966 (2000).

[24] N. Fang, H. Lee, C. Sun, and X. Zhang, Science **308**, 534 (2005).

[25] D. R. Smith, J. B. Pendry, and M. C. K. Wiltshire, Science **305**, 788 (2004).

[26] T. J. Yen, W. J. Padilla, N. Fang, D. C. Vier, D. R. Smith, J. B. Pendry, D. N. Basov, and X. Zhang, Science **303**, 1494 (2004).

[27] E. Prodan, C. Radloff, N. J. Halas, and P. Nordlander, Science **302**, 419 (2003).

[28] N. Liu and H. Giessen, Angewandte Chemie International Edition **49**, 9838 (2010).

[29] B. Luk'yanchuk, N. I. Zheludev, S. A. Maier, N. J. Halas, P. Nordlander, H. Giessen, and C. T. Chong, Nature Materials **9**, 707 (2010).

[30] M. F. Limonov, M. V. Rybin, A. N. Poddubny, and Y. S. Kivshar, Nature Photonics **11**, 543 (2017).

[31] V. A. Fedotov, M. Rose, S. L. Prosvirnin, N. Papasimakis, and N. I. Zheludev, Phys. Rev. Lett. **99**, 147401 (2007).

[32] R. Singh, I. A. I. Al-Naib, M. Koch, and W. Zhang, Opt. Express **19**, 6312 (2011).

[33] S. Zhang, D. A. Genov, Y. Wang, M. Liu, and X. Zhang, Phys. Rev. Lett. **101**, 047401 (2008).

[34] N. Papasimakis, V. A. Fedotov, N. I. Zheludev, and S. L. Prosvirnin, Phys. Rev. Lett. **101**, 253903 (2008).

[35] N. Liu, L. Langguth, T. Weiss, J. Kstel, M. Fleischhauer, T. Pfau, and H. Giessen, Nature Materials **8**, 758 (2009).

[36] R. Singh, I. A. I. Al-Naib, Y. Yang, D. R. Chowdhury, W. Cao, C. Rockstuhl, T. Ozaki, R. Morandotti, and W. Zhang, Applied Physics Letters **99**, 201107 (2011).

[37] R. Singh, W. Cao, I. Al-Naib, L. Cong, W. Withayachumnankul, and W. Zhang, Applied Physics Letters **105**, 171101 (2014).

[38] Y. Yang, I. I. Kravchenko, D. P. Briggs, and J. Valentine, Nature Communications **5**, 5753 (2014).

[39] M. Gupta, Y. K. Srivastava, M. Manjappa, and R. Singh, Applied Physics Letters **110**, 121108 (2017).

[40] N. I. Zheludev, S. L. Prosvirnin, N. Papasimakis, and V. A. Fedotov, Nature Photonics **2**, 351 (2008).

[41] E. Plum, V. A. Fedotov, P. Kuo, D. P. Tsai, and N. I. Zheludev, Opt. Express **17**, 8548 (2009).

[42] K. L. Tsakmakidis, A. D. Boardman, and O. Hess, Nature **450**, 397 (2007).

[43] A. Reza, M. M. Dignam, and S. Hughes, Nature **455**, E10 (2008).

[44] C. Wu, A. B. Khanikaev, and G. Shvets, Phys. Rev. Lett. **106**, 107403 (2011).

[45] J. Gu, R. Singh, X. Liu, X. Zhang, Y. Ma, S. Zhang, S. A. Maier, Z. Tian, A. K. Azad, H.-T. Chen, A. J. Taylor, J. Han, and W. Zhang, Nature Communications **3**, 1151 (2012).

[46] Y. Yang, W. Wang, A. Boulesbaa, I. I. Kravchenko, D. P. Briggs, A. Puretzky, D. Geohegan, and J. Valentine, Nano Letters **15**, 7388 (2015).

[47] H. Liu, G. X. Li, K. F. Li, S. M. Chen, S. N. Zhu, C. T. Chan, and K. W. Cheah, Phys. Rev. B **84**, 235437 (2011).

[48] L. Luo, I. Chatzakis, J. Wang, F. B. P. Niesler, M. Wegener, T. Koschny, and C. M. Soukoulis, Nature Communications **5**, 3055 (2014).

[49] F. Alves, B. Kearney, D. Grbovic, and G. Karunasiri, Opt. Express **20**, 21025 (2012).

[50] H. Y. Hwang, K. Fan, A. Sternbach, X. Zhang, R. D. Averitt, and K. A. Nelson, in *Advanced Photonics 2013* (Optical Society of America, 2013).

[51] C. Belacel, Y. Todorov, S. Barbieri, D. Gacemi, I. Favero, and C. Sirtori, Nature Communications **8**, 1578 (2017).

[52] L. Cong, N. Xu, J. Gu, R. Singh, J. Han, and W. Zhang, Laser & Photonics Reviews **8**, 626 (2014).

[53] Y. Zhang, Y. Feng, B. Zhu, J. Zhao, and T. Jiang, Opt. Express **23**, 27230 (2015).

[54] W. J. Padilla, A. J. Taylor, C. Highstrete, M. Lee, and R. D. Averitt, Phys. Rev. Lett. **96**, 107401 (2006).

[55] H.-T. Chen, W. J. Padilla, J. M. O. Zide, A. C. Gossard, A. J. Taylor, and R. D. Averitt, Nature **444**, 597 (2006).

[56] H.-T. Chen, J. F. O'Hara, A. K. Azad, A. J. Taylor, R. D. Averitt, D. B. Shrekenhamer, and W. J. Padilla, Nature Photonics **2**, 295 (2008).

[57] J. Neu, B. Krolla, O. Paul, B. Reinhard, R. Beigang, and M. Rahm, Opt. Express **18**, 27748 (2010).

[58] H. Tao, A. C. Strikwerda, K. Fan, W. J. Padilla, X. Zhang, and R. D. Averitt, Phys. Rev. Lett. **103**, 147401 (2009).

[59] K. Bi, Y. Guo, X. Liu, Q. Zhao, J. Xiao, M. Lei, and J. Zhou, Scientific Reports **4**, 7001 (2014).

[60] W. Zhu, A. Liu, T. Bourouina, D. Tsai, J. Teng, X. Zhang, G. Lo, D. Kwong, and N. Zheludev, Nature Communications **3**, 1274 (2012).

[61] P. Pitchappa, M. Manjappa, C. P. Ho, R. Singh, N. Singh, and C. Lee, Advanced Optical Materials **4**, 541 (2016).

[62] J. Zhang, K. F. MacDonald, and N. I. Zheludev, Light: Science &Amp; Applications **2**, e96 (2013).

[63] Y.-S. Lin, P. Pitchappa, C. P. Ho, and C. Lee, Proc.SPIE **9302**, 9302 (2015).

[64] T. Weiland, M. Timm, and I. Munteanu, IEEE Microwave Magazine , 1527 (2008), DOI: 10.1109/MMM.2008.929772 .

[65] S. E. Harris, Physics Today **50**, 36 (1997).

[66] K.-J. Boller, A. Imamoğlu, and S. E. Harris, Phys. Rev. Lett. **66**, 2593 (1991).

[67] L. V. Hau, S. E. Harris, Z. Dutton, and C. H. Behroozi, Nature **397**, 594 (1999).

[68] C. L. G. Alzar, M. A. G. Martinez, and P. Nussenzveig, American Journal of Physics **70**, 37 (2002).

[69] S.-Y. Chiam, R. Singh, C. Rockstuhl, F. Lederer, W. Zhang, and A. A. Bettiol, Phys. Rev. B **80**, 153103 (2009).

[70] M. Manjappa, S.-Y. Chiam, L. Cong, A. A. Bettiol, W. Zhang, and R. Singh, Applied Physics Letters **106**, 181101 (2015).

[71] X. Yin, T. Feng, S. Yip, Z. Liang, A. Hui, J. C. Ho, and J. Li, Applied Physics Letters **103**, 021115 (2013).

[72] F. Y. Meng, Q. Wu, D. Erni, K. Wu, and J. C. Lee, IEEE Transactions on Microwave Theory and Techniques **60**, 3013 (2012).

[73] P. Tassin, L. Zhang, R. Zhao, A. Jain, T. Koschny, and C. M. Soukoulis, Phys. Rev. Lett. **109**, 187401 (2012).

[74] B. Gallinet and O. J. F. Martin, Phys. Rev. B **83**, 235427 (2011).

[75] D. R. Smith, J. B. Pendry, and M. C. K. Wiltshire, Science Review **30**, 788 (2004).

[76] W. J. Padilla, D. N. Basov, and D. R. Smith, Materials Today **9**, 28 (2006).

[77] U. Leonhardt, Science **312**, 1777 (2006).

[78] J. B. Pendry, D. Schurig, and D. R. Smith, Science **312**, 1780 (2006).

[79] J. Li and J. B. Pendry, Phys. Rev. Lett. **101**, 203901 (2008).

[80] P. Alitalo and S. Tretyakov, Materials Today **12**, 22 (2009).

[81] S. Linden, C. Enkrich, M. Wegener, J. Zhou, T. Koschny, and C. M. Soukoulis, Science **306**, 1351 (2004).

[82] T. Driscoll, H.-T. Kim, B.-G. Chae, B.-J. Kim, Y.-W. Lee, N. M. Jokerst, S. Palit, D. R. Smith, M. Di Ventra, and D. N. Basov, Science **325**, 1518 (2009).

[83] D. Roy Chowdhury, R. Singh, A. J. Taylor, H.-T. Chen, and A. K. Azad, Applied Physics Letters **102**, 011122 (2013), https://doi.org/10.1063/1.4774003 .

[84] W. X. Lim, M. Manjappa, Y. K. Srivastava, L. Cong, A. Kumar, K. F. MacDonald, and R. Singh, Advanced Materials **30**, 1705331 (2018), https://onlinelibrary.wiley.com/doi/pdf/10.1002/adma.201705331 .

[85] R. Singh, C. Rockstuhl, F. Lederer, and W. Zhang, Phys. Rev. B **79**, 085111 (2009).

[86] M. Gupta, V. Savinov, N. Xu, L. Cong, G. Dayal, S. Wang, W. Zhang, N. I. Zheludev, and R. Singh, Advanced Materials **28**, 8206 (2018), https://onlinelibrary.wiley.com/doi/pdf/10.1002/adma.201601611 .

[87] M. Kerker, J. Opt. Soc. Am. **65**, 376 (1975).

[88] A. Alù and N. Engheta, Phys. Rev. E **72**, 016623 (2005).

[89] A. Alù and N. Engheta, Opt. Express **15**, 3318 (2007).

[90] M. G. Silveirinha, A. Alù, and N. Engheta, Phys. Rev. B **78**, 075107 (2008).

[91] P. Alitalo, F. Bongard, J.-F. Zrcher, J. Mosig, and S. Tretyakov, Applied Physics Letters **94**, 014103 (2009).

[92] R. Singh, C. Rockstuhl, and W. Zhang, Applied Physics Letters **97**, 241108 (2010).

[93] L. Cong, M. Manjappa, N. Xu, I. Al-Naib, W. Zhang, and R. Singh, Advanced Optical Materials **3**, 1537 (2015).

[94] N. I. Zheludev and Y. S. Kivshar, Nature Materials **11**, 917 (2012).

[95] K. Fan and W. J. Padilla, Materials Today **18**, 39 (2015).

[96] W. M. Zhu, A. Q. Liu, X. M. Zhang, D. P. Tsai, T. Bourouina, J. H. Teng, X. H. Zhang, H. C. Guo, H. Tanoto, T. Mei, G. Q. Lo, and D. L. Kwong, Advanced Materials **23**, 1792 (2011).

[97] J. Y. Ou, E. Plum, L. Jiang, and N. I. Zheludev, Nano Letters **11**, 2142 (2011).

[98] D. R. Smith, D. C. Vier, T. Koschny, and C. M. Soukoulis, Phys. Rev. E **71**, 036617 (2005).

[99] L. Rayleigh, Proceedings of the Royal Society of London A: Mathematical, Physical and Engineering Sciences **79**, 399 (1907).

[100] V. G. Kravets, F. Schedin, and A. N. Grigorenko, Phys. Rev. Lett. **101**, 087403 (2008).

[101] R. W. Wood, Proceedings of the Physical Society of London **18**, 269 (1902).

[102] S. Linden, J. Kuhl, and H. Giessen, Phys. Rev. Lett. **86**, 4688 (2001).

[103] E. M. Hicks, S. Zou, G. C. Schatz, K. G. Spears, R. P. Van Duyne, L. Gunnarsson, T. Rindzevicius, B. Kasemo, and M. Kall, Nano Letters **5**, 1065 (2005).

[104] B. Auguié and W. L. Barnes, Phys. Rev. Lett. **101**, 143902 (2008).

[105] A. Bitzer, J. Wallauer, H. Helm, H. Merbold, T. Feurer, and M. Walther, Opt. Express **17**, 22108 (2009).

[106] N. Xu, R. Singh, and W. Zhang, Applied Physics Letters **109**, 021108 (2016).

[107] J. Keller, C. Maissen, J. Haase, G. L. Paravicini-Bagliani, F. Valmorra, J. Palomo, J. Mangeney, J. Tignon, S. S. Dhillon, G. Scalari, and J. Faist, Advanced Optical Materials **5**, 1600884 (2017).

[108] M. Manjappa, Y. K. Srivastava, and R. Singh, Phys. Rev. B **94**, 161103 (2016).

[109] Y. K. Srivastava, M. Manjappa, L. Cong, W. Cao, I. Al-Naib, W. Zhang, and R. Singh, Advanced Optical Materials **4**, 457 (2016).

[110] M. C. Schaafsma, A. Bhattacharya, and J. G. Rivas, *ACS Photonics*, ACS Photonics **3**, 1596 (2016).

[111] H. Xu, Y. Lu, Y. Lee, and B. S. Ham, Opt. Express **18**, 17736 (2010).

[112] I. Al-Naib, E. Hebestreit, C. Rockstuhl, F. Lederer, D. Christodoulides, T. Ozaki, and R. Morandotti, Phys. Rev. Lett. **112**, 183903 (2014).

[113] N. Xu, M. Manjappa, R. Singh, and W. Zhang, Advanced Optical Materials **4**, 1179 (2016).

[114] M. Manjappa, Y. K. Srivastava, L. Cong, I. Al-Naib, and R. Singh, Advanced Materials **29**, 1603355 (2017).

[115] T. Kaelberer, V. A. Fedotov, N. Papasimakis, D. P. Tsai, and N. I. Zheludev, Science **330**, 1510 (2010).

[116] U. Fano, Phys. Rev. **124**, 1866 (1961).

[117] A. E. Miroshnichenko, S. Flach, and Y. S. Kivshar, Rev. Mod. Phys. **82**, 2257 (2010).

[118] B. Zeng, Y. Gao, and F. J. Bartoli, Applied Physics Letters **105**, 161106 (2014).

[119] M. Manjappa, P. Pitchappa, N. Singh, N. Wang, N. I. Zheludev, C. Lee, and R. Singh, Nature Communications **9**, 4056 (2018).

[120] N. J. Croft and M. S. Olivier, in *Southern African Telecommunication Networks and Applications Conference 2005 (SATNAC 2005) Proceedings*, Vol. 1, edited by D. Browne (Champagne Castle, South Africa, 2005) pp. 71–76.

[121] C. Della Giovampaola and N. Engheta, Nature Materials **13**, 1115 (2014).

[122] T. J. Cui, M. Q. Qi, X. Wan, J. Zhao, and Q. Cheng, Light: Science &Amp; Applications **3**, e218 (2014).

[123] N. I. Zheludev, Science **348**, 973 (2015).

[124] S. H. Mousavi, I. Kholmanov, K. B. Alici, D. Purtseladze, N. Arju, K. Tatar, D. Y. Fozdar, J. W. Suk, Y. Hao, A. B. Khanikaev, R. S. Ruoff, and G. Shvets, Nano Letters **13**, 1111 (2013).

[125] S. A. Veldhuis, P. P. Boix, N. Yantara, M. Li, T. C. Sum, N. Mathews, and S. G. Mhaisalkar, Advanced Materials **28**, 6804 (2016).

[126] B. R. Sutherland and E. H. Sargent, Nature Photonics **10**, 295 (2016).

[127] C.-X. Sheng, Y. Zhai, E. Olejnik, C. Zhang, D. Sun, and Z. Vardeny, Opt. Mater. Express **5**, 530 (2015).

[128] B. Gholipour, G. Adamo, D. Cortecchia, H. N. S. Krishnamoorthy, M. D. Birowosuto, N. I. Zheludev, and C. Soci, Advanced Materials **29**, 1604268 (2017), 1604268.

[129] W. Zhao, Q. Wu, Q. Hao, J. Wang, M. Li, Y. Zhang, K. Bi, Y. Chen, and Z. Ni, Applied Physics Letters **108**, 131903 (2016).

[130] E. H. Hwang, R. Sensarma, and S. Das Sarma, Phys. Rev. B **82**, 195406 (2010).

[131] Y. Cui, A. Lauchner, A. Manjavacas, F. J. Garca de Abajo, N. J. Halas, and P. Nordlander, Nano Letters **16**, 6390 (2016).

[132] D. Shelton, I. Brener, J. C. Ginn, M. B. Sinclair, D. W. Peters, K. R. Coffey, and G. D. Boreman, Nano Letters **11**, 2104 (2011).

[133] M. Ramezani, A. Halpin, A. I. Fernández-Domínguez, J. Feist, S. R.-K. Rodriguez, F. J. Garcia-Vidal, and J. G. Rivas, Optica **4**, 31 (2017).

[134] M. Manukumara, S. Y. Kumar, S. Ankur, K. Abhishek, S. T. Chien, and S. Ranjan, Advanced Materials **29**, 1605881.

[135] F. Brivio, J. M. Frost, J. M. Skelton, A. J. Jackson, O. J. Weber, M. T. Weller, A. R. Goni, A. M. A. Leguy, P. R. F. Barnes, and A. Walsh, Phys. Rev. B **92**, 144308 (2015).

[136] C. La-o vorakiat, H. Xia, J. Kadro, T. Salim, D. Zhao, T. Ahmed, Y. M. Lam, J.-X. Zhu, R. A. Marcus, M.-E. Michel-Beyerle, and E. E. M. Chia, The Journal of Physical Chemistry Letters **7**, 1 (2016).

[137] M. Sendner, P. K. Nayak, D. A. Egger, S. Beck, C. Muller, B. Epding, W. Kowalsky, L. Kronik, H. J. Snaith, A. Pucci, and R. Lovrincic, Mater. Horiz. **3**, 613 (2016).

[138] M. A. Seo, H. R. Park, S. M. Koo, D. J. Park, J. H. Kang, O. K. Suwal, S. S. Choi, P. C. M. Planken, G. S. Park, N. K. Park, Q. H. Park, and D. S. Kim, Nature Photonics **3**, 152 (2009).